9-12-2018 3:00 PM

Numerical Simulation of Three-Phase Flows in the Inverse Fluidized bed

Yunfeng Liu, *The University of Western Ontario*

Supervisor: Zhang, Chao, *The University of Western Ontario*
Co-Supervisor: Zhu, JingXu, *The University of Western Ontario*
A thesis submitted in partial fulfillment of the requirements for the Master of Engineering Science degree in Mechanical and Materials Engineering

Abstract

The inverse three-phase fluidized bed has excellent potentials to be used in chemical, biochemical, petrochemical and food industries because of its high contact efficiency among each phase which leads to a good mass and heat transfer. The understanding of the hydrodynamics and flow structures in inverse three-phase fluidized beds is important for the design and scale up purposes.

A CFD model based on the Eulerian-Eulerian (E-E) approach coupled with the kinetic theory of the granular flow is successfully developed to simulate an inverse three-phase fluidization system. The proposed CFD model for the inverse three-phase fluidization system is validated by comparing the numerical results with the experimental data. Investigations on the hydrodynamics and flow structures in the inverse three-phase fluidized bed under a batch liquid mode are conducted by numerical studies. The development of the fluidization processes and the general gas-liquid-solids flow structures under different operating conditions are further studied by the proposed three-phase E-E CFD model. Parametric studies including different inlet superficial gas velocities, particle densities, and solids loadings are investigated numerically. The numerical results show a general non-uniform radial flow structure in the inverse three-phase fluidized bed. It is also found that the particle distribution profiles in the axial direction relate to the solids loading, particle density and inlet superficial gas velocity. The existences of the liquid and solids recirculation inside the inverse three-phase fluidized bed are also noticed under the batch liquid mode.

Moreover, the proposed CFD model for the inverse three-phase fluidized bed is further modified by adjusting the bubble size. The modified CFD model takes the bubble size effects into account and performs better on estimating the average gas holdup. In addition, a correlation between the bubble size and the superficial gas velocity, gas holdup and physical properties of the liquid and solid phases is proposed based on the numerical results. The predicted bubble size and the gas holdup in the inverse three-phase fluidized beds under a batch mode using the proposed correlation agree well with the experimental data. Therefore, the proposed three-phase E-E CFD model incorporated with the bubble

size adjustment can be used to predict the performance of the inverse three-phase fluidization system more accurately.

Keywords: computational fluid dynamic (CFD), inverse fluidized bed, three-phase flow, bubble size

Co-Authorship Statement

Chapter 3 and Chapter 4 of this thesis will be submitted for publications.

All papers are drafted by Yunfeng Liu and modified under the supervision of Prof. Chao Zhang and Prof. Jesse Zhu and in consultation with Miss Zeneng Sun in Prof. Chao Zhang's research group

Acknowledgement

I would like to take this opportunity to express the gratitude and appreciation to those who have always been helping and supporting me throughout my master's study.

First, I would like to express my sincerest thank to my Supervisor Prof. Zhu and Prof. Zhang, for believing my potential, providing me advice, support and encouragement through my entire research work. I attribute the thesis to their guidance and efforts, which ensured the work to be successfully completed.

Then I would like to thank all members of our Computational Fluid Dynamics Research Laboratory, especially Zeneng Sun, Huirui Han, Hao Luo for their help and friendship in both academic and daily life.

Finally, I would like to thank my parents for their encouragement and support during the entire process.

Table of Contents

Abstract i

Co-Authorship Statement iii

Acknowledgement iv

Table of Contents v

Nomenclature ix

List of Tables xi

List of Figures xii

Chapter 1 1

1 Introduction 1

1.1 Background 1

1.2 Literature review 4

1.2.1 Experimental studies of the hydrodynamic characteristics of the inverse three-phase fluidized beds 4

1.2.1.1 Modes of operation and flow regimes 5

1.2.1.2 Particle movements 7

1.2.1.3 Phase holdups 8

1.2.1.4 Remarks 9

1.2.2 CFD modelling of multiphase flows in fluidized beds 9

1.3 Objectives 17

1.4 Thesis structure 18

Reference 19

Chapter 2 24

2 A CFD Model for the Simulation of the Inverse Gas-Liquid-Solid Fluidized Bed .. 24

2.1 Introduction 24

2.2 Experimental setup of the inverse three-phase fluidized bed 27

2.3 Numerical models 30

2.3.1 Governing equations 30

2.3.2 Interphase forces 31

2.3.3 Turbulence model 32

2.4 Numerical methodology 37

2.5 Results and discussion 38

2.5.1 Grid independence test and CFD model validation 38

2.5.2 Flow development and flow structure in an inverse three-phase fluidized bed 40

2.5.2.1 Initial fluidization stage 41

2.5.2.2 Developing stage 46

2.5.2.3 Fully developed stage 49

2.5.3 Effects of the solids loading 54

2.5.4 General flow structure 60

2.5.5 Recirculation 69

2.6 Conclusions 73

Reference 75

Chapter 3 78

3 Modification of the CFD Model Based on the Bubble Size Adjustment for the Inverse Three-phase Fluidized Bed 78

3.1 Introduction 78

3.2 Experimental setup of the inverse three-phase fluidized bed 82

3.3 Numerical models 85

3.3.1 Governing equations 85

3.3.2 Interphase forces 86

3.3.3 Turbulence model 87

3.4 Numerical methodology 91

3.5 Grid Independence test 93

3.6 Results and discussion 94

3.6.1 Bubble size adjustment under different U_g 94

3.6.2 Mean bubble size correlation 101

3.7 Conclusions 102

Reference 103

Chapter 4 106

4 Conclusions and Recommendations 106

4.1 Conclusions 106

4.2 Recommendations 107

Curriculum Vitae 109

Nomenclature

Notation

$C_{1\varepsilon}$	Turbulence constants, dimensionless
$C_{2\varepsilon}$	Turbulence constants, dimensionless
$C_{3\varepsilon}$	Turbulence constants, dimensionless
C_D	Drag coefficient, dimensionless
d_p	Mean particles diameter, m
d_b	Mean bubble size, m
D	Column diameter, m
e	Restitution coefficient for particle-particle collision, dimensionless
g	Acceleration due to gravity, m/s^2
g_0	Radial distribution function, dimensionless
G_b	Generation of turbulence kinetic energy due to buoyancy, m^2/s^2
G_k	Generation of turbulence kinetic energy due to the mean velocity gradients, m^2/s^2
H	Column height from bottom to top, m
k	Turbulent kinetic energy, m^2/s^2
K	Interphase momentum exchange coefficient, kg/m^3s
p	Pressure, Pa
Re	Reynolds number, dimensionless
t	Time, s

U_g Superficial gas velocity, m/s

v Velocity, m/s

x Radial position from left wall to right wall, m

Greek letters

α Local volume fraction, dimensionless

ε Turbulent energy dissipation rate, m^2/s^2

ε_g Gas holdup, dimensionless

γ Collision dissipation rate of energy, kg/ms^3

k_{Θ_s} Granular conductivity, kg/m^3s

Θ Granular temperature, m^2/s^2

λ Bulk viscosity, kg m/s

μ Dynamic viscosity, kg/m-s

ρ Density kg/m^3

τ Stress sensor, Pa

Subscripts

l Liquid phase

g Gas phase

s Solid phase

List of Tables

Table2.1 Operating conditions and physical properties of the liquid, gas and solid phases 29

Table 2.2 Parameters of the RNG k-ε models 35

Table 2.3 Mesh information for the grid independent test..... 39

Table 2.4 Average gas holdups for different meshes..... 39

Table 3.1 Operating conditions and physical properties of each phase..... 84

Table 3.2 Parameters of the dispersed RNG k-ε models 89

Table 3.3 Constitutive equations of the solid phases..... 90

Table 3.4 Mesh information for the grid independent test..... 94

Table 3.5 Average gas holdups from different meshes..... 94

Table 3.6 Bubble sizes under the different inlet superficial gas velocities..... 96

List of Figures

Figure 1.1 Schematic diagram of the gas-liquid-solid three-phase fluidization (Muroyama & Fan, 1985) 4

Figure 1.2 Flow regimes in the three-phase inverse fluidized bed. (Fan et al., 1982)..... 6

Figure 1.3 Flow regime map of the three-phase bubble column under the batch mode (Sun, 2017) 7

Figure 2.1 Configuration of the experimental setup of the inverse three-phase fluidized bed (Sun, 2017)..... 28

Figure 2.2 Computational domain of the inverse three-phase fluidized bed 38

Figure 2.3 Comparison of the axial profiles of the solids volume fraction between the numerical results and experimental data at U_g=15 mm/s, 15% loading and ρ_s=930 kg/m^3 40

Figure 2.4 Contours of the solids volume fraction at different time of the initial fluidization stage for Ug=15mm/s, 15% solids loading and ρ_s= 930 kg/m^3 41

Figure 2.5 Axial profiles of the solids volume fraction at different time at the initial fluidization stage..... 42

Figure 2.6 Radial profiles of the solids volume fraction at different axial locations at the initial fluidization stage (t=30s). 43

Figure 2.7 Radial profiles of the gas volume fraction at different axial locations at the initial fluidization stage (t=30s) 44

Figure 2.8 Radial profiles of the solids axial velocity at different axial locations at the initial fluidization stage (t=30s) 45

Figure 2.9 Radial profiles of the liquid and gas axial velocities at H=0.5 m (t=30s)..... 45

Figure 2.10 Contours of the solids volume fraction at different time at the developing stage 46

Figure 2.11 Axial profiles of the solids volume fraction at different time at the developing stage (t=150s) 47

Figure 2.12 Radial profiles of the gas volume fraction at different axial locations at the developing stage (t=150s) 48

Figure 2.13 Radial profiles of the solids volume fraction at different axial locations at the developing stage (t=150s) 48

Figure 2.14 Radial profiles of the solids axial velocity component at different axial locations at the developing stage (t=150s) 49

Figure 2.15 Contours of the solid phase volume fraction at the fully developed stage with time 50

Figure 2.16 Time-averaged axial profile of the solids volume fraction at the fully developed stage 51

Figure 2.17 Time-averaged axial profile of the gas volume fraction at the fully developed stage 51

Figure 2.18 Time-averaged radial profiles of the solids axial velocity at different axial locations 53

Figure 2.19 Time-averaged radial profiles of the solids volume fraction at different axial locations 53

Figure 2.20 Time-averaged radial profiles of the solid and liquid axial velocities at H=1m 54

Figure 2.21 Effects of the solids loading on the flow development time 55

Figure 2.22 Axial profiles of the solids volume fraction under different solids loadings at U_g=15mm/s and ρ_s=930kg/m^3 56

Figure 2.23 Radial profiles of the solids axial velocity under different solids loadings at U_g=15mm/s and ρ_s=930kg/m^3 57

Figure 2.24 Radial profiles of the solids volume fraction under different solids loadings at Ug=15mm/s and ρ_s=930kg/m^3 58

Figure 2.25 Radial profiles of the gas hold up at U_g=15mm/s and ρ_s=930kg/m^3 59

Figure 2.26 Time required to reach to the developing and fully developed stages under differet inlet superficial gas velocities 60

Figure 2.27 Contours of the solids volume fraction under different inlet superficial velocities at 15% solids loading and ρ_s=930 kg/m^3 63

Figure 2.28 Radial profiles of the solids volume fraction under different inlet superficial gas velocities 64

Figure 2.29 Average gas holdup under different particle densities at U_g=15mm/s, and 15% solids loading 65

Figure 2.30 Contours of the solids volume fraction with different particle densities at 15% solids loading and U_g=15mm/s 66

Figure 2.31 Radial profiles of solids holdup with different particle densities at 15% solids loading and U_g=15mm/s 68

Figure 2.32 Radial profiles of the solids axial velocity under different inlet superficial gas velocities 70

Figure 2.33 Instantaneous volume fraction contour (left) and particle velocity vector contour (right) 73

Figure 3.1 Configuration of the experimental setup of the inverse three-phase fluidized bed (Sun, 2017)..... 83

Figure 3.2 Computational domain of the inverse three-phase fluidized bed under the batch liquid mode 93

Figure 3.3 Comparison of the average gas holdup between the numerical results and experimental data under the different inlet superfical gas velocities at 15% solids loading and $\rho_{s=}$930 kg/m^3..... 96

Figure 3.4 Comparison of the axial gas holdups from the origin CFD model and modified CFD model with the experiment data at $\rho_{s=}$930 kg/m^3 and 15% solids loading..... 98

Figure 3.5 Time-averaged radial gas holdups under different superficial gas velocities from the modified CFD model 99

Figure 3.6 Comparison of the radial profiles of the gas holdup between the origin CFD model and the modified CFD model at 15% solids loading and ρ_s=930 kg/m^3 100

Chapter 1

1 Introduction

1.1 Background

Fluidization is a process that makes the solid particles behave like fluid by introducing liquid or gas flow. The concept of the fluidized bed was first proposed for the gasification of coal in the 1920s, and the fluidization was used for fluid catalytic processes (FCC) in 1940s (Werther, Hartge, & Heinrich, 2014). Today, fluidized beds are widely used in chemical, biochemical, petrochemical and food industries because of the good heat and mass transfer.

Usually, fluidized beds can be categorized by the fluidizing agent, so that there are liquid-solid two-phase fluidization, gas-solid two-phase fluidization and gas-liquid-solid (GLS) three-phase fluidization. Gas-solid fluidized beds were the first to be applied in industries, then the application extended to the liquid-solid and gas-liquid-solid fluidized beds.

With the development of fluidization technology, fluidized beds can also be characterized by the flow directions after the concept of the inverse fluidized bed was proposed. Fluidized beds can be further divided into upward fluidized beds and inverse fluidized beds.

For the traditional upward two-phase fluidization process, the liquid or gas is injected into the reactor from the bottom and flows through the space between particles. Under a low fluid velocity, the drag force acting on the particles cannot overcome the gravity of particles, causing them to remain packed. The fluidization begins as the fluid velocity reaches to the minimum fluidization velocity where the drag force acting on the particles can balance the gravity of the particles. Minimum fluidization velocity U_{mf} is an important parameter for designing the fluidized bed (Zhu, Na, & Lu, 2007). By further increasing the fluid velocity, the drag force acting on particles will increase and particles will entrain out of the fluidized bed reactor, and the fluidized bed becomes a circulating fluidized bed if the entrained particles are recycled.

For gas-solid upward fluidization, the fluidized bed usually goes through the bubbling regime, turbulent regime, fast fluidization regime, to the pneumatic transport regime with the increase in the superficial gas velocity (Grace, 1986). For the gas-liquid-solid fluidization, the gas phase is usually introduced into the reactor as bubbles. The flow regime can be divided into dispersed bubble flow, discrete bubble flow, coalesced bubble flow, slug flow, churn flow, bridging flow and annular flow at different gas and liquid velocities (Zhang, Grace, Epstein, & Lim, 1997).

As mentioned before, the three-phase GLS fluidized bed has been studied since 1970s with the development of fluidization technology (Ostergaard, 1971). Due to the close contact among solid, liquid and gas phases in GLS three-phase fluidized beds (TPFBs), it is used in chemical and biochemical processing (Muroyama & Fan, 1985). Three-phase fluidization can be divided into upward flow three-phase fluidization and inverse three-phase fluidization depending on the flow direction of the gas and liquid phases. The different modes of three-phase fluidization is shown in Figure 1.1. Modes 1a and 1b are co-current flows where the air and liquid are injected from the bottom of the reactor and particles are moving upward. Modes 2a and 2b are countercurrent flows where the gas is introduced to the reactor from the bottom and the liquid is injected from the top of the reactor. The density of the particles used for modes 2a and 2b are usually less than the density of the liquid medium, allowing particles to overcome the buoyancy force and expand downward during the fluidization process. Besides modes 2a and 2b, the inverse fluidization can be also operated under the batch liquid mode (Comte, Bastoul, Hebrard, Roustan, & Lazarova, 1997; Sun, 2017), in which the liquid initially fills the reactor and the particles are floated at the top surface of the liquid before the operation starts. In the inverse fluidized bed under the batch mode operating condition, the fluidization state of the particles can be achieved with the zero liquid velocity when the superficial gas velocity is high enough resulting in the drag force and gravity acting on particles balanced with the buoyancy force. Compared to the upward flow three-phase fluidization, the inverse three-phase fluidization can reduce energy cost and minimum solids attrition as the solid phase can be fluidized under low liquid and gas velocities, and the particle entrainment problem can be eliminated without using any external equipment (Ibrahim, Briens, Margaritis, & Bergongnou, 1996). The inverse three-phase fluidized bed has been started to be used in

wastewater treatment industries. Compared with the traditional methods of the wastewater treatment such as activated sludge process which requires longer retention time and large space, the retention time can be reduced in fluidized bed reactor due to high biomass concentration, and another problem of excessive growth of biomass on particles can be fixed by using light particles in inverse fluidized beds as well (Sokół & Korpal, 2006).

Understanding the hydrodynamics of inverse three-phase fluidized beds is important when designing the reactors for industrial applications. Fan, Muroyama and Chern (1982) first defined the flow regime for the inverse three-phase fluidized bed, which are the fixed bed with dispersed bubble regime, bubbling fluidized bed regime, transition regime and slugging flow regime based on the liquid and gas velocities. Other flow characteristics in the inverse three-phase fluidized bed including the phase holdup, minimum fluidization velocity, pressure drop, bubble behavior, bed expansion has been studied by many researchers (Briens, Ibrahim, Margaritis, & Bergougnou, 1999; Renganathan & Krishnaiah, 2008; Son, Kang, Kim, Kang, & Kim, 2007). However, few researchers have reported the flow structure in the radial direction of the inverse three-phase fluidized bed.

	1a	1b	2a	2b
Diagram of GLS fluidized bed	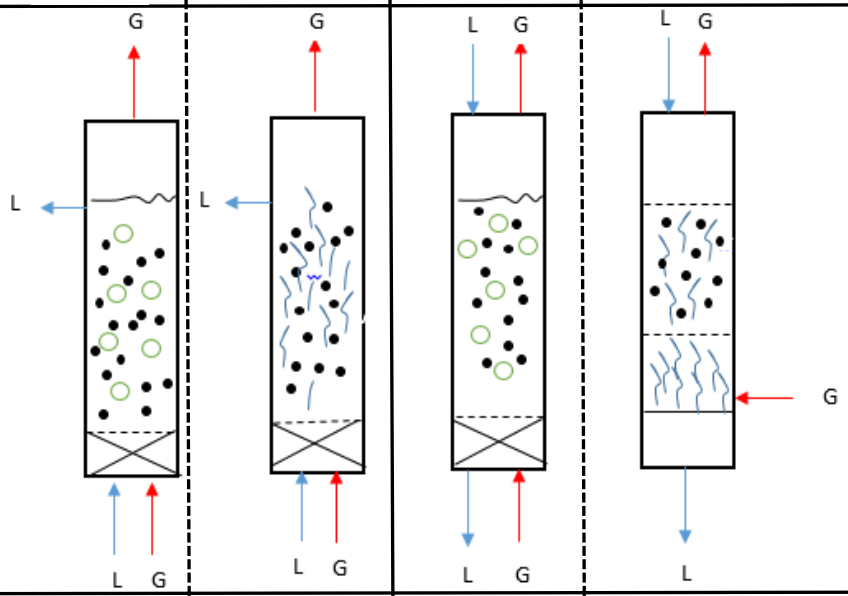			
Continuous phase	**Liquid**	**Gas**	**Liquid**	**Gas**
Flow direction	**Cocurrent Up-flow**		**Countercurrent flow**	

Figure 1.1 Schematic diagram of the gas-liquid-solid three-phase fluidization (Muroyama & Fan, 1985)

Although a few experimental studies on the hydrodynamics in GLS three-phase flows have been conducted, it is hard to fully understand the underlying phenomena of the GLS three-phase fluidization due to the complex interactions between each phase. There is even less studies focused on predicting the flow characteristics of the inverse three-phase fluidized bed due to the restrictions of the experiments. Therefore, with the rapid development of computer technology, CFD has become a powerful tool to simulate the multiphase flow and provide more details on the three-phase fluidization process. In addition, CFD is considered to be more time and economic efficient to simulate complex flows compared with the experimental method. However, few CFD models has been developed to predict the hydrodynamics and flow structure in inverse three-phase fluidized beds (TPFBs).

1.2 Literature review

The literature review will focus on two parts, which are the experiment studies on the hydrodynamics of the GLS three-phase inverse fluidized bed and the CFD simulations of the GLS three-phase fluidized bed.

1.2.1 Experimental studies of the hydrodynamic characteristics of the inverse three-phase fluidized beds

Minimum fluidization velocity is an important parameter to consider when designing an inverse three-phase fluidized bed. Minimum fluidization velocity is defined as the velocity when the pressure gradient across the bed is minimum in the inverse three-phase fluidized bed (Ibrahim et al., 1996). Ibrahim et al.(1996) found that the minimum liquid fluidization velocity will decrease when increasing the gas velocity. Many researchers also reported the same trend in which the minimum liquid fluidization velocity decreases with the increase in gas flowrate (Bandaru, Murthy, & Krishnaiah, 2007; Cho, Park, Kim, Kang, & Kim, 2002; D. H. Lee, Epstein, & Grace, 2000; Renganathan & Krishnaiah, 2008). Renganathan and Krishnaiah (2008) also found the same results and developed the correlation for the minimum gas fluidization velocity in inverse three-phase fluidized beds under the batch liquid (U_l=0) operating condition.

1.2.1.1 Modes of operation and flow regimes

Inverse three-phase fluidized beds can operate under the batch liquid mode or continuous mode. Under the batch liquid mode, the liquid velocity is zero, and the fluidization state of particles can be achieved by injecting gas only. The main method to determine the flow regime for inverse three-phase fluidized beds is by visual observation of the flow phenomena (particle movement or bubble behavior) in the experiment.

Fan et al. (1982) conducted the first experimental study to investigate the hydrodynamics in the three-phase inverse fluidized bed. Both the gas and liquid phase can be considered as the continuous phase in an inverse three-phase fluidized bed. Fan et al. (1982) defined four flow regimes shown in Figure 1.2 based on the gas and liquid velocities in an inverse three-phase fluidized bed, which are: (a) the fixed bed with the dispersed bubble regime, (b) the bubbling fluidized bed regime, (c) the transition regime and (d) the slugging fluidized bed regime. In the fixed bed with dispersed bubble regime, the gas and liquid velocities are low, and the drag force and gravity acting on the particle cannot overcome the buoyancy force. In this regime, the particles remain packed. With the increase in gas and liquid velocities, the bubbling fluidized bed regime can be reached. The gravity and drag force exerted on particles can balance the buoyancy force, so, particles start to fluidize from the bottom of packed bed, ultimately distributing uniformly along the reactor. The bubble size is uniform within the bubbling fluidized bed regime. At the transition regime, bubbles starts to coalescence and their sizes will change. At the slugging fluidized bed regime, particles will move upward with slug bubbles, and then settle down quickly, and the interaction between particles and bubbles will affect their flows.

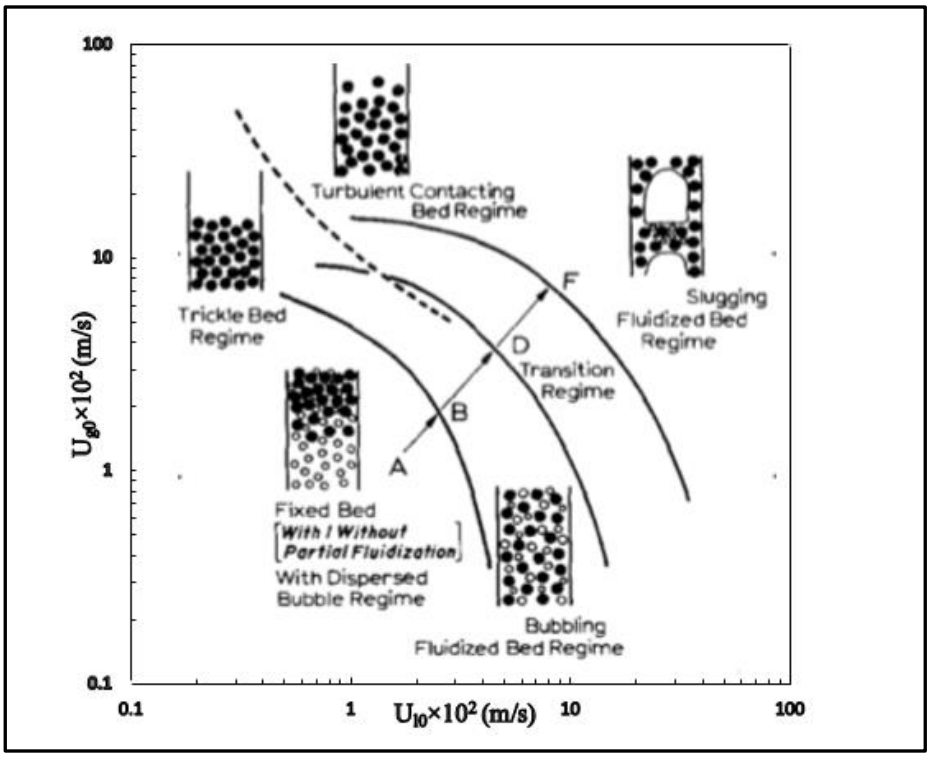

Figure 1.2 Flow regimes in the three-phase inverse fluidized bed. (Fan et al., 1982)

Only a few researchers studied the batch mode of the inverse three-phase fluidized bed compared to the continuous mode. Comte et al. (1997) conducted experiments in an inverse TPFB under the batch mode operating condition. The particles used in the experiment have a mean density of 934 kg/m^3, and gas bubbles are introduced into the fluidized bed by using a perforate plate and membrane distributor. Three significant transition velocities have been defined based on different distributions of the solid phase to distinguish the flow regimes and study the flow behavior: (1) the minimum gas fluidization velocity U_{g1} that can break the fixed bed; (2) velocity U_{g2} is the velocity at which some particle can reach the bottom of the reactor; (3) velocity U_{g3}, at this velocity, the particle distribution is uniform along the reactor. It was found that U_{g2} and U_{g3} will decrease when increasing the solids loading or particle density. A mathematical model to predict velocity U_{g3} was developed based on the assumption that the particle movement is mainly due to the density difference between particles and mixture of gas and liquid. Sun (2017) also proposed similar specific transition velocities, which are the initial fluidization velocity, expansion velocity, and complete fluidization velocity to study the flow behavior of solid phase

shown in Figure 1.3. In addition, when the superficial gas velocity is above $U_{g4,}$ a free board region can be observed. It was also confirmed that U_{g1}, U_{g2} and U_{g3} will decrease with the increase in the particle density. Han et al. (2003) used particles with a density of 934 kg/m^3 but the gas distributor used in their experiment is different from the distributor used in the experimental study by Comte et al. (1997), so a different U_{g3} value was derived. Thus, the gas distributor is one of the factors that can influence the U_{g3} (Han et al., 2003). Sun (2017) further confirmed this fact by using particles with a density of 930 kg/m^3 and the porous quartz gas distributor, which can generate small bubbles, obtained the smallest U_{g3} value among the three studies.

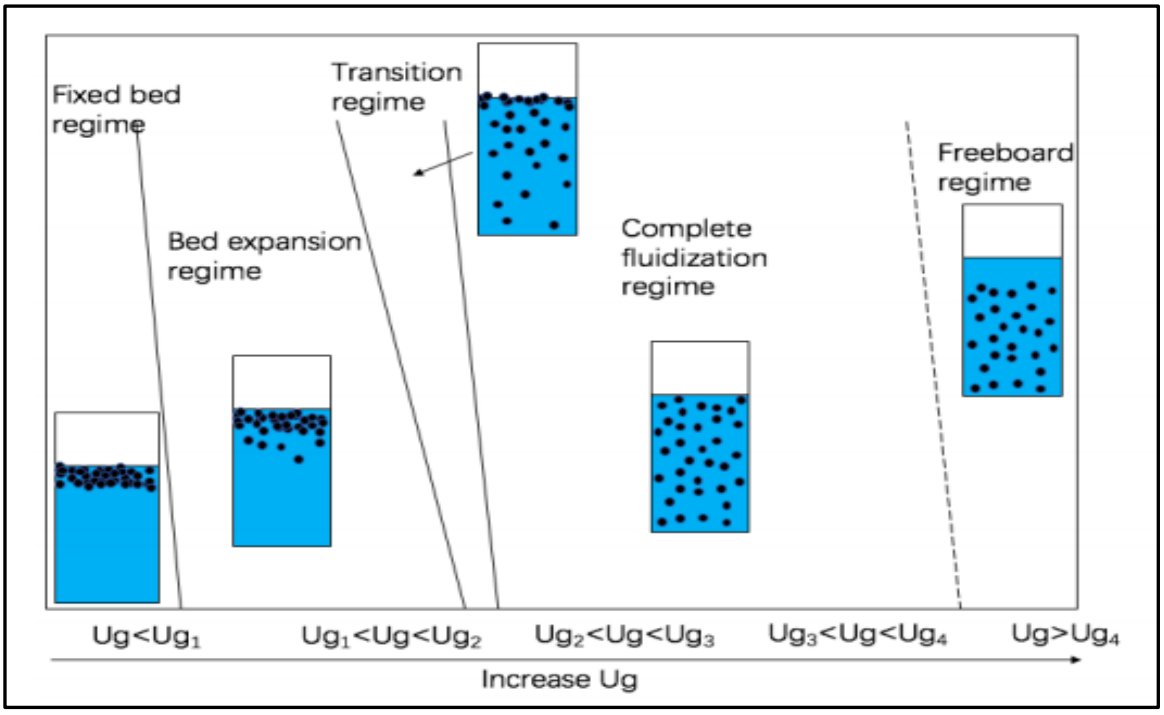

Figure 1.3 Flow regime map of the three-phase bubble column under the batch mode (Sun, 2017)

1.2.1.2 Particle movements

Buffière and Moletta (1999) investigated the influence of the particle size and density on the flow regimes of the inverse fluidized bed under the batch liquid mode. Two types of particles are used in the experiment: one has a mean diameter of 4 mm with density of 920 kg/m^3 and the other one has a mean diameter of 0.175 mm with a density of 690 kg/m^3.

For larger particles with a constant superficial liquid velocity, particles start to settle down and accumulate at the bottom of the reactor when the superficial gas velocity increases which results in a semi-fluidization phenomenon. For smaller particles, it was found that they will distribute uniformly in the reactor when the gas velocity is above a certain value, though the particle density is still smaller than the density of the surrounding liquid-gas mixture. In addition, smaller particles will flow upward with the liquid motion at a high gas velocity, so there is no semi-fluidization for smaller particles at a high gas velocity. In that case, two possible particle expansion mechanisms were proposed: (1) the density difference between particles and liquid-gas mixture and (2) the liquid circulation effect caused by rising bubbles. Later, Renganathan and Krishnaiah (2008) reported the particle expansion mechanism as a combination of the density difference effect and liquid circulation effect. It was indicated that the liquid circulation is not enough to cause the particle movement if the density difference between particles and the liquid-gas mixture is very large for large size particles.

1.2.1.3 Phase holdups

Cho et al. (2002) conducted an experiment to find out the average phase holdup of an inverse TPFB under the continuous operating condition. The results showed the gas and liquid holdups will increase with an increase in the gas and liquid velocities. Later, Bandaru et al. (2007) also reported the same trend for the liquid average holdup. Only a few studies reported the axial distributions of flow parameters for each phase in inverse TPFBs. Ibrahim et al. (1996) and Bandaru et al. (2007) studied the distribution of the axial volume fraction of each phase in an inverse TPFB. It was found that the bed remains fixed at a lower gas and liquid velocity. With the increase in the inlet liquid or gas velocity, the packed bed starts to fluidize, and the particles begin to move downward. The gas phase holdup was eventually found to be uniform along the reactor.

Buffière and Moletta (1999) proposed a correlation to predict the liquid holdup and bed porosity under the batch liquid mode in the inverse TPFB, and it can be used in the dispersed bubble regime and the transition regime. The gas holdup was found to be independent of the liquid velocity, and the gas holdup for large particles is higher than that of small particles under the same superficial gas velocity because the small particles may

not be able to break up the bubble. Sun (2017) reported that the gas holdup increases, and the liquid holdup decreases with a constant solids loading when increasing the superficial gas velocity. In addition, it was also reported that the local solids volume fraction in the axial direction decreases at the top and increases at the bottom of the column gradually with an increase in the superficial gas velocity.

1.2.1.4 Remarks

Only a few researchers studied the fluidization process in inverse TPFBs. Most particles remain packed at the minimum fluidization velocity, and the hysteresis effect between the fluidization and defluidization was also found in inverse TPFBs (D. H. Lee et al., 2000). Renganathan and Krishnaiah (2008) observed that particles expanded layer by layer from the bottom of the packed bed instead of expanding suddenly at the minimum fluidization velocity under the batch liquid operating condition. The bed expansion was found to be heterogeneous first before reaching to the homogeneous expansion state (K. Il Lee et al., 2007). It was also found that the bed expands faster when using heavier particles or increasing gas and liquid velocities in inverse TPFBs.

In an inverse TPFB, the gas is always introduced to the reactor as bubbles, which it is one of the key factors that can influence the heat and mass transfer. Therefore, it is important to study the bubble behavior and properties in order to better understand the flow characteristics of inverse TPFBs. Son et al. (2007) studied bubble properties in an inverse TPFB, and the results showed that the bubble size increases with an increase in the liquid or gas velocity. It was also found that the bubble size and the bubble rising velocity is higher when using the particles with smaller density. The correlation of bubble size, bubble rising velocity, and frequency was proposed based on the gas drift flux. Cho et al. (2002) also reported that the bubble size increases with an increase in the gas velocity.

1.2.2 CFD modelling of multiphase flows in fluidized beds

In past decades, with the rapid development of the computer technology, computational fluid dynamics (CFD) has becomes a powerful tool to simulate multiphase flows as it is more time and economic efficient than experiments. There are two main approaches used

to simulate multiphase flows: (1) Eulerian-Eulerian approach and (2) Eulerian-Lagrangian approach.

The Eulerian-Lagrangian approach treats the liquid and gas as a continuous phase by solving the Navier-Stokes equations, and the solid phase is treated as a discrete phase which can be solved by tracking the trajectories of each particle based on the Lagrangian force balance equation (ANSYS, 2014). Compared to the Eulerian-Eulerian approach, the advantages of the Eulerian-Lagrangian approach are that fewer empirical constitutive relations need to be used and the detailed information of the discrete phase can be obtained. Therefore, many researchers used the Eulerian-Lagrangian approach to investigate the flow characteristics of the discrete phase in micro-scales. Li, Zhang and Fan (1999) studied the single bubble wake behavior and particle entrainment phenomena in a GLS three-phase bubble column by using the VOF-DPM (volume of fluid-discrete phase model) which described the flows of gas bubbles and solid particles in the Lagrangian coordinates and the liquid phase in the Eulerian coordinates. Later, Zhang and Ahmadi (2005) developed a CFD model for the GLS slurry fluidized bed based on the Eulerian-Lagrangian method, and the effect of the bubble size on the flow structure and transient characteristics of the three-phase flows was studied. Wen, Lei and Huang (2005) treated the liquid and gas phases as continuous, and solid phase as the discrete phase to study the hydrodynamics in a TPFB and got a good agreement between the numerical results and experiment data. Since the Eulerian-Lagrangian approach tracks the trajectory of each individual particle, one of the fundamental assumptions made for the Eulerian-Lagrangian model is that the volume fraction of the discrete phase is low (ANSYS, 2014). The computational resource needed for simulating multiphase flows will be high if the discrete phase volume fraction is high (Pan, Chen, Liang, Zhu, & Luo, 2016). Although the Eulerian-Lagrangian method can predict the hydrodynamics of TPFBs accurately and provide more micro-scale information on the discrete phase, the Eulerian-Eulerian method will be used in the present work because the solids volume fraction in an inverse TPFB is high.

The Eulerian-Eulerian approach treats all phases as the interpenetrating continuum, and all phases are solved using governing equations which are closed by additional closure laws and constitutive relations. A turbulence model is used as a closure law to solve the

governing equations for both the gas and liquid phases. Turbulence models used to close the Reynold-averaged Naiver Stokes can be divided into four categories: (1) zero-equation turbulence model; (2) one-equation turbulence model; (2) two-equation turbulence model and (4) RSM (Reynold Stress) turbulence model.

The zero-equation turbulence model is the simplest eddy viscosity model that uses only one algebraic equation to calculate the turbulence viscosity. So, there are no other partial differential equations needed to calculate the turbulent stress. The Prandtl's mixing length theory was the first zero-equation turbulence model developed in 1920s (Prandtl, 1925) based on the Bounsinesq hypothesis (Boussinesq, 1877). But it only considered the mean velocity in a single direction. Later, Cebeci and Smith (1974) and Baldwin and Lomax (1978) extended the model to describe multi-dimensional turbulent flows. The drawbacks of the zero-equation turbulence model are the underestimation of the transport effects, and having difficulties in deriving the turbulence length scale for different types of flows from the empirical data.

The one-equation turbulence model calculates the turbulent eddy viscosity by solving one more transport equation for the turbulent kinetic energy. Spallart and Allmaras (1992) developed a one-equation model, which can predict the free shear and boundary layer flows correctly. The advantage of the one-equation turbulence model is that less computation time is required. However, it also has the same drawback as the zero equation turbulence model in which the accuracy strongly depends on the specified turbulent length scale and time scale of the flow.

Two-equation turbulence models such as the k–ε model turbulence models are more popular than the zero and one-equation turbulence models because they overcome the drawbacks of the zero and one-equation models. The turbulent viscosity can be calculated by solving two additional transport equations for the turbulence kinetic energy and turbulence dissipation rate. Launder, Reece, and Rodi (1975) first developed the standard k–ε turbulence model but it is only valid for high Reynolds number turbulent flows. To be used for low Reynold number flows, the wall function should be used with the standard k–ε turbulence model in order to solve the flow in the near wall region correctly. Yakhot

and Orszag (1986) developed the RNG k–ε model by adding addition terms and functions in the transport equation based on the renormalization group theory. Shih et al. (1995) developed the Realizable k–ε model in order to improve the performance of the standard k –ε model on predicting flows with a high shear rate and massive separation. The model has a new transport equation of dissipation rate related to the vorticity fluctuation at a high Reynolds number and a new formation for the turbulence viscosity based on realizability constraints. Laborde-Boutet et al. (2009) compared the performance of each turbulence models by predicting the turbulent flow characteristics in bubble columns. The results showed that the RNG k–ε has a better performance than the standard and realizable k–ε models. The study also investigated the influence of using different turbulence models, the dispersed k–ε model, dispersed k –ε model with bubble induce effect and per phase k –ε model to account for the effect of the gas phase turbulence on the liquid phase turbulence. The results showed there is no influence on the predicted velocity filed, but the turbulent quantities are higher when accounting for the bubble induced turbulence. Masood and Delgado (2014) reported that both the dispersed RNG k –ε model and dispersed RNG k –ε model with bubble induced turbulence can predict the average velocity and turbulent accurately in a 3D square bubble column. Hamidipour, Chen, and Larachi (2012) extended the study to a three-phase bubble column and found the dispersed RNG k –ε has a better performance on predicting the flow field in TPFBs bed than the per-phase RNG k –ε model, realizable standard k –ε model and standard k –ε model.

The RSM model is a second closure model, which closes governing equations by solving the transport equation of Reynold stresses instead of calculating the eddy viscosity. The RSM model has better performance on predicting the anisotropic flows than all other turbulence models mentioned above. The drawback of the RSM is the computation expense is high. Therefore, two equation turbulence models are used in the simulation of the multiphase fluidization in present work.

For the solid phase, the kinetic theory of granular flow (KTGP) proposed by Chapman and Cowling (1970) is used to model the solid phase pressure, viscosity and stress in order to close the RANS equation. In the KTGP, the random motion of particles caused by particle-

particle collision can be analogous to the random motion of gas molecules in a thermodynamic system. The granular temperature is defined analogous to the temperature in a thermodynamic system, which is related the particle velocity fluctuation. The solids phase viscosity and stress are the functions of the granular temperature. Ding and Gidaspow (1990) modelled the gas-solid fluidization by using the KTGP. Later, some researchers also used the KTGP for the solid phase when modeling three-phase fluidization (Hamidipour et al., 2012; W. Li & Zhong, 2015; Wu & Gidaspow, 2000). Johnson and Jackson boundary condition (Johnson & Jackson, 1987) was often used for the solid phase to account for the collisions between the wall and particle, and the specularity coefficient is an empirical parameter to define the wall condition. The specularity coefficient can vary from zero to one where one represents the no-slip wall condition which means significant amount of lateral momentum transfer existed at wall, and zero represents the free-slip wall condition which means there is no shear at the wall.

For the three-phase fluidization modelling, the Eulerian-Eulerian approach can be categorized into two types which are the pseudo two-fluid model and three-fluid Eulerian-Eulerian approach. The pseudo two-fluid model can be used for modeling the three-phase fluidization only when the gas bubble is smaller than the particle size and uniformly distributed along the column because the gas phase and fluid phase can be considered as a single mixed fluid phase (Felice, 2000). In addition, the two-fluid model is also applied to the three-phase fluidization when the particle size is small enough, the loading is low and the slip velocity between the solid and liquid phases is small. In that case, the liquid and solid suspension can be simplified to one-phase, and it is often used in the three-phase slurry bubble column simulation (Grevskott, Sannaes, Dudukovic, Hjarbo, & Svendsen, 1996; Hillmer & Weismantel, 1994; Wen & Xu, 1998). In addition, Feng et al. (2005) employed a pseudo two fluid model to the gas–liquid-nanoparticles three-phase fluidization process, and the results was validated with the experimental data and the agreement was strong. By applying the pseudo two-fluid model for the three-phase simulation, the complicated three-phase flows can be simplified to a two-phase flow, which reduces the computation expanse as well. However, the drawback of the pseudo two-fluid model is that the application is limited by the particle size and particle loading, and it also neglects the interaction between the two phases. Therefore, the three-fluid Eulerian-

Eulerian approach will be used because of the large particle size used in the present study. Only a few literatures presented the CFD modelling based on the three-fluid Eulerian-Eulerian model as the interactions among each phase is complicated in TPFBs.

Panneerselvam, Savithri, and Surender (2009) developed a CFD model for TPFBs based on the three-fluid Eulerian approach. Two different reactors were used to validate the model, and the particle densities are 2475 kg/m^3 and 2500 kg/m^3. The dispersed standard k −ε turbulence model combined with the bubble and gas induced turbulence model on liquid was applied to the liquid phase. The constant viscosity model (Gidaspow, 1994) instead of the KTGP was used to describe the solid pressure and stress. Only the drag force was considered as the interaction force among each phase to calculate the momentum exchange coefficient. The drag model used between the liquid and solid phases is the Gidaspow drag model (Gidaspow, 1994). For the liquid and gas phases, the Tomiyama drag model (Tomiyama, 1998) and Grace drag models (Grace, 1973) were used, and the Tomiyama drag model gives a better performance by comparing the experimental results. The drag model used for the gas and particle phases in this study was the Schiller-Naumann drag model (Schiller & Naumann, 1935). The no-slip wall boundary condition for the liquid phase and free slip condition for the gas and solid phases were selected. The velocity inlet and pressure outlet were selected as boundary conditions. The mean bubble size is used without considering the bubble size distribution in their study (Panneerselvam et al., 2009), and it was determined by comparing the gas holdup derived from the CFD results using different bubble sizes with the average gas holdup from the experiment data. The simulation results showed a good agreement on the axial gas hold, axial solids velocity, and turbulence quantities such as turbulent velocity and shear stress with the experimental data. However, the model cannot predict the near wall region correctly.

Hamidipour et al. (2012) presented a CFD model based on a three-fluid model combined with the KTGP in the same TPFBs as Panneerselvam et al. (2009) to investigate the performance of different turbulence models and solid wall conditions. A single bubble size distribution assumption was made in this study. The results showed the dispersed RNG k–ε model gives a better performance on predicting the axial solids velocity and gas velocity than the other k–ε models. According to this study, it was also found that both the three-

dimension and two-dimensional models are capable of predicting the flow field, but the three-dimensional model is slightly accurate than the two-dimensional model. However, the computational cost of the three- dimensional simulation is also high. The no-slip wall condition for the liquid phase, free-slip for the gas and solids phases were recommended. The bubble size input for the second phase was found to have an influence on the gas holdup, and the smaller bubble size resulted in a higher gas holdup. Also, the interphase force between the continuous and dispersed phases has been studied widely in literatures, but the interaction between two dispersed phases has not been well understand and modeled. Hamidipour et al. (2012) used the same method to model the drag force between the two dispersed phases to model the drag force between the continuous and dispersed phases because two dispersed phases were also treated as continuums in the Eulerian-Eulerian approach. The drag model used between the gas and solid phases was the Schiller-Naumann drag model (Schiller & Naumann, 1935), between the solid and liquid phase was the Gidaspow drag model (Gidaspow, 1994), between the liquid and gas phase was also the Schiller-Naumann model (Schiller & Naumann, 1935).

Li and Zhong (2015) did the CFD modeling using the three-fluid Eulerian-Eulerian approach with the KTGP to investigate the hydrodynamics of the three-phase phase bubble columns. The dispersed RNG model was used for the liquid phase. A mean bubble size was applied even under different superficial gas velocities. The sensitivity of the interphase force, which includes the drag force, was studied. It was found the best drag model for the liquid and gas phases is the Zhang-Vanderheyden model (Zhang & Vanderheyden, 2002), between liquid and solid phases is the Schiller-Naumann drag model (Schiller & Naumann, 1935), and the drag force between the gas and solid phases were not considered. The effect of the superficial gas velocity, particle density, solids loading and particle size on the hydrodynamics of the three-phase bubble column is investigated based on the CFD results.

According to literatures, very few works were focused on developing CFD model based on three-fluid Eulerian-Eulerian approach for the three-phase fluidization process, and most of the CFD models are for upward TPFBs. No CFD model for the inverse three-phase fluidization process with light particle has been reported in the literature. Only very few studies which relate to the CFD modeling of the hydrodynamics of inverse two-phase

fluidized bed has been reported. The following literature review is about liquid-solid inverse fluidized beds.

A numerical simulation based on the Eulerian-Eulerian approach has been carried out to study the flow behavior of particles in the inverse liquid-solid fluidization process by Wang et al. (2014). The dispersed standard k –ε turbulence model for the liquid phase and KTGP for the solid phase were applied. The Gidaspow drag model is used to determine the interphase momentum exchange coefficient. The no-slip wall condition was used for both the liquid and solid phases. The particle density was 897 kg/m3 which is lower than the surrounding liquid phase density. The predicted bed expansion was slightly higher than the experimental value. The effects of the liquid velocity on the bed height, solid phase distribution and flow patterns of particles were investigated. Further improvement of the drag model is needed to enhance the performance of CFD model in inverse liquid-solid fluidized beds.

Wang et al. (2018) developed a CFD model for inverse liquid-solid fluidized beds based on the Eulerian-Larganrain approach. The effects of the particle velocity, jet velocity and liquid viscosity on the particle flow behavior was studied. The results indicated that the solid distribution was denser at the bottom of the column for heavily particles than light particles in an inverse liquid-solid fluidized bed. It was also found that a higher particles restitution coefficient will give a higher bed expansion height.

1.3 Objectives

According to the literature review presented in the previous section, it is noticed that the hydrodynamics of the inverse fluidized bed has been studied experimentally by many researchers, but most studies were focused on the flow characteristics, such as the average phase holdup, axial phase holdup, and minimum fluidization velocity. However, few of them reported the details of the flow patterns and local flow characteristics such as local radial phase holdup, radial solid phase velocity and etc. In addition, few researchers investigated the development process of the inverse three-phase fluidization process.

For CFD models, only a few models were developed and validated for the three-phase fluidization process based on the three-fluid Eulerian-Eulerian approach. The complicated interactions between each phase are still not well understood, and there is no clear guideline to follow when setting up a CFD model for the simulation of the three-phase fluidization process. In addition, there is no CFD model developed for inverse TPFBs from literatures. The mean bubble size is assumed to be constant even under different superficial gas or liquid velocities operating condition from literatures. However, in reality, the mean bubble size varies with the superficial gas velocity.

The first objective of the present work is to develop a CFD model for the simulation of the inverse TPFB based on the three-fluid Eulerian-Eulerian approach in order to study the flow details and fluidization development process in the inverse TPFB, which have not been reported by experimental studies. The second objective is to further modify the proposed CFD model by using different mean bubble sizes under different inlet superficial gas velocities. In addition, a correlation between the bubble size and inlet superficial gas velocity in the inverse TPFB will be developed.

1.4 Thesis structure

The thesis is in the “Integrated-Article Format”.

Chapter1: General background and literature review on CFD modelling and experiment study of the three-phase fluidization process is presented.

Chapter2: A CFD model is developed for the simulation of the inverse TPFB. The development of the fluidization process and the effect of the operating condition on the hydrodynamics and flow structure are investigated.

Chapter3: The CFD model proposed in chapter 2 is modified based on the mean bubble size adjustment and the correlation for the bubble size.

Chapter4: Conclusions and recommendations for future work are presented.

Reference

Ansys. Inc. (2014). Fluent 16.0 User's Guide.

Baldwin, B., & Lomax, H. (1978). Thin-layer approximation and algebraic model for separated turbulentflows. In *16th Aerospace Sciences Meeting*. American Institute of Aeronautics and Astronautics. https://doi.org/10.2514/6.1978-257

Bandaru, K. S. V. S. R., Murthy, D. V. S., & Krishnaiah, K. (2007). Some hydrodynamic aspects of 3-phase inverse fluidized bed. *China Particuology*, *5*(5), 351–356. https://doi.org/https://doi.org/10.1016/j.cpart.2007.06.002

Boussinesq, J. (1877). Essai sur la theorie des eaux courantes. *Mémoires Présentés Par Divers Savants à l'Acad. Des Sci. Inst. Nat. France*, *23*(1), 1–680.

Briens, C. L., Ibrahim, Y. A. A., Margaritis, A., & Bergougnou, M. A. (1999). Effect of coalescence inhibitors on the performance of three-phase inverse fluidized-bed columns. *Chemical Engineering Science*, *54*(21), 4975–4980. https://doi.org/10.1016/S0009-2509(99)00220-1

Buffière, P., & Moletta, R. (1999). Some hydrodynamic characteristics of inverse three phase fluidized-bed reactors. *Chemical Engineering Science*, *54*(9), 1233–1242. https://doi.org/10.1016/S0009-2509(98)00436-9

Cebeci, T., & Smith, A. M. O. (1974). *Analysis of turbulent boundary layers*. (A. M. O. Smith, Ed.). New York: Academic Press.

Chapman, S., & Cowling, F. (1991). *The Mathematical Theory of Non-uniform Gases An Account of the Kinetic Theory of Viscosity , Thermal Conduction and Diffusion in Gases*. Cambridge University Press. https://doi.org/10.1039/c3cp54368d

Cho, Y. J., Park, H. Y., Kim, S. W., Kang, Y., & Kim, S. D. (2002). Heat transfer and hydrodynamics in two- and three-phase inverse fluidized beds. *Industrial and Engineering Chemistry Research*, *41*(8), 2058–2063. https://doi.org/10.1021/ie0108393

Comte, M. P., Bastoul, D., Hebrard, G., Roustan, M., & Lazarova, V. (1997). Hydrodynamics of a three-phase fluidized bed - The inverse turbulent bed. *Chemical Engineering Science*, *52*(21–22), 3971–3977. https://doi.org/10.1016/S0009-2509(97)00240-6

Ding, J., & Gidaspow, D. (1990). A bubbling fluidization model using kinetic theory of granular flow. *AIChE Journal*, *36*(4), 523–538. https://doi.org/10.1002/aic.690360404

Fan, L. S., Muroyama, K., & Chern, S. H. (1982). Hydrodynamic characteristics of inverse fluidization in liquid-solid and gas-liquid-solid systems. *The Chemical Engineering Journal*, *24*(2), 143–150. https://doi.org/10.1016/0300-9467(82)80029-4

Felice, R. Di. (2000). The pseudo-fluid model applied to three-phase fluidisation. *Chemical Engineering Science*, *55*(18), 3899–3906. https://doi.org/https://doi.org/10.1016/S0009-2509(00)00027-0

Feng, W., Wen, J., Fan, J., Yuan, Q., Jia, X., & Sun, Y. (2005). Local hydrodynamics of gas–liquid-nanoparticles three-phase fluidization. *Chemical Engineering Science*, *60*(24), 6887–6898. https://doi.org/https://doi.org/10.1016/j.ces.2005.06.006

Gidaspow, D. (1994). *Multiphase Flow and Fluidization: Continuu and Kinetic Theory Descriptions*. Boston: Acad. Press.

Grace, J. R. (1973). Shapes and velocities of bubbles rising in infinite liquids. *Transactions of the Institution of Chemical Engineers*, *51*, 116–120. Retrieved from http://ci.nii.ac.jp/naid/10021836141/en/

Grace, J. R. (1986). Contacting modes and behaviour classification of gas—solid and other two- phase suspensions. *The Canadian Journal of Chemical Engineering*, *64*(3), 353–363. https://doi.org/10.1002/cjce.5450640301

Grevskott, S., Sannaes, B. H., Dudukovic, M. P., Hjarbo, K. W., & Svendsen, H. F. (1996). Liquid circulation, bubble size distributions, and solid movement in two- and three-phase bubble columns. *Chemical Engineering Science*, *51*(10), 1703. https://doi.org/https://doi.org/10.1016/0009-2509(96)00029-2

Hamidipour, M., Chen, J., & Larachi, F. (2012). CFD study on hydrodynamics in three-phase fluidized beds — Application of turbulence models and experimental validation. *Chemical Engineering Science*, *78*, 167–180. https://doi.org/10.1016/j.ces.2012.05.016

Han, H., Lee, W., Kim, Y., Kwon, J., Choi, H., Kang, Y., & Kim, S. (2003). Phase Hold-up and Critical Fluidization Velocity in a Three-Phase Inverse Fluidized Bed. *Korean J. Chem. Eng.*, *20*(1), 163–168. https://doi.org/10.1007/BF02697203

Hillmer, G., & Weismantel, L. (1994). Investigations and Modelling Columns of Slurry Bubble. *Science*, *49*(6), 837–843. https://doi.org/https://doi.org/10.1016/0009-2509(94)80020-0

Ibrahim, Y. A. A., Briens, C. L., Margaritis, A., & Bergongnou, M. A. (1996). Hydrodynamic Characteristics of a Three-Phase Inverse Fluidized-Bed Column. *AIChE Journal*, *42*(7), 1889–1900. https://doi.org/10.1002/aic.690420710

Il Lee, K., Mo Son, S., Yeong Kim, U., Kang, Y., Hwan Kang, S., Done Kim, S., … Hyun Kim, W. (2007). Particle dispersion in viscous three-phase inverse fluidized beds. *Chemical Engineering Science*, *62*(24), 7060–7067. https://doi.org/10.1016/j.ces.2007.08.024

Johnson, P. C., & Jackson, R. (1987). Frictional-collisional constitutive relations for granular materials, with application to plane shearing. *Journal of Fluid Mechanics*,

176, 67–93. https://doi.org/10.1017/S0022112087000570

Laborde-Boutet, C., Larachi, F., Dromard, N., Delsart, O., & Schweich, D. (2009). CFD simulation of bubble column flows: Investigations on turbulence models in RANS approach. *Chemical Engineering Science*, *64*(21), 4399–4413. https://doi.org/10.1016/j.ces.2009.07.009

Launder, B. E., Reece, G. J., & Rodi, W. (1975). Progress in the development of a Reynolds-stress turbulence closure. *Journal of Fluid Mechanics*, *68*(3), 537–566. https://doi.org/10.1017/S0022112075001814

Lee, D. H., Epstein, N., & Grace, J. R. (2000). Hydrodynamic Transition from Fixed to Fully Fluidized Beds for Three-Phase Inverse Fluidization. *Korean Journal of Chemical Engineering*, *17*(6), 684–690. https://doi.org/10.1007/BF02699118

Li, W., & Zhong, W. (2015). CFD simulation of hydrodynamics of gas-liquid-solid three-phase bubble column. *Powder Technology*, *286*, 766–788. https://doi.org/10.1016/j.powtec.2015.09.028

Li, Y., Zhang, J., & Fan, L.-S. (1999). Numerical simulation of gas–liquid–solid fluidization systems using a combined CFD-VOF-DPM method: bubble wake behavior. *Chemical Engineering Science*, *54*(21), 5101–5107. https://doi.org/https://doi.org/10.1016/S0009-2509(99)00263-8

Masood, R. M. A., & Delgado, A. (2014). Numerical investigation of the interphase forces and turbulence closure in 3D square bubble columns. *Chemical Engineering Science*, *108*, 154–168. https://doi.org/10.1016/j.ces.2014.01.004

Muroyama, K., & Fan, L. - S. (1985). Fundamentals of gas- liquid- solid fluidization. *AIChE Journal*, *31*(1), 1–34. https://doi.org/10.1002/aic.690310102

Ostergaard, K. (1971). Three-phase fluidization. In J. F. Davidson & D. Harrison (Eds.), *Fluidization* (pp. 751–780). Academic Press London.

Pan, H., Chen, X., Liang, X., Zhu, L., & Luo, Z. (2016). CFD simulations of gas – liquid – solid flow in fluidized bed reactors — A review. *Powder Technology*, *299*, 235–258. https://doi.org/https://doi.org/10.1016/j.powtec.2016.05.024

Panneerselvam, R., Savithri, S., & Surender, G. D. (2009). CFD simulation of hydrodynamics of gas–liquid–solid fluidised bed reactor. *Chemical Engineering Science*, *64*(6), 1119–1135. https://doi.org/https://doi.org/10.1016/j.ces.2008.10.052

Prandtl, L. (1925). Uber die ausgebildete Turbulenz. *Zamm*, *Vol. 5*(5), 136–139. https://doi.org/10.1007/978-3-662-11836-8_60

Renganathan, T., & Krishnaiah, K. (2008). Prediction of Minimum Fluidization Velocity in Two and Three Phase Inverse Fluidized Beds. *The Canadian Journal of Chemical Engineering*, *81*(3–4), 853–860.

https://doi.org/https://doi.org/10.1002/cjce.5450810369.

Schiller, L., & Naumann, A. (1935). A drag coefficient correlation. *Z. Ver. Deutsch. Ing*, *77*, 318–320.

Shih, T.-H., Liou, W. W., Shabbir, A., Yang, Z., & Zhu, J. (1995). A new eddy viscosity model for high Reynolds number turbulent flows. *Computers and Fluids*, *24*(3), 227–238. https://doi.org/10.1016/0045-7930(94)00032-T

Sokół, W., & Korpal, W. (2006). Aerobic treatment of wastewaters in the inverse fluidised bed biofilm reactor. *Chemical Engineering Journal*, *118*(3), 199–205. https://doi.org/10.1016/j.cej.2005.11.013

Son, S. M., Kang, S. H., Kim, U. Y., Kang, Y., & Kim, S. D. (2007). Bubble properties in three-phase inverse fluidized beds with viscous liquid medium. *Chemical Engineering and Processing: Process Intensification*, *46*(8), 736–741. https://doi.org/10.1016/j.cep.2006.10.002

SPALART, P., & ALLMARAS, S. (1992). A one-equation turbulence model for aerodynamic flows. In *30th Aerospace Sciences Meeting and Exhibit*. American Institute of Aeronautics and Astronautics. https://doi.org/10.2514/6.1992-439

Sun, X. (2017). *Bubble induced Inverse Gas-liquid-solid Fluidized bed*. University of Western Ontario.

Tomiyama, A. (1998). Struggle with computational bubble dynamics. *Multiphase Science and Technology*. https://doi.org/10.1615/MultScienTechn.v10.i4.40

Wang, S., Li, H., Wang, R., Tian, R., Sun, Q., & Ma, Y. (2018). Numerical simulation of flow behavior of particles in a porous media based on CFD-DEM. *Journal of Petroleum Science and Engineering*, *171*, 140–152. https://doi.org/10.1016/j.petrol.2018.07.039

Wang, S., Sun, J., Yang, Q., Zhao, Y., Gao, J., & Liu, Y. (2014). Numerical simulation of flow behavior of particles in an inverse liquid–solid fluidized bed. *Powder Technology*, *261*, 14–21. https://doi.org/https://doi.org/10.1016/j.powtec.2014.04.017

Wen, J., Lei, P., & Huang, L. (2005). Modeling and simulation of gas-liquid-solid three-phase fluidization. *Chemical Engineering Communications*, *192*(7–9), 941–955. https://doi.org/10.1080/009864490511175

Wen, J., & Xu, S. (1998). Local hydrodynamics in a gas-liquid-solid bubble column reactor. *Science*, *70*(97), 81–84. https://doi.org/https://doi.org/10.1016/S1385-8947(97)00120-4

Werther, J., Hartge, E. U., & Heinrich, S. (2014). Fluidized-bed reactors-status and some development perspectives. *Chem. Ing. Tech.*, *86*(12), 2022–2038.

https://doi.org/doi:10.1002/cite.201400117

Wu, Y., & Gidaspow, D. (2000). Hydrodynamic simulation of methanol synthesis in gas-liquid slurry bubble column reactors. *Chemical Engineering Science*, *55*(3), 573–587. https://doi.org/https://doi.org/10.1016/S0009-2509(99)00313-9

Yakhot, V., & Orszag, S. A. (1986). Renormalization group analysis of turbulence. I. Basic theory. *Journal of Scientific Computing*, *1*(1), 3–51. https://doi.org/10.1007/BF01061452

Zhang, D. Z., & Vanderheyden, W. B. (2002). The effects of mesoscale structures on the disperse two-phase flows and their closures for dilute suspensions . *Int. J. Multiphase Flows*, *28*(5), 805–822. https://doi.org/https://doi.org/10.1016/S0301-9322(02)00005-8

Zhang, J. P., Grace, J. R., Epstein, N., & Lim, K. S. (1997). Flow regime identification in gas-liquid flow and three-phase fluidized beds. In *Chemical Engineering Science* (Vol. 52, pp. 3979–3992). Pergamon. https://doi.org/10.1016/S0009-2509(97)00241-8

Zhang, X., & Ahmadi, G. (2005). Eulerian–Lagrangian simulations of liquid–gas–solid flows in three-phase slurry reactors. *Chemical Engineering Science*, *60*(18), 5089–5104. https://doi.org/https://doi.org/10.1016/j.ces.2005.04.033

Zhu, Z., Na, Y., & Lu, Q. (2007). Effect of pressure on minimum fluidization velocity. *Journal of Thermal Science*, *16*(3), 264–269. https://doi.org/10.1007/s11630-007-0264-2

Chapter 2

2 A CFD Model for the Simulation of the Inverse Gas-Liquid-Solid Fluidized Bed

2.1 Introduction

Fluidization is a process that can convert particle behavior from the solid state to a fluid state by introducing liquid or gas flow into the system. Fluidized beds can be categorized as the liquid-solid fluidization, gas-solid fluidization and gas-liquid-solid three-phase fluidization using different fluidizing agents. Due to the higher contact efficiency among each phase and good mass and heat transfer features, gas-liquid-solid three-phase fluidized beds (TPFBs) have the potential to be used in chemical, biochemical, and petrochemical industries since past decades (Muroyama & Fan, 1985). In addition, fluidized beds can be further divided into upward fluidized beds and inverse fluidized beds based on the flow direction of the fluidizing agent. The inverse gas-liquid-solid TPFBs can be operated under the continuous mode or batch mode. Under the batch mode, the liquid velocity is zero, and the fluidization state of the system can be achieved by increasing the gas velocity. In inverse TPFBs, the particle density is usually smaller than the liquid density, so fluidization will begin when the drag force and gravity of particles can balance with the buoyancy force when increasing the liquid or gas velocity. Comparing to the traditional upward three-phase fluidization, inverse three-phase fluidization possesses some advantages such as lower energy cost and minimum solids attrition.

The hydrodynamics and flow patterns in inverse fluidized beds have been studied by a few researchers. The flow regimes in inverse fluidized beds are defined as the fixed bed with dispersed bubble regime, bubbling fluidized bed regime, transition regime and slugging fluidized bed regime with an increase in the liquid velocity or gas velocity (Fan et al., 1982). Three significant transition superficial gas velocities have been defined based on the solid phase distribution in the inverse fluidized bed under the batch liquid mode to distinguish the flow regimes, being (1) the minimum gas fluidization velocity (U_{g1}) that can break the fixed bed, (2) the velocity (U_{g2}) that can let some particles reach the bottom of the reactor, and (3) the velocity (U_{g3}) that can distribute particles uniformly along the reactor (Comte

et al., 1997; Sun, 2017). It was found that U_{g2} and U_{g3} will decrease when increasing the solids loading or particle density.

A few researchers experimentally investigated the hydrodynamics, such as the minimum fluidization velocity and phase holdup in inverse TPFBs. The minimum liquid fluidization velocity decreased with an increase in the gas flowrate, and the gas and liquid holdup was found to increase with the increase in the gas and liquid velocities (Bandaru et al., 2007; Cho et al., 2002; D. H. Lee et al., 2000). Renganathan & Krishnaiah (2008) developed a correlation, which can predict the minimum fluidization velocity in the inverse TPFB under both the batch mode and continuous mode. The solids holdup was found to become denser at the lower part of the column and dilute at the upper part of the column when increasing the liquid or gas velocity, and the gas holdup is distributed uniformly along the axial direction of the column (Bandaru et al., 2007; Ibrahim et al., 1996; Sun, 2017). The solid phase expansion in the inverse TPFB is due to the combination of the density difference and liquid circulation, and it was also found particles are easier to be fluidized when their density is close to the gas-liquid mixture density (Buffière & Moletta, 1999).

Despite a few experimental studies on the hydrodynamics and flow structure conducted, the understanding of the hydrodynamics of inverse TPFBs is still limited. For instance, no studies were found in the literatures that reported the hydrodynamics of an inverse TPFB in the radial direction. CFD has become a powerful tool to study the multi-phase flows in fluidized beds due to the rapid development of computer technology in past decades. Therefore, a numerical study on the hydrodynamics of an inverse fluidized bed will be conducted in the present study in order to better understand the flow patterns and hydrodynamics in the inverse TPFB under the batch mode.

Two main methods are usually used to simulate flows in fluidized beds, which are the Eulerian-Lagrangian approach and Eulerian-Eulerian approach. In the Eulerian-Lagrangian approach, the liquid phase is treated as the continuous phase and the solid phase is treated as the discrete phase in which each individual particle is tracked by solving the Lagrangian force balance equation. The Eulerian-Lagrangian approach is typically used when the volume fraction of the discrete phase is low to study the single bubble and particle

behavior in the TPFB (Y. Li et al., 1999). When the volume fraction of the discrete phase is high, the Eulerian-Eulerian approach is preferred. Therefore, the Eulerian-Eulerian approach will be used in present study since the volume fraction of particles in an inverse three-phase fluidized bed is high.

The Eulerian-Eulerian approach treats all phases as an interpenetrating continuum, and the governing equations are solved for each phase with additional closure law and constative relations. The kinetic theory of the granular flow (Ding & Gidaspow, 1990; Hamidipour et al., 2012; W. Li & Zhong, 2015; Wu & Gidaspow, 2000) is used to calculate the solid phase pressure, viscosity and stress. The Eulerian-Eulerian approach can be divided into the pseudo two-fluid Eulerian model and three-fluid Eulerian-Eulerian model for the three-phase flows. For the pseudo two-fluid Eulerian model, the liquid-solid or liquid-gas can be treated as one mixed phase when the particle or bubble size is small, volume fraction of the solid or gas phase is low and the slip velocity between the two phases is low. Therefore, the three-phase flows can be simplified to a two-phase flows, which is often used to simulate the flow in the three-phase slurry fluidized bed or the fluidized bed that used nanoparticles as solid phase (Feng et al., 2005; Grevskott et al., 1996; Hillmer & Weismantel, 1994; Wen & Xu, 1998). Due to the limitation of the pseudo two-fluid model, the three-fluid Eulerian-Eulerian model is used in present study to simulate the three-phase flows in a fluidized bed under the batch operating mode.

Comparing to the traditional upward two-phase flows in fluidized beds, fewer researchers have been done the numerical study on hydrodynamics in TPFBs. Panneerselvam et al. (2009) developed a CFD model to simulate gas-liquid-solid fluidized beds based on the three-fluid Eulerian-Eulerian approach, and the results shows a good agreement with the experimental data except at the near wall region. Hamidipour et al. (2012) presented a CFD model based on the three-fluid Eulerian-Eulerian approach and kinetic theory of the granular flow to investigate the performance of different turbulence models and wall boundary conditions for the solid phase. It was found the dispersed RNG $k-\varepsilon$ model has the best performance. Li and Zhong (2015) studied the performance of different drag models in TPFBs. It was found the best drag model for the liquid and gas phases is the Zhang-Vanderheyden model (Zhang & Vanderheyden, 2002), between the liquid and solid

phases is the Schiller-Naumann drag model (Schiller & Naumann, 1935), and the drag force between the gas and solid phases were not considered.

No CFD studies on inverse TPFBs were found in the literatures. Therefore, the objective of this study is to develop a CFD model based on the three-fluid Eulerian-Eulerian approach with the kinetic theory of the granular flow for an inverse TPFB in order to better understand the hydrodynamics and flow patterns within it.

2.2 Experimental setup of the inverse three-phase fluidized bed

The proposed CFD model will be validated based on the he experimental work done by Sun (2017). The schematic diagram of the experiment set up is shown in Figure 2.1. The column is made of PVC with 0.153 m in diameter and 3 m in height. The ring-shape porous quartz gas distributor with an 8.7 cm outer diameter and a 2.7 cm inner diameter which can generate very small bubbles, is placed at the bottom of the column. The tap water, air and particles are used as the liquid, gas and solid phases, respectively, in the experiment. Three types of particles with different densities (904 kg/m^3, 930 kg/m^3 and 950 kg/m^3) are used. Before the experiment begins, tap water and particles are injected into the column. The particles rise to the surface as the particle density is lower than the liquid density. During the experiment, only the gas is continuously introduced into the column through the gas distributor, and there are no inlets and outlets for particles and liquid. The superficial velocity of the gas at the inlet is from 0mm/s to 60mm/s. The experiment is carried out under ambient temperature and pressure.

In this study, the simulation of the three-phase flows in the inverse TPFB will be carried out under different operating conditions, such as different particle densities, inlet superficial gas velocities, and solids loadings, in order to study the hydrodynamics and flow structures in the inverse TPFB. The summary of the operating conditions and properties of each phase are shown in Table 2.1.

1	**Column**
2	**Bubble**
3	**Liquid**
4	**Solid particles**
5	**Rotameters**
6	**Pressure gauge**
7	**Gas distributor**
8	**Liquid inlet/outlet valve**
9	**Manometer**

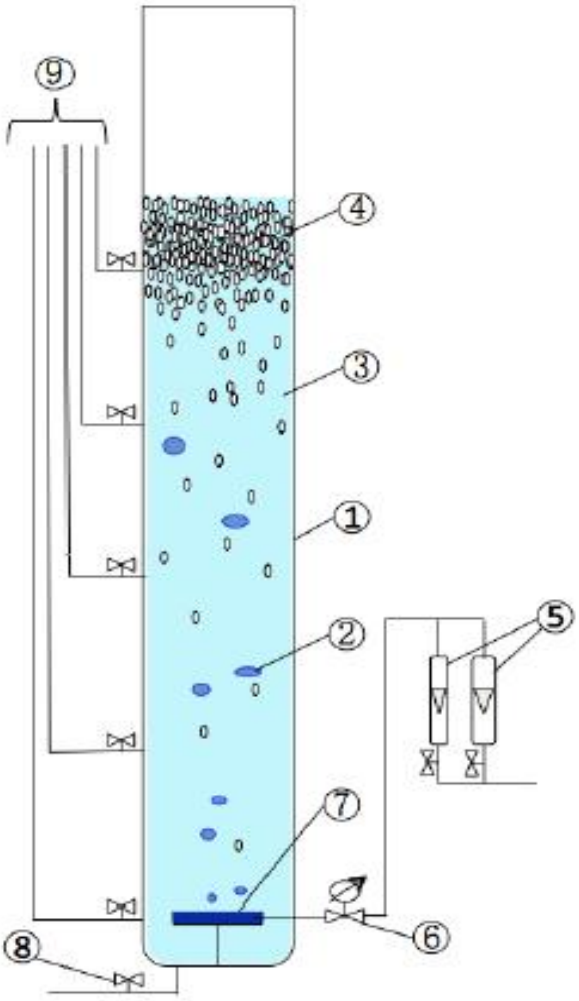

Figure 2.1 Configuration of the experimental setup of the inverse three-phase fluidized bed (Sun, 2017)

Table2.1 Operating conditions and physical properties of the liquid, gas and solid phases

Sun (2017)	Bubble column size (m)	Diameter: 0.153
		Total height: 3
	U_l (mm/s)	0
	U_g (mm/s)	9, 12.5, 15, 20, 40
	U_s (mm/s)	0
	Liquid phase	Water
	Liquid phase density ($kg/m^{3)}$	998
	Liquid phase viscosity ($kg/m^{-s)}$	0.001003
	Gas phase	Air
	Gas phase density ($kg/m^{3)}$	1.225
	Gas phase viscosity (kg/m^{-s})	1.7984×10^{-5}
	Solid phase	Polypropylene, polyethylene
	Particle diameter (mm)	3.5, 4.6
	Particle density ($kg/m^{3)}$	904, 930, 950
	Solid phase loading	5%, 15%, 20%
	Pressure	Atmospheric pressure
	Temperature	Ambient temperature

2.3 Numerical models

The CFD model developed in this study to simulate the inverse gas-liquid-solid three-phase fluidized bed is based on the three-fluid Eulerian-Eulerian approach. Each phase is treated as interpenetrating continuum. A turbulence model coupled with the kinetic theory of the granular flow is used to close the governing equations. The liquid phase is set as the primary phase, and the gas and solid phases are considered as the secondary phases in the simulation. The governing equation for each phase and corresponding closure law and constitutive relations are shown as following.

2.3.1 Governing equations

Conservation equation of mass for the liquid phase

$$\frac{\partial}{\partial t}(\alpha_l \rho_l) + \nabla\,(\alpha_l \rho_l \overrightarrow{v_l}) = 0 \tag{1}$$

Conservation equation of mass for the gas phase

$$\frac{\partial}{\partial t}\left(\alpha_g \rho_g\right) + \nabla\left(\alpha_g \rho_g \overrightarrow{v_g}\right) = 0 \tag{2}$$

Conservation equation of mass for the solid phase

$$\frac{\partial}{\partial t}(\alpha_s \rho_s) + \nabla\,(\alpha_s \rho_s \overrightarrow{v_s}) = 0 \tag{3}$$

where α, ρ, and v are the volume fraction, density and velocity of each phase. The subscript of l, g land s represent liquid, gas and solid phase respectively. The sum of volume fraction for each phase should be equal to one.

$$\alpha_l + \alpha_g + \alpha_s = 1 \tag{4}$$

Conservation equation of momentum for the liquid phase

$$\frac{\partial}{\partial t}(\alpha_l \rho_l \overrightarrow{v_l}) + \nabla\,(\alpha_l \rho_l \overrightarrow{v_l}\,\overrightarrow{v_l}) = -\,\alpha_l \nabla p + \nabla\,\overline{\overline{\tau_l}} + \alpha_l \rho_l \vec{\mathrm{g}} + M_l \tag{5}$$

$$\overline{\overline{\tau_l}} = \alpha_l \mu_l \left(\nabla\,\overrightarrow{v_l} + \nabla \overrightarrow{v_l}^{T}\right) - \alpha_l \frac{2}{3} \mu_l (\nabla\,\overrightarrow{v_l})\bar{\bar{I}} \tag{6}$$

Conservation equation of momentum for the gas phase

$$\frac{\partial}{\partial t}\left(\alpha_g \rho_g \overrightarrow{v_g}\right) + \nabla\left(\alpha_g \rho_g \overrightarrow{v_g}\,\overrightarrow{v_g}\right) = -\alpha_g \nabla p + \nabla \overline{\overline{\tau_g}} + \alpha_g \rho_g \vec{g} + M_g \tag{7}$$

$$\overline{\overline{\tau_g}} = \alpha_g \mu_g\left(\nabla \overrightarrow{v_g} + \nabla \overrightarrow{v_g}^T\right) - \alpha_g \frac{2}{3}\mu_g\left(\nabla \overrightarrow{v_g}\right)\overline{\overline{I}} \tag{8}$$

Conservation equation of momentum for the solid phase

$$\frac{\partial}{\partial t}\left(\alpha_s \rho_s \overrightarrow{v_s}\right) + \nabla\left(\alpha_s \rho_s \overrightarrow{v_s}\,\overrightarrow{v_s}\right) = -\alpha_s \nabla p + \nabla p_s + \nabla \overline{\overline{\tau_s}} + \alpha_s \rho_s \vec{g} + M_s \tag{9}$$

$$\overline{\overline{\tau_s}} = \alpha_s \mu_s\left(\nabla \overrightarrow{v_s} + \nabla \overrightarrow{v_s}^T\right) + \alpha_s\left(\lambda_s - \frac{2}{3}\mu_s\right)\nabla \overrightarrow{v_s}\overline{\overline{I}} \tag{10}$$

where p_s and μ_s are solid phase viscosity and pressure, which can be obtained by the kinetic theory of the granular flow, and $\overline{\overline{\tau}}$ is the stress of each phase.

2.3.2 Interphase forces

M_l, M_g and M_s are the momentum exchange terms, which are the interphase interaction forces for each phase including the drag force, lift force, turbulent dispersion force, virtual mass force and etc. Only the drag force and virtual mass force will be considered in the present study since the other two forces are negligible. Regarding the drag force between the liquid and gas phases, the equation is written as the following

$$F_{drag,gl} = K_{gl}\left(\overrightarrow{v_g} - \overrightarrow{v_l}\right) \tag{11}$$

where K_{gl} is the momentum exchange coefficients between the liquid and gas phases, which is calculated by

$$K_{gl} = C_{D,gl}\frac{3}{4}\rho_l \frac{\alpha_g \alpha_l}{d_b}\left|\overrightarrow{v_g} - \overrightarrow{v_l}\right| \tag{12}$$

where d_b is the diameter of bubble or droplet, and $C_{D,gl}$ is the drag coefficient between the gas and liquid phases, and the Schiller-Naumann drag model (Schiller and Naumann 1935) is used to calculate $C_{D,gl}$, which is shown as

$$C_{D,gl} = \begin{cases} 24(1 + 0.15{Re_1}^{0.687})/Re_1 & Re_1 \leq 1000 \\ 0.44 & Re_1 > 1000 \end{cases} \quad (13)$$

$$Re_1 = \frac{\rho_l d_b |\overrightarrow{v_g} - \overrightarrow{v_l}|}{\mu_l} \quad (14)$$

The drag force between the liquid and solid phases can be expressed as

$$F_{drag,ls} = K_{ls}(\overrightarrow{v_s} - \overrightarrow{v_l}) \quad (15)$$

$$K_{ls} = C_{D,ls} \frac{3}{4} \rho_l \frac{\alpha_l \alpha_s}{d_p} |\overrightarrow{v_s} - \overrightarrow{v_l}| \quad (16)$$

where d_p is the diameter of the particles, and the drag model used to calculate the drag force between liquid and solid phases is also based on the Schiller-Naumann model (Schiller and Naumann 1935). The equations are listed as following

$$C_{D,ls} = \begin{cases} 24(1 + 0.15{Re_2}^{0.687})/Re_2 & Re_2 \leq 1000 \\ 0.44 & Re_2 > 1000 \end{cases} \quad (17)$$

$$Re_2 = \frac{\rho_l d_p |\overrightarrow{u_s} - \overrightarrow{u_l}|}{\mu_l} \quad (18)$$

The drag force between the solid and gas phases is shown as

$$F_{drag,gs} = K_{gs}(\overrightarrow{v_g} - \overrightarrow{v_s}) \quad (19)$$

$$K_{gs} = C_{D,gs} \frac{3}{4} \rho_g \frac{\alpha_g \alpha_s}{d_p} |\overrightarrow{v_g} - \overrightarrow{v_s}| \quad (20)$$

$$C_{D,gs} = \begin{cases} 24(1 + 0.15{Re_3}^{0.687})/Re_3 & Re_3 \leq 1000 \\ 0.44 & Re_3 > 1000 \end{cases} \quad (21)$$

$$Re_3 = \frac{\rho_g d_p |\overrightarrow{v_s} - \overrightarrow{v_g}|}{\mu_g} \quad (22)$$

2.3.3 Turbulence model

In present study, the dispersed RNG k-ε turbulence model is used for the liquid phase, since it performs better than the standard and realizable k-ε models and per-phase RNG k-ε

model (Hamidipour et al., 2012). The turbulence for dispersed phases, which are gas and solid phases in present study, is derived from the time and length scales instead of transport equations (ANSYS, 2014). The general form of the k-ε model of the liquid phase is shown as following

$$\frac{\partial}{\partial t}(\alpha_l \rho_l k_l) + \nabla\,(\alpha_l \rho_l k_l \overrightarrow{v_l}) = \nabla\left(\alpha_l \left(\frac{\theta_k \mu + \mu_t}{\sigma_k}\right)\nabla k\right) + \alpha_l G_{k,q} - \alpha_l \rho_l \varepsilon_l + \Pi_k \tag{23}$$

$$\frac{\partial}{\partial t}(\alpha_l \rho_l \varepsilon_l) + \nabla\,(\alpha_l \rho_l \varepsilon_l \overrightarrow{v_l}) = \nabla\left(\alpha_l \left(\frac{\theta_{1,\varepsilon} \mu + \mu_t}{\sigma_\varepsilon}\right)\nabla \varepsilon\right) + \alpha_l \frac{\varepsilon_l}{k_l}(C_{1\varepsilon}\theta_{2,\varepsilon} G_{k,q} - C_{2\varepsilon}\theta_{3,\varepsilon}\rho_l \varepsilon_l) + C_{3,\varepsilon}\alpha_l \rho_l \Pi_k - \alpha_l R_\varepsilon \tag{24}$$

$$\mu_t = \rho C_\mu \frac{k^2}{\varepsilon} \tag{25}$$

where k is the turbulence kinetic energy, ε is the turbulence kinetic energy dissipation, and Π_k is the source term to account for the turbulence interaction between phases which is neglected in the dispersed model, and G_k is the turbulence kinetic energy generated by mean velocity gradient is given as

$$G_k = \mu_t S^2 \tag{26}$$

$$S = \sqrt{2 S_{ij} S_{ij}} \tag{27}$$

$$S = \frac{1}{2}(\nabla \vec{v} + (\nabla \vec{v})^T) \tag{28}$$

The RNG k-ε model is obtained by renormalizing the Naiver-Stokes equations based on renormalization group method (Yakhot & Orszag, 1986). The RNG k-ε model has a better performance on predicting rapid strained flows and swirling flow, and the RNG k-ε model can simulate the flow in a low-Reynolds region accurately by using an analytical formula to calculate the effective viscosity (ANSYS,2014). The parameters of the standard k-ε turbulence model will be modified as following when it is used as a dispersed RNG k-ε turbulence model

θ_k is set to one and σ_k is calculated based on σ_{eff} which is the effective Schmidt number, and it is shown by equation

$$\left|\frac{\left(\frac{1}{\sigma_{eff}}\right)-1.3929}{\left(\frac{1}{\sigma_0}\right)-1.3929}\right|^{0.6312}\left|\frac{\left(\frac{1}{\sigma_{eff}}\right)+2.3929}{\left(\frac{1}{\sigma_0}\right)+2.3929}\right|^{0.3679}=\frac{\mu}{\mu+\mu_t} \quad (29)$$

where $\frac{1}{\sigma_0} \approx 1$ and $\theta_k = 1$

Then $\theta_{1,\varepsilon}$ is also set to one and σ_ε is defined based on σ_{eff} as well which can be also calculated by Eq (29). R_ε is the addiction model parameter calculated by

$$R_\varepsilon = \frac{\rho C_\mu \eta^3 (\frac{1-\eta}{\eta_0})}{1+\beta\eta^3}\frac{\varepsilon^2}{k} \quad (30)$$

where η is the dimensionless strain rate coefficient, which is calculated by

$$\eta = \frac{Sk}{\varepsilon} \quad (31)$$

In that case, the equations for the RNG k-ε turbulence model can be write as following

$$\frac{\partial}{\partial t}(\rho k) + \nabla\,(\rho_l k_l \overrightarrow{v_l}) = \nabla\left(\alpha_k \mu_{eff} \nabla k\right) + G_k + G_b - \rho\varepsilon - Y_M + S_k \quad (32)$$

$$\frac{\partial}{\partial t}(\rho\varepsilon) + \nabla\,(\rho_l \varepsilon_l \overrightarrow{v_l}) = \nabla\left(\alpha_\varepsilon \mu_{eff} \nabla\varepsilon\right) + C_{1\varepsilon}\frac{\varepsilon}{k}(G_k + C_{3\varepsilon}G_b) - \rho C_{2\varepsilon}\frac{\varepsilon^2}{k} - R_\varepsilon + S_\varepsilon \quad (33)$$

The relevant parameters of the dispersed RNG k-ε model is listed in Table 2.2

Table 2.2 Parameters of the RNG k-ε models

Parameters	θ_k	$\theta_{1,\varepsilon}$	σ_ε	σ_k	$C_{1\varepsilon}$	$C_{2\varepsilon}$
Values	1	1	Equation (29)	Equation (29)	1.42	1.68
Parameters	C_μ	R_ε	$\theta_{3,\varepsilon}$	$\theta_{2,\varepsilon}$	$C_{3,\varepsilon}$	Π_k
Values	0.085	Equation (30)	1	1	0	0

A wall function is used with a turbulence model in order to modify the model for the low Reynold number region. The scalable wall function is used in the present study, since the standard wall function is not accurately when y^* is smaller than 15. The scalable wall function refined the standard wall function when $y^* < 11.225$ by using a limited value shown in equation to avoid the deterioration in the accuracy of the near wall region (ANSYS, 2014).

$$\widetilde{y^*} = Max(y^*, y^*_{limit}) \tag{34}$$

where $y^*_{limit} = 11.225$ and y^* is the dimensionless distance from the wall.

To describe the solid phase motion, the KTGP is used to calculate solid stress and pressure, which are needed to solve the governing equation. The granular temperature is introduced in the KTGP, which is related to the particle random motion, and solid phase stress and pressure are the function of the granular temperature. The constitutive equations related to the KTGP are shown as following

Solid pressure (Lun, Savage, Jeffrey, & Chepurniy, 1984)

$$P_S = \alpha_S \rho_S \Theta_S + 2\rho_S(1 + e_{ss})\alpha_s^2 g_{0,ss}\Theta_s \tag{35}$$

where Θ_s is granular temperature

Radial distribution function (Ding & Gidaspow, 1990)

$$g_{0,ss} = \left[1 - \left(\frac{\alpha_s}{\alpha_{s,max}}\right)^{1/3}\right]^{-1} \quad (36)$$

Solid shear stress

$$\mu_s = \mu_{s,col} + \mu_{s,kin} + \mu_{s,fr} \quad (37)$$

Collisional viscosity (Gidaspow, 1994)

$$\mu_{s,col} = \frac{4}{5}\alpha_s \rho_s d_s g_{0,ss}(1 + e_{ss})\sqrt{\frac{\Theta_s}{\pi}} \quad (38)$$

Kinetic viscosity (Syamlal, Rogers, & O`Brien, 1993)

$$\mu_{s,kin} = \frac{\alpha_s \rho_s d_s \sqrt{\Theta_s \pi}}{6(3+e_{ss})}\left[1 + \frac{2}{5}(1 + e_{ss})(3e_{ss} - 1)\alpha_s g_{0,ss}\right] \quad (39)$$

Frictional viscosity (Schaeffer, 1987)

$$\mu_{s,fr} = \frac{P_s \sin\phi}{2\sqrt{I_{2D}}} \quad (40)$$

Bulk viscosity (Lun et al., 1984)

$$\lambda_s = \frac{4}{3}\alpha_s^2 \rho_s d_s g_{0,ss}(1 + e_{ss})\sqrt{\frac{\Theta_s}{\pi}} \quad (41)$$

Granular conductivity (Syamlal et al., 1993)

$$k_{\Theta_s} = \frac{15 d_s \rho_s \alpha_s \sqrt{\Theta_s \pi}}{4(41-33\eta)}\left[1 + \frac{12}{5}\eta^2(4\eta - 3)\alpha_s g_{0,ss} + \frac{16}{15\pi}(41 - 33\eta)\alpha_s g_{0,ss}\eta\right] \quad (42)$$

where

$$\eta = \frac{1}{2}(1 + e_{ss}) \quad (43)$$

Collisional dissipation of energy (Lun et al., 1984)

$$\gamma_{\Theta_s} = \frac{12(1-{e_{ss}}^2 g_{0,ss})}{d_s\sqrt{\pi}}\rho_s \alpha_s^2 \Theta_s^{3/2} \quad (44)$$

2.4 Numerical methodology

In the present study, the simulation of the three-phase flows will be conducted in an inverse TPFB in order to study the hydrodynamics and flow patterns. The inverse TPFB shown in Figure 2.1 will be simplified to a 2D planar computational domain. The mesh is created by using the commercial software ICEM 16.0. The computational domain is 3 m × 0.153 m based on the dimensions of the inverse TPFB used in the experimental study. The schematic diagram of the computational domain and boundary conditions is shown in Figure 2.2.

The gas inlet is located at the bottom of the reactor, and the uniform velocity is used as the inlet boundary condition for the gas phase. For the liquid and solid phases, the inlet velocity is zero. The outflow is used as the outlet boundary condition for the gas phase, which located at the top of the column. The no-slip boundary condition is set for the liquid phase as wall boundary condition, and free-slip is used for both the gas and solid phases, so the specularity coefficient of the solid phase is set to zero which is correspond to the free-slip wall boundary condition. The particle-particle restitution coefficient is set as 0.95.

The initial conditions of the inverse TPFB under the batch liquid operating condition are also shown in Figure 2.2, which are different from the conventional or circulating fluidized beds. To mimic the experimental condition, the liquid phase is initially patched inside the reactor, and particles are patched at the top surface of the liquid phase because the density of the particles is lower than the density of the liquid. The patched height of each phase depends on the solids loading.

The simulation is carried out by using the commercial software Fluent 16.0. The double precision segregated, transient, implicit formulation are used. The phase coupled SIMPLE algorithm is used for the pressure-velocity coupling. The second order upwind scheme is used to discretize the momentum equation while the first order upwind discretization method is used for all other convection terms, since the momentum equation is more important. The convergence criterion is set as 5×10^{-4} and the time step is set as 0.0001.

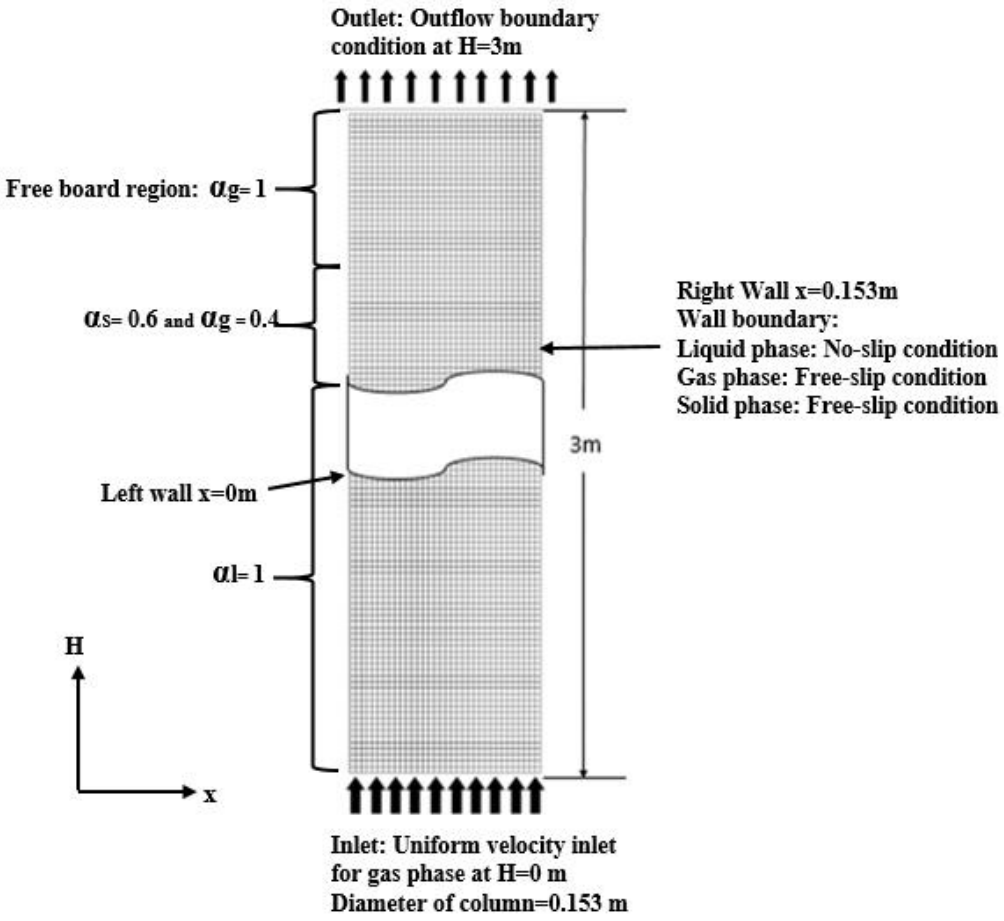

Figure 2.2 Computational domain of the inverse three-phase fluidized bed

2.5 Results and discussion

2.5.1 Grid independence test and CFD model validation

The grid independent study will be performed in this section under U_g=20 mm/s. The information on three different meshes is listed in Table 2.3, and the average gas holdup will be used to check the grid independence. The results from three meshes are listed in Table 2.4. It can be seen that the difference of average gas holdup between the medium mesh and fine mesh is less than 1%. Therefore, the medium size mesh is selected in this study for the further simulations.

Table 2.3 Mesh information for the grid independent test

Mesh info	Size	Coarse	Medium	Fine
	Face	44815	73906	286680
	Node	22750	37400	144000
	Cell	22066	36507	142681

Table 2.4 Average gas holdups for different meshes

Mesh	Average gas holdup	Difference% of gas holdup
Coarse mesh	0.0856	
Medium mesh	0.0819	4.5%
Fine mesh	0.0816	0.4%

The proposed CFD model will be validated by comparing the numerical results with the experimental data. The operating condition under U_g =15 mm/s, particle density 930 kg/m^3 and particles loading 15% is used for model validation. Figure 2.3 shows the comparison of the solids volume fraction in the axial direction between the CFD results and the experimental data. The average solids volume fraction from the experimental data is around 14.2% and the distribution is almost uniform along the axial direction of the column. The CFD results also show the near uniform distribution of the solids volume fraction in the axial direction and the solids volume fraction is around 13.8%. Thus, the agreement between the numerical results and experiment data is good as shown in Figure 2.3.

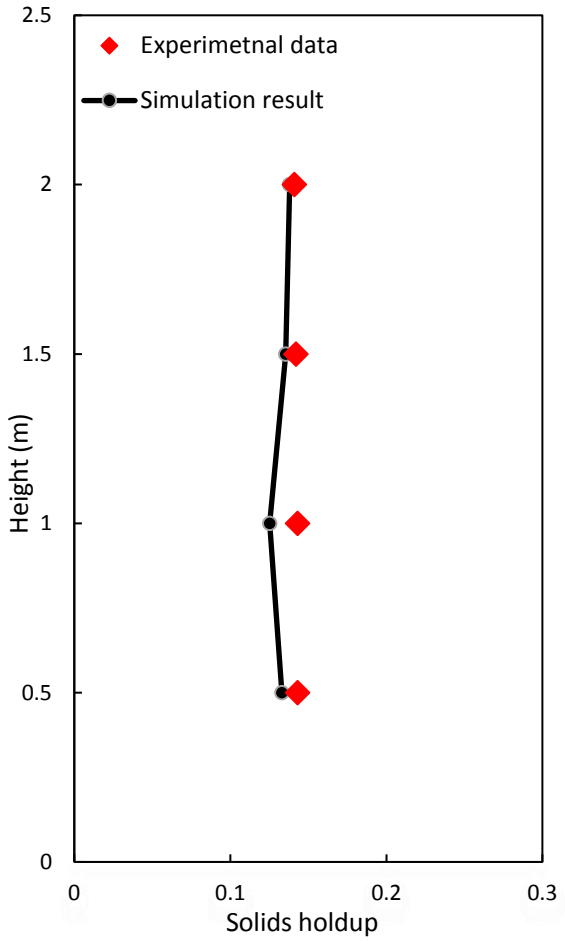

Figure 2.3 Comparison of the axial profiles of the solids volume fraction between the numerical results and experimental data at U_g=15 mm/s, 15% loading and ρ_s=930 kg/m^3

2.5.2 Flow development and flow structure in an inverse three-phase fluidized bed

The flow development in an inverse gas-liquid-solid TPFB will be studied numerically. Under U_g=15 mm/s, particles are uniformly distributed along the axial direction in the column. Therefore, the fluidization process in the inverse TPFB is investigated under U_g=15 mm/s. The flow development process in an inverse TPFB can be divided into three stages, the initial fluidization stage, developing stage and fully developed stage.

2.5.2.1 Initial fluidization stage

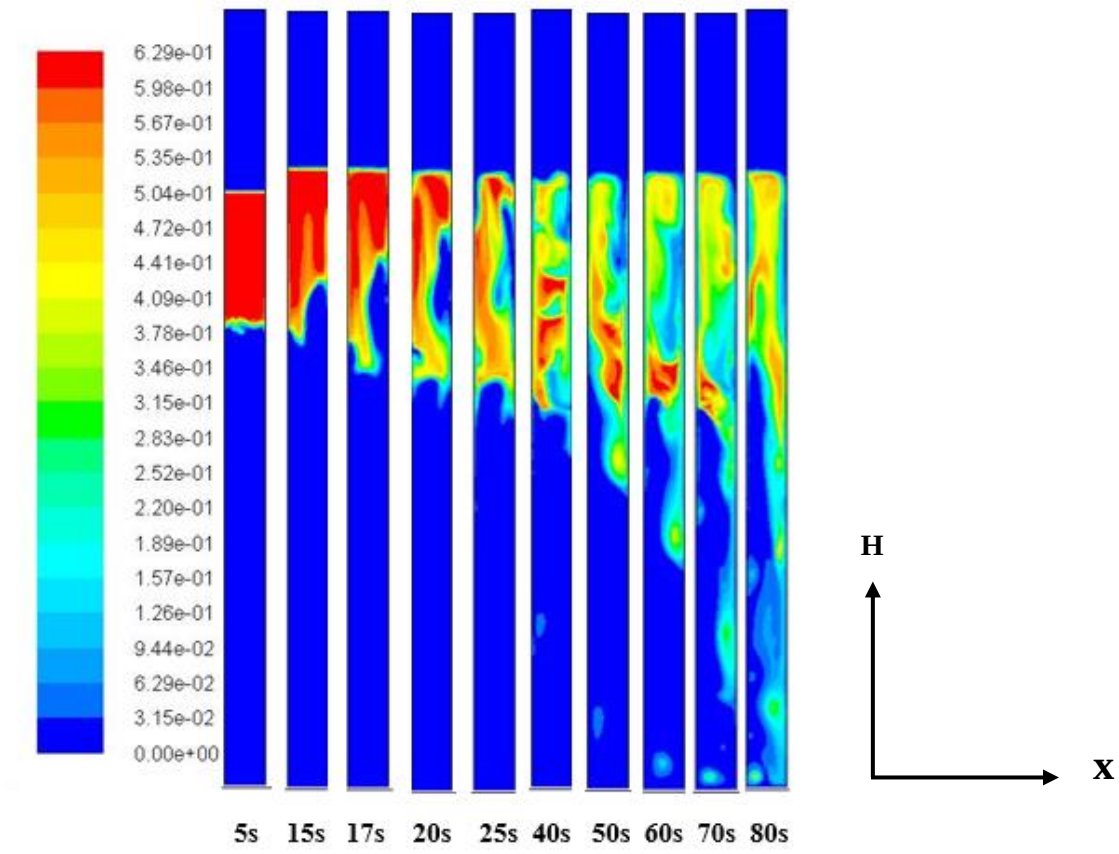

Figure 2.4 Contours of the solids volume fraction at different time of the initial fluidization stage for Ug=15mm/s, 15% solids loading and ρ_s= 930 kg/m^3

The initial fluidization stage is the period in which particles are initially fluidized to when particles first reach the bottom of the reactor. Figure 2.4 displays the contours of the solids volume fraction at different time at the initial fluidization stage, which is from t=5s to 80s. At t=5s, with less air introduced into the column, the particles at the bottom of the packed bed region start to move downward, and most of particles remain packed. As time passes by, more air is introduced into the column and flows through the packed particles, so the drag force acting on particles can balance with the buoyancy force and gravity, causing packed particles to expand from the bottom of the packed bed region. At 80s, some particles reach to the bottom of the column. Figure 2.5 shows the axial profile of the solids volume fraction at t=15s, t=60s and t=80s. At t=15s, most particles remain packed, and the solids

volume fraction is around 0.6 at the upper part of the column. It can be seen that more particles move downward with time, so the solids volume fraction at the upper part of the column gradually decreases, and particles at the lower part of the column become denser with the time at the initial fluidization stage.

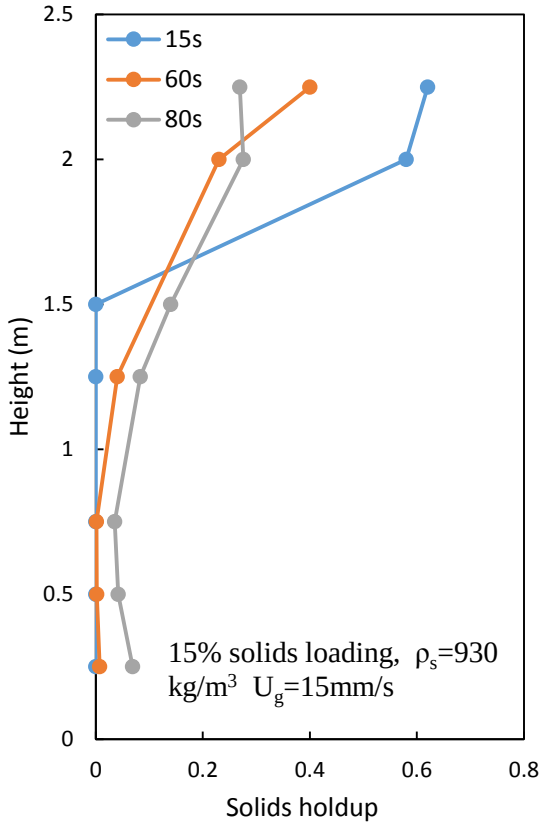

Figure 2.5 Axial profiles of the solids volume fraction at different time at the initial fluidization stage

Figure 2.6 shows the radial profile of the solids volume fraction at the initial fluidization stage at different axial locations in the column. The x-axis is the radial positon of the column which is from the left wall (x=0 m) to the right wall (x=0.153 m), and the center of the column is at x=0.0765 m. At H=0.5 m, the solids volume fraction is zero because no particles have moved to this location yet. At H=1 m, there are only small number of particles (very low solids volume fraction) at the near wall region. At H=2 m, the radial profile of the solids volume fraction is non-uniform, and the solids volume fraction at the

near wall region is low. In contrast, the solids volume fraction at the near wall region is high at H=1.5 m. So it can be concluded that particles moved downward at the near wall region first. The same phenomena were also observed by Renganathan and Krishnaiah (2008). The liquid recirculation caused by the upward flow of gas bubbles can fluidize the particles at the bottom part of packed bed from the near wall region first, and the particle recirculation was created from the wall to center region. Figure 2.7 shows the radial profile of the gas holdup at different axial locations at the initial fluidization stage. The non-uniform distribution of the air in radial direction, which is dense at the center region and dilute at the near wall region, can be observed at all axial locations. In addition, the gas holdup is around 0.045 at H= 2 m, which is lower than the gas holdup at other axial locations as the most of particles remained at the upper part of column and the system is still at the initial fluidization stage.

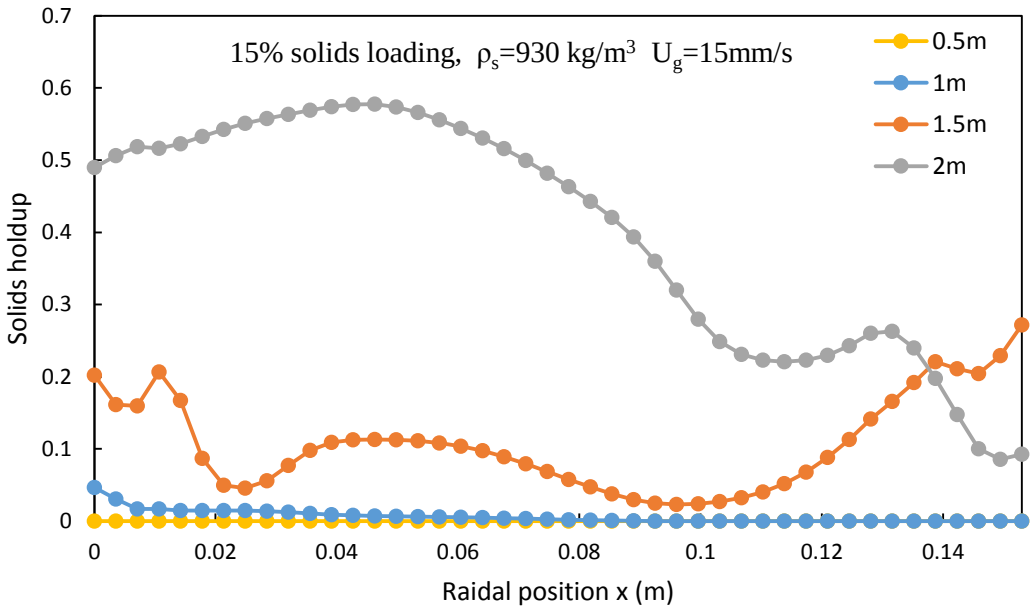

Figure 2.6 Radial profiles of the solids volume fraction at different axial locations at the initial fluidization stage (t=30s).

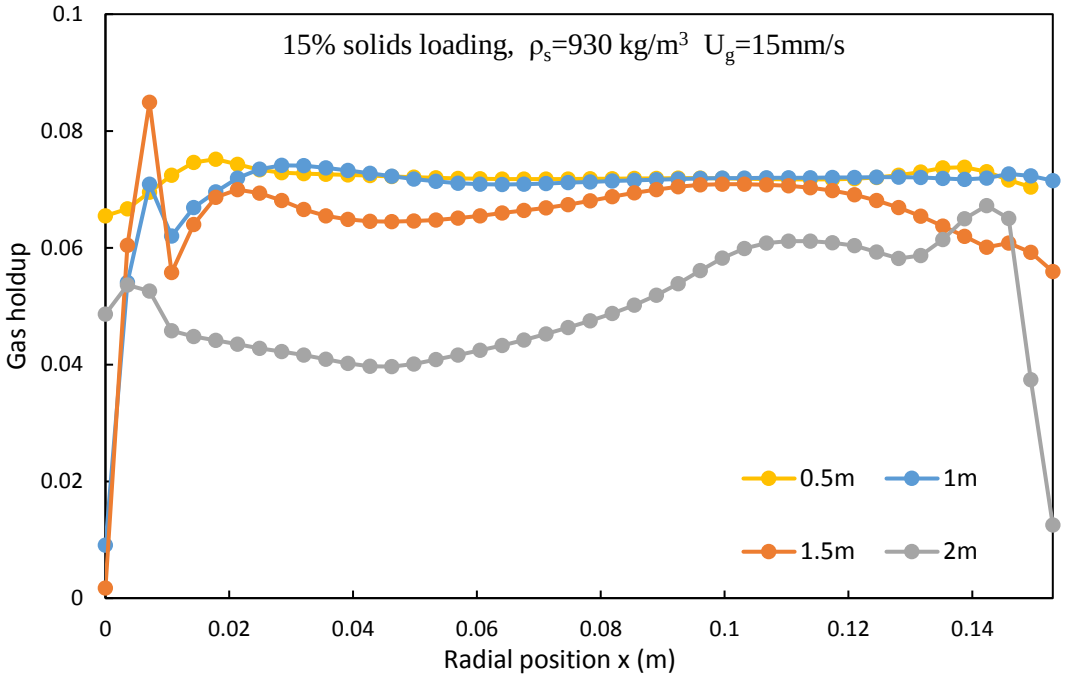

Figure 2.7 Radial profiles of the gas volume fraction at different axial locations at the initial fluidization stage (t=30s)

Figure 2.8 shows the radial profiles of the solids axial velocity at different axial locations at the initial fluidization stage. The positive solids axial velocity indicates that particles flow upward, and the negative solids axial velocity represents that particles flow downward to the bottom of the column. At H=0.5 m, the solids axial velocity is zero because particles have not reached to this location yet. At other axial locations, non-uniform radial profiles of solids axial velocity can be observed, where the center region has a lower velocity than the velocity at the near wall region. Figure 2.9 is the liquid and gas phases radial profiles of axial velocities at H=0.5 m at the initial fluidization stage. It has been noted from Figure 2.8 that particles have not reached to the lower section of the reactor at t=30s, so there are only the gas and liquid phases existed at H=0.5 m. The liquid and gas phases have the similar velocity profiles, which are higher in the center region and lower in the near wall region. But the gas velocity is around 0.2 m/s, which is much higher than the liquid velocity. The liquid velocity profile also shows that the liquid moves downward at the near wall region and moves upward at the center region, which indicates the recirculatory flow pattern of the liquid phase. Thus, it can be concluded that the liquid velocity, which is

caused by the gas flow only, is very small, and the upward gas flow can induce the liquid recirculation. This is further verified the point mentioned previously that particles are fluidized first at the near wall region due to the liquid recirculation induced by upward flow of gas bubbles.

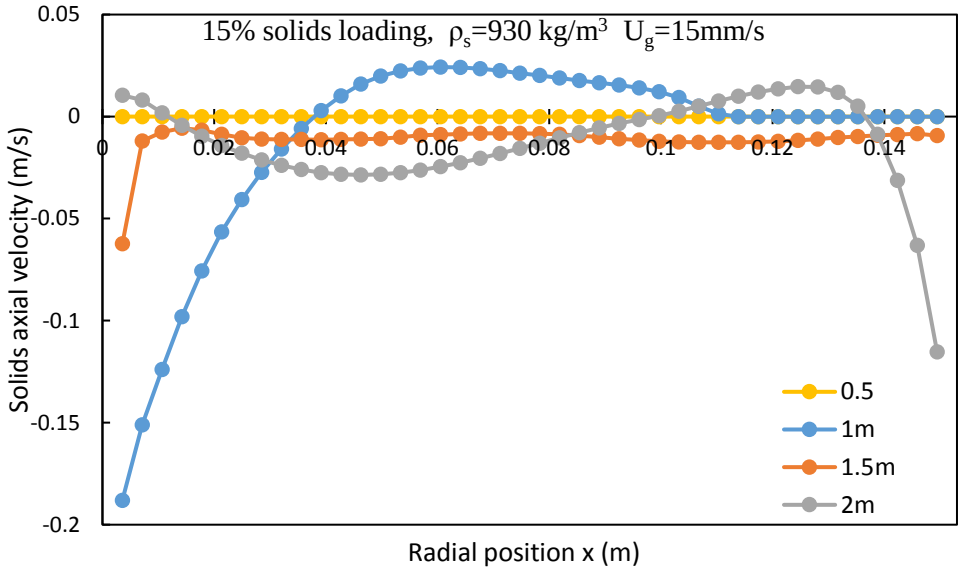

Figure 2.8 Radial profiles of the solids axial velocity at different axial locations at the initial fluidization stage (t=30s)

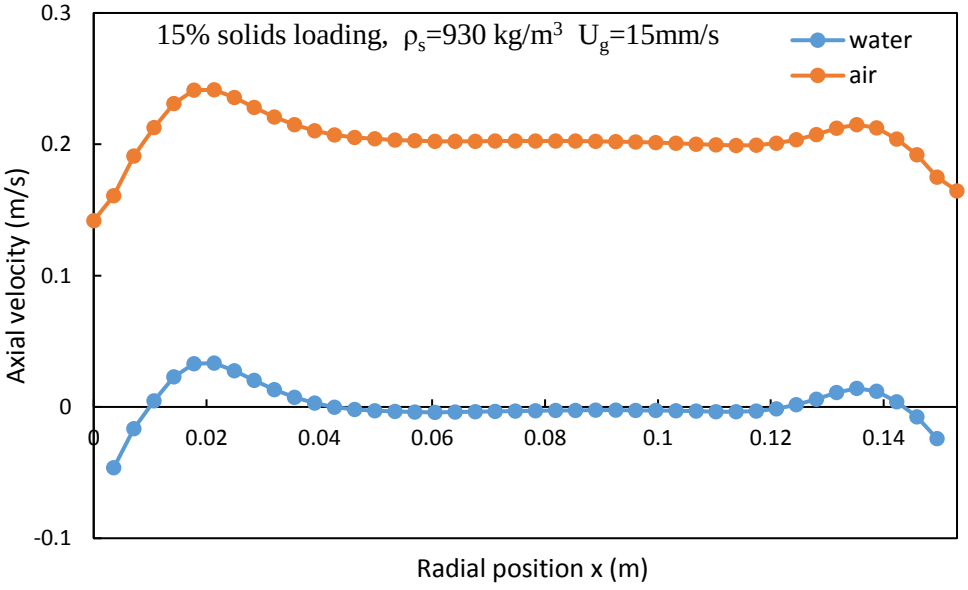

Figure 2.9 Radial profiles of the liquid and gas axial velocities at H=0.5 m (t=30s)

2.5.2.2 Developing stage

The developing stage is defined as the period from which particles first reached to the bottom of the column to particles uniformly distributed along the axial direction of the column. The contours of the solids volume fraction at the developing stage are shown in Figure 2.10. The figure shows the movement of particles from t=110s to 190s. More particles moved toward the bottom of the column with time during this period, which leads to a gradual decrease in the solids volume fraction at the upper part of the column and a gradual increase in the solids volume fraction at the lower part of the column. Figure 2.11 shows the axial profiles of the solids volume fraction at t=100s, 130s and 150s. A non-uniform axial profile of the solids volume fraction, which is higher at the upper section of the column and lower at the lower section of the column, can be observed. However, the solids distribution become more and more uniform with time during this period. Therefore, the axial profile of solids distribution at the developing stages is more uniform than that at the initial fluidization stage.

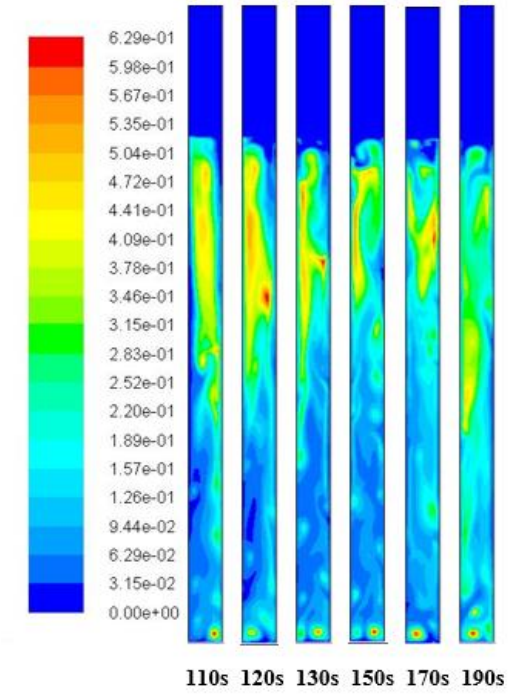

Figure 2.10 Contours of the solids volume fraction at different time at the developing stage

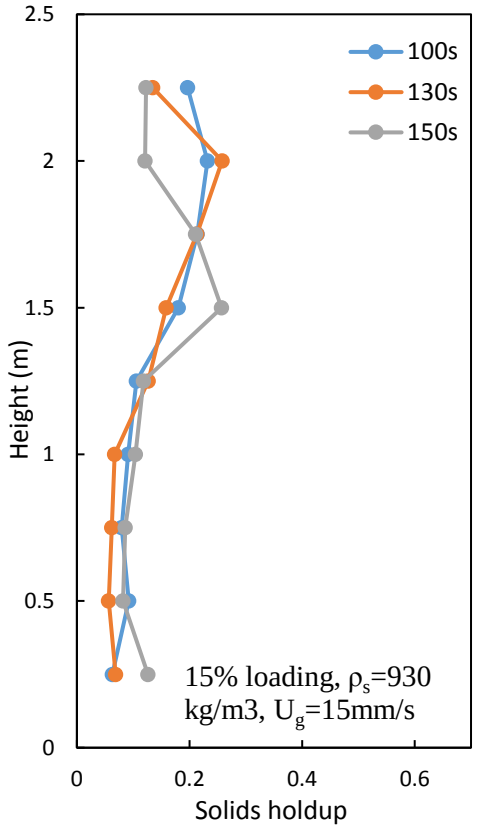

Figure 2.11 Axial profiles of the solids volume fraction at different time at the developing stage (t=150s)

The radial profiles of the gas holdup at different axial locations at the developing stage are presented in Figure 2.12. The non-uniform radial profile of the gas holdup, which is higher at the center region and lower at the near wall region, is observed at all axial locations, due to the wall effect. In addition, unlike the radial gas holdup profile at the initial fluidization stage shown in Figure 2.7 where the radial gas holdup at H=2 m is smaller than the gas holdup at other axial locations, the radial gas holdup at all axial locations are almost identical at the developing stage. Figure 2.13 shows the radial profiles of the solids holdup at different axial locations at the developing stage. The solids volume fraction at different axial locations are similar and non-uniform along the radial direction, which is dense at the center region and dilute at the near wall region. However, the solids holdup is higher at the upper section of the column than that at the lower section of the column because more particles are distributed from the upper section of the column during the developing stage.

In addition, the radial distribution of the solids volume fraction becomes more uniform in the axial flow direction, (i.e. it is less uniform at the upper region and more uniform at the lower region of the column).

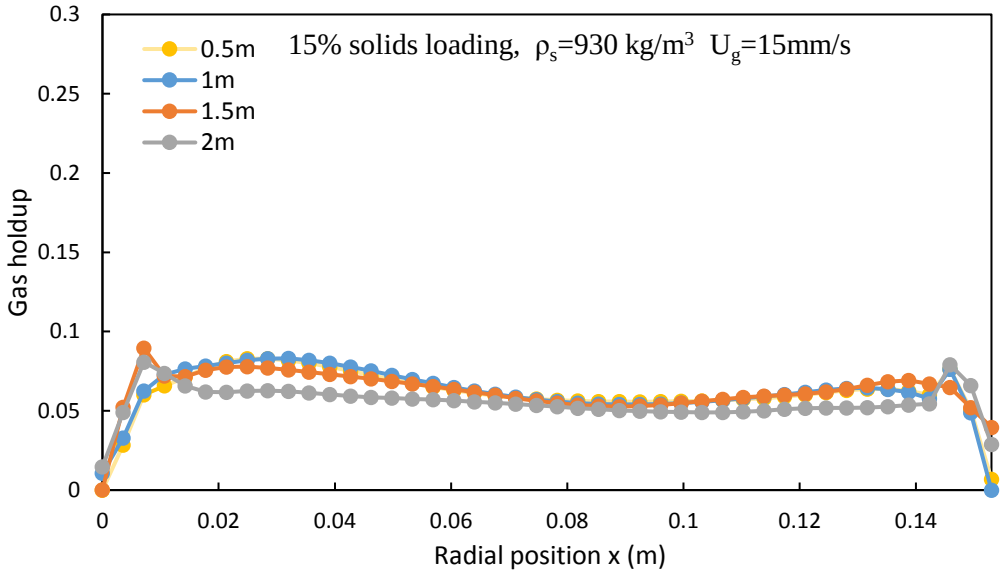

Figure 2.12 Radial profiles of the gas volume fraction at different axial locations at the developing stage (t=150s)

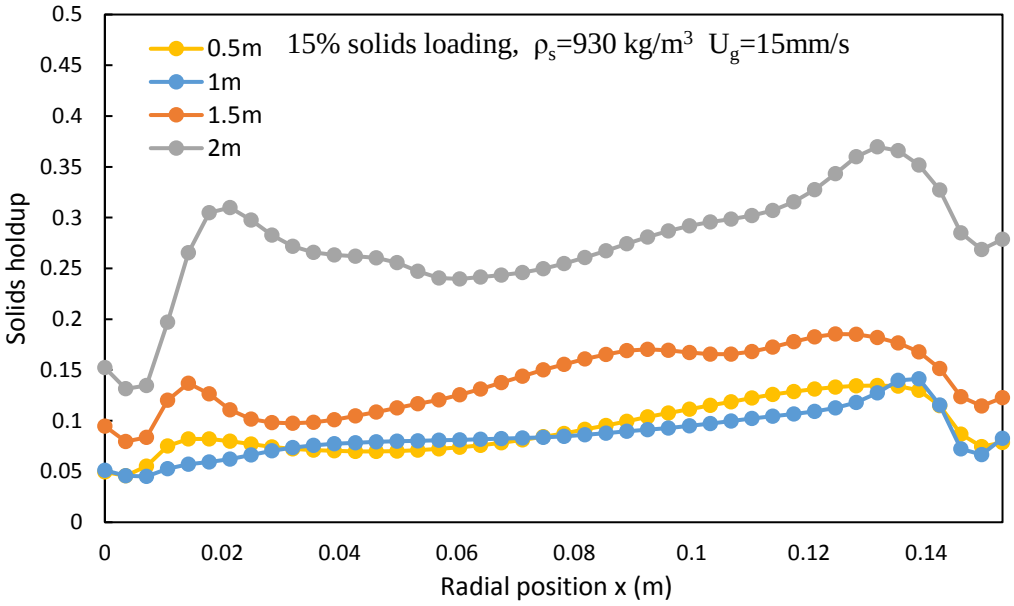

Figure 2.13 Radial profiles of the solids volume fraction at different axial locations at the developing stage (t=150s)

The radial profiles of the solids axial velocity at different axial locations are shown in Figure 2.14. It can be seen that the solids axial velocity component is mainly positive on the left-hand side of the column and mainly negative on the right-hand side, and is zero near the center, indicating that there is a recirculation in the solid flow.

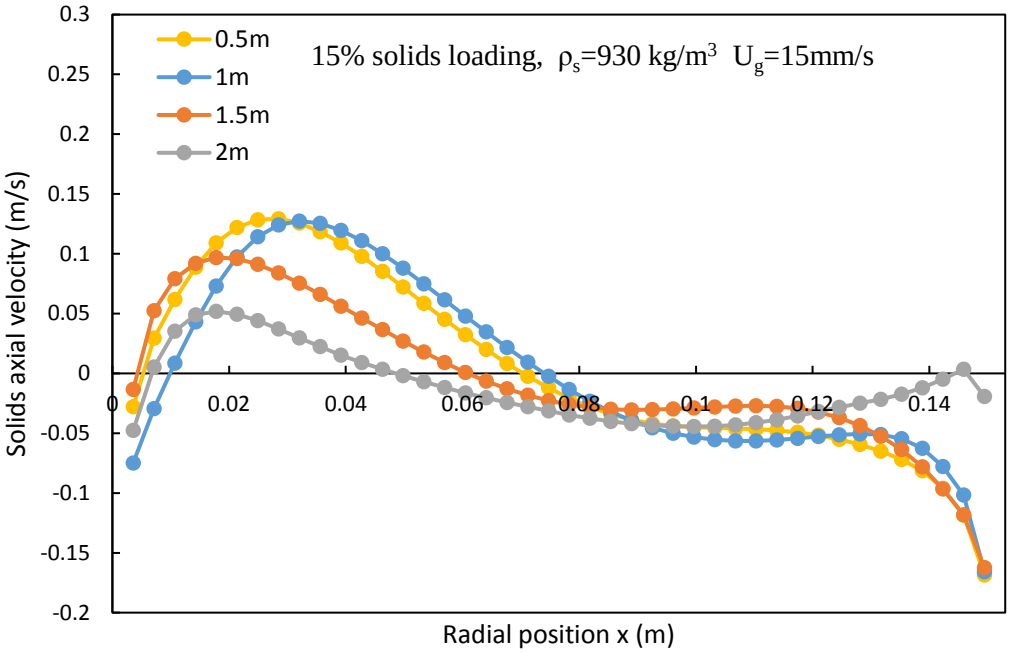

Figure 2.14 Radial profiles of the solids axial velocity component at different axial locations at the developing stage (t=150s)

2.5.2.3 Fully developed stage

After the developing stage, the solids distribution in the axial direction will be uniform. Therefore, once particles are uniformly distributed along the reactor, the fully developed stage is achieved. Figure 2.15 shows the contours of the solid phase volume fraction from 200s -290s, which reveals the particle movement at the fully developed stage. It is noted that the solids volume fraction is almost uniform along the column. Thus, one of the characteristic of the fully developed stage is that the axial distribution of solids volume fraction remains uniform with time. Figure 2.16 is the axial profile of solids holdup, which is uniformly distributed along the column. Figure 2.17 is the time-averaged axial profile of the gas holdup, which is also almost uniformly distributed along the axial direction in the

column. Therefore, both the gas phase and solid phase are distributed uniformly in the axial direction at the fully developed stage at the U_g=15 mm/s.

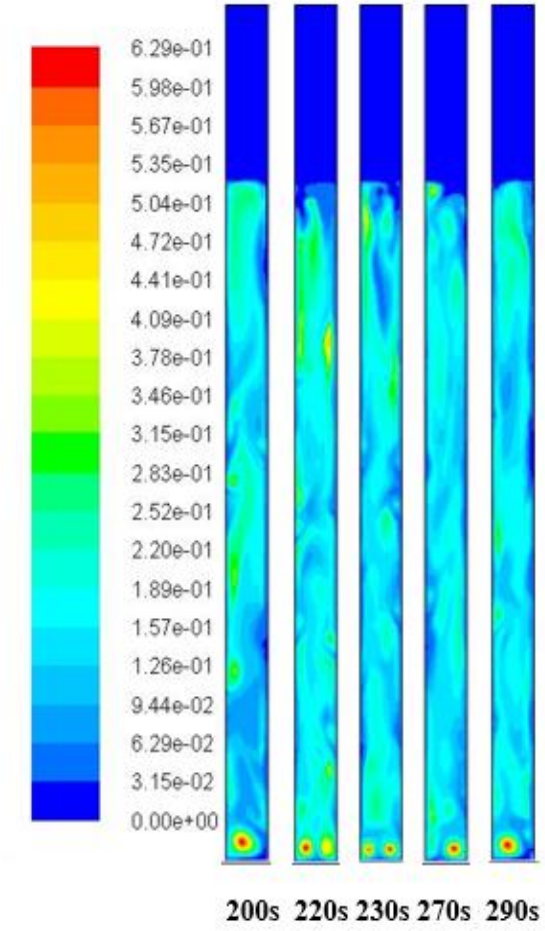

Figure 2.15 Contours of the solid phase volume fraction at the fully developed stage with time

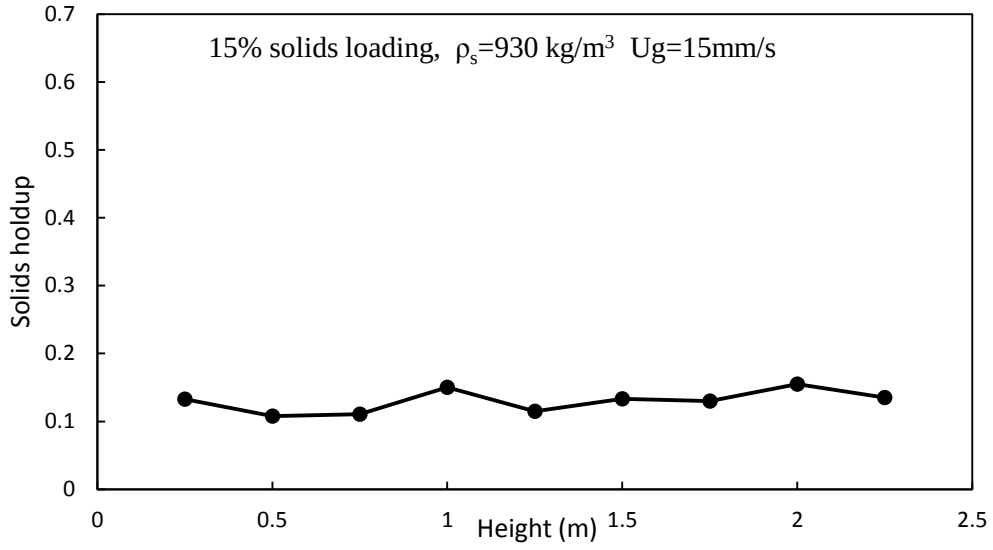

Figure 2.16 Time-averaged axial profile of the solids volume fraction at the fully developed stage

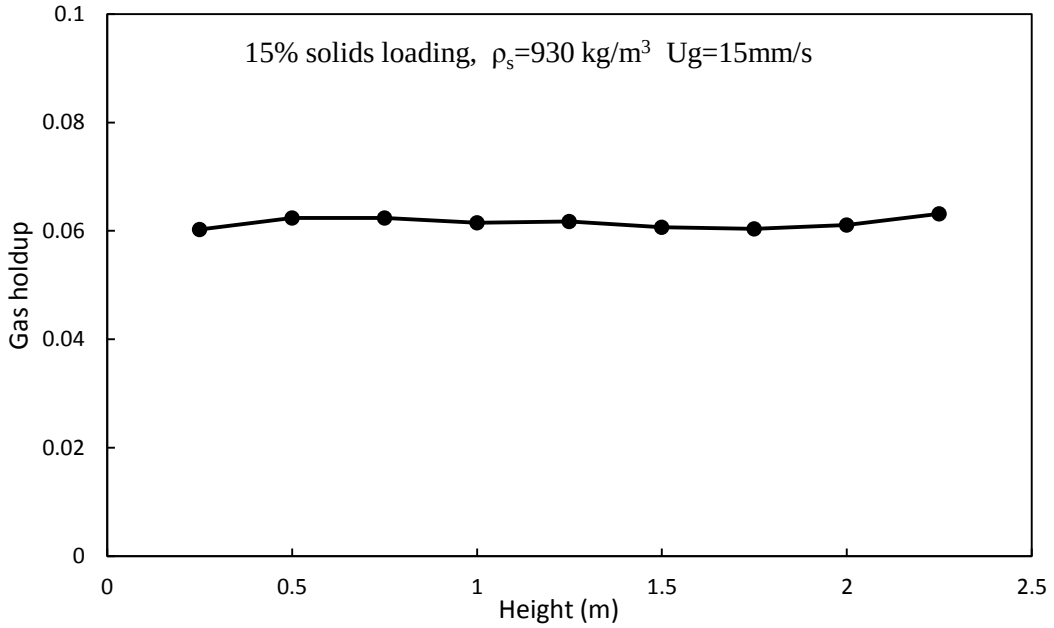

Figure 2.17 Time-averaged axial profile of the gas volume fraction at the fully developed stage

Figure 2.18 shows the time-averaged radial profiles of the solids axial velocity at different axial locations at the fully developed stage. The radial non-uniform distribution of the solids axial velocity can be seen, which is of a 'M' shape with negative solids axial velocities near the wall and in the center region, and positive solids axial velocities in the regions between the wall and center of the column. Therefore, from Figure 2.18, due to the recirculation of the solids, the particles move downward at the wall and in the center of the column, however, the particles move upward near the wall region (x=0.01m-0.045m, and x=0.1m-0.145m). The time averaged radial profiles of the solids holdup at different axial locations are presented in Figure 2.19. The radial non-uniform distributions of the solids holdup can be found at each axial locations, which is dense at the center and dilute at the near wall region. Comparing the radial profiles of the solids axial velocity (Figure 2.18) with the solids holdup (Figure 2.19), it can be seen that the concentration of the solid phase is lower with a higher downward particle velocity at the wall. By contrast, the concentration of the solids phase is higher with a higher upward solids velocity in the center of the column. Those radial non-uniform velocity and holdup profiles are different from the profile in the liquid-solid circulating fluidized bed, in which a high solids velocity leads a low solid volume fraction. By comparing with the initial fluidization stage and the developing stage, the radial non-uniformity profiles of the solids axial velocity and solids holdup profile at the fully developed stage is lower.

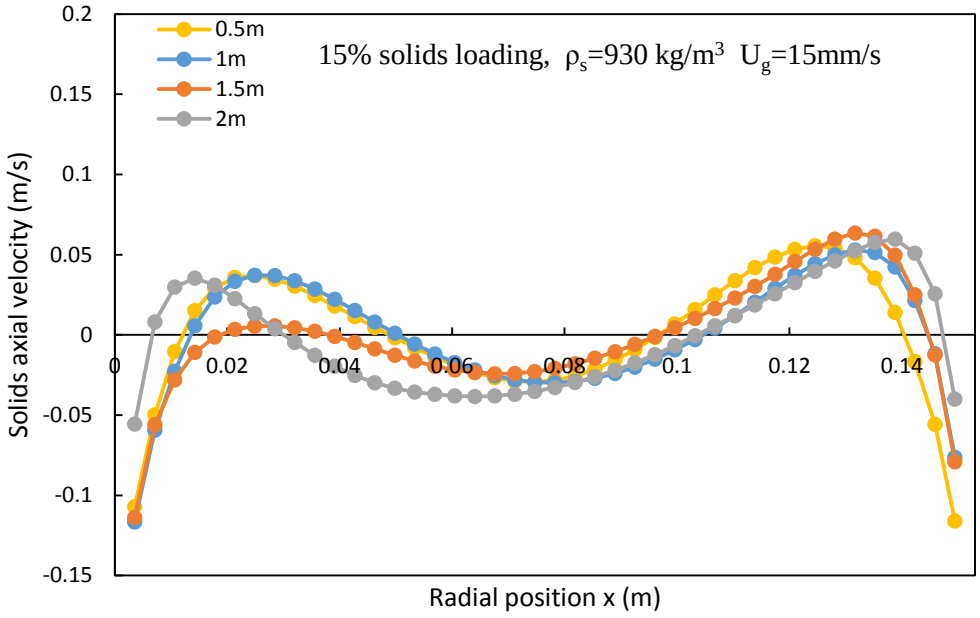

Figure 2.18 Time-averaged radial profiles of the solids axial velocity at different axial locations

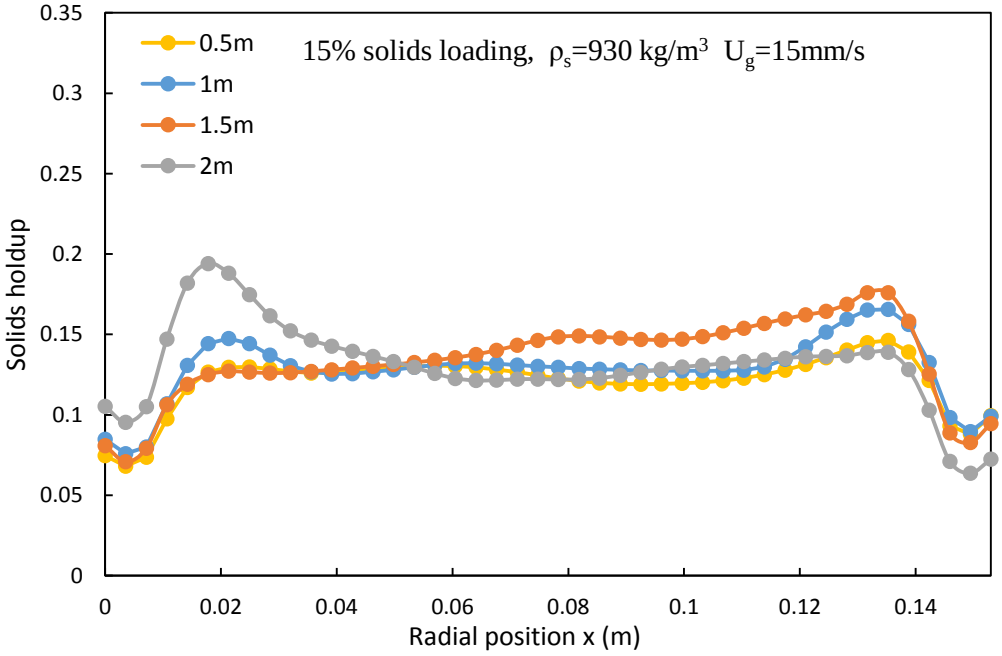

Figure 2.19 Time-averaged radial profiles of the solids volume fraction at different axial locations

The comparison between the liquid axial velocity and solids axial velocity in the radial direction at H=1m is shown in Figure 2.20. It can be seen that the velocities of the liquid phase and solid phase are almost identical. Therefore, particles move along with the liquid at the fully developed stage.

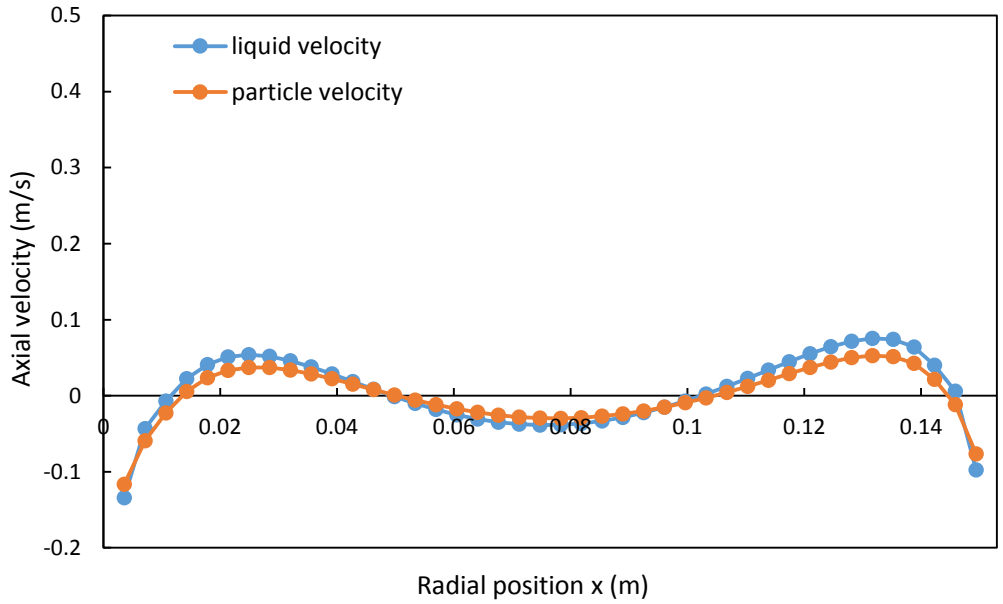

Figure 2.20 Time-averaged radial profiles of the solid and liquid axial velocities at H=1m

2.5.3 Effects of the solids loading

The investigation on the effect of the solids loading on the flow development and hydrodynamics in an inverse TPFB is carried out under U_g =15 mm/s and ρ_s=930 kg/m^3. Figure 2.21 shows the time required to reach the developing stage and fully developed stage under different solids loadings. It is found that 20% solids loading needs the longest time to reach both stages and 5% needs the shortest time. Therefore, the time to reach the developing stage and fully developed stage is longer at a higher solids loading. The possible reason lies in that with higher inventory of particles, it will take longer time to fluidize all particles. In addition, a high solids loading also hindered the liquid flow, which results in a higher fraction loss.

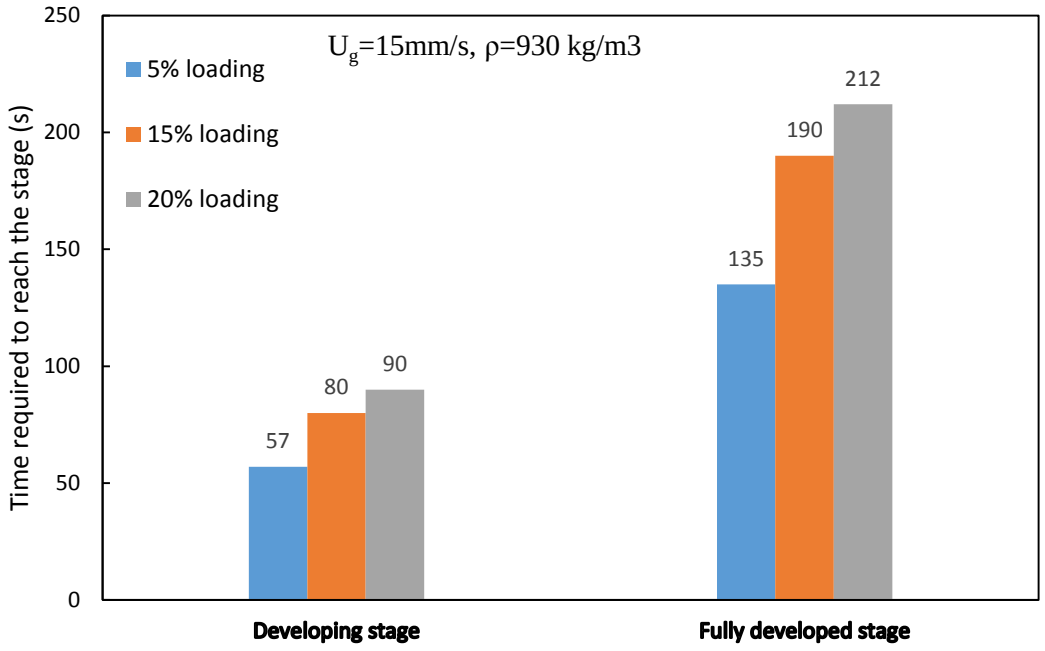

Figure 2.21 Effects of the solids loading on the flow development time

The axial profiles of the solids holdup under different solids loadings are shown in Figure 2.22. It can be seen that the solids holdup under 5% solids loading is lower at the bottom section of the column. However, the lowest solids volume fraction with 20% solids loading is at the top of the column. The most likely reason is that with the increase in the solids loading, the liquid holdup will decrease and the gas holdup, which strongly depends on the inlet superficial gas velocity, remains constant since the inlet superficial gas velocity does not change. Therefore, the average density of the liquid-gas mixture will decrease, which leads to less buoyancy force acting on particles, so more particles will move toward to the bottom of the column. By contrast, with less solids loading, the average density of the liquid-gas mixture will increase, resulting in a higher buoyancy force on the particles. Thus, the solids volume fraction at the lower section of the column is low.

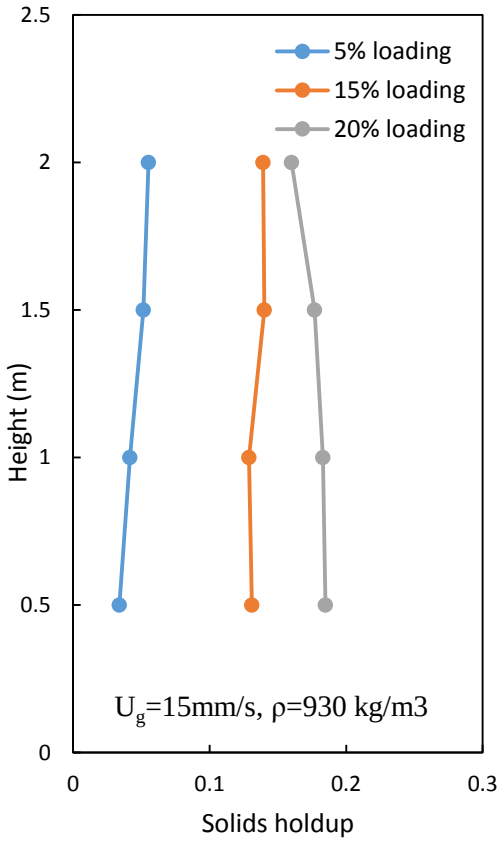

Figure 2.22 Axial profiles of the solids volume fraction under different solids loadings at U_g=15mm/s and ρ_s=930kg/m^3

The time-averaged radial profiles of the solids axial velocity under different solids loadings at the fully developed stage are illustrated at H=1.5 m and 0.5 m in Figure 2.23. A non-uniform distribution of the solids velocity can be seen at both axial locations. The maximum downward velocity is at 5% solids loading in both axial locations, and 20% solids loading has a maximum upward velocity at H=1.5 m. The axial velocities are close to zero in the center region of the column under all solids loadings at both axial locations. The figure also shows the solids loading has almost no influence on the radial profiles of the solids axial velocity at H=0.5 m. Figure 2.24 shows the time-averaged radial profiles of the solids holdup under different solids loadings. It can be seen that the 20% solids loading has the highest solids holdup, and the 5% solids loading has the lowest solids holdup at both H=0.5 m and H=1.5 m. Thus, the local solids holdup increases with the increase in the solids loading. Moreover, the radial non-uniform solids holdup distribution

is observed. In addition, when increasing the solids loading, the radial non-uniformity of the solids holdup also increases.

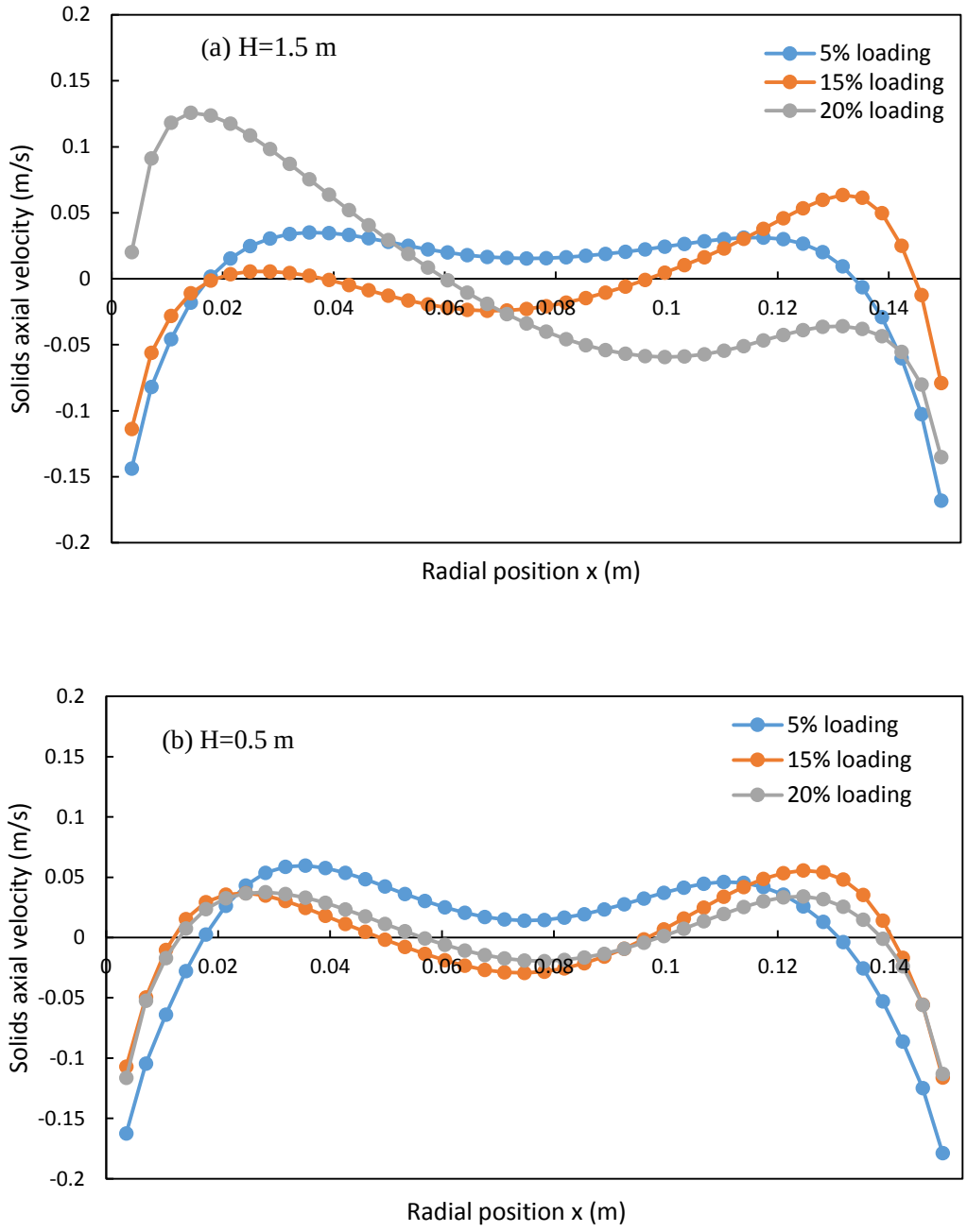

Figure 2.23 Radial profiles of the solids axial velocity under different solids loadings at U_g=15mm/s and ρ_s=930kg/m^3

(a) H=1.5m and (b) H=0.5m

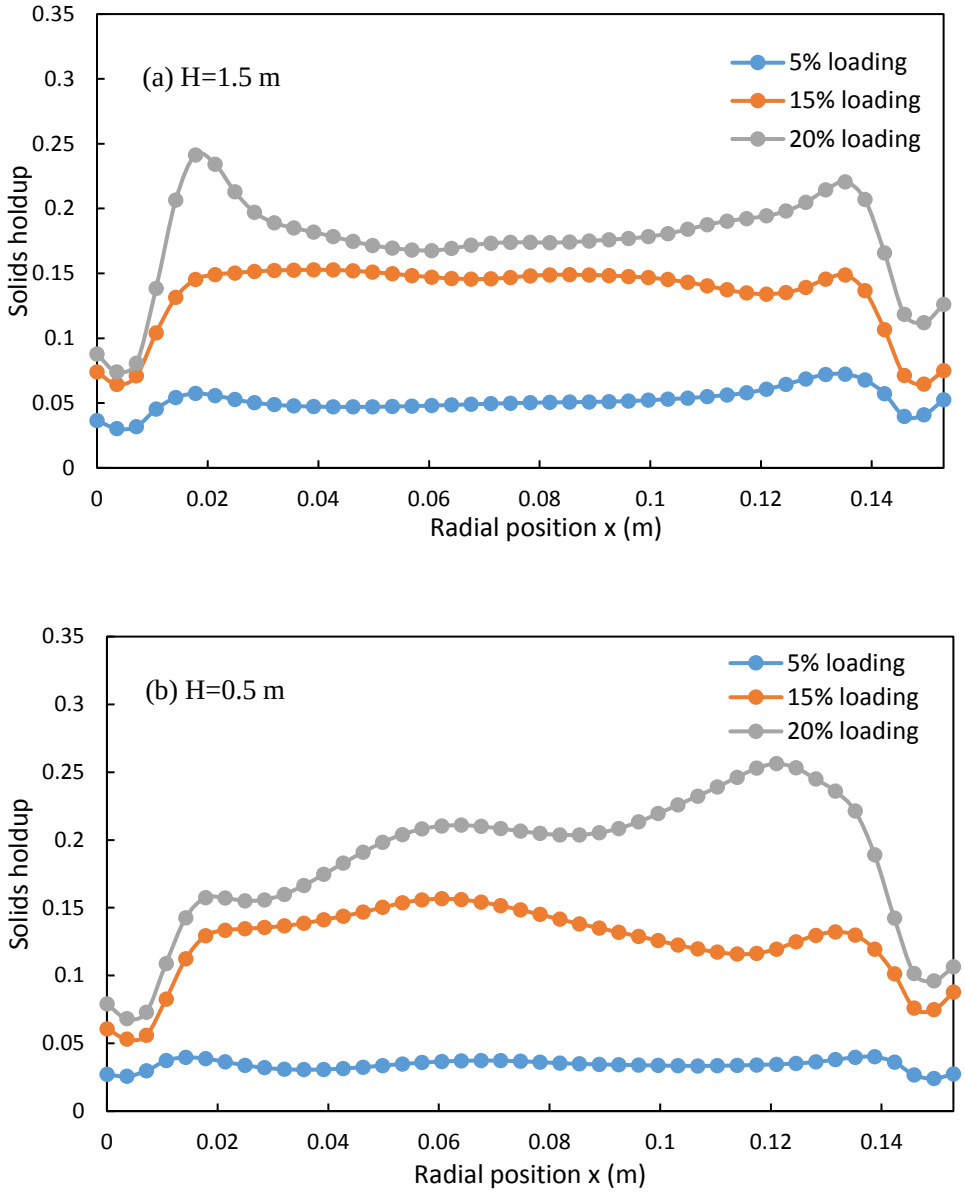

Figure 2.24 Radial profiles of the solids volume fraction under different solids loadings at Ug=15mm/s and ρ_s=930kg/m^3

(a) H=1.5m and (b) H=0.5m

Figure 2.25 shows the radial profiles of the gas holdup under different solids loadings at H=0.5 m and H=1.5 m. The radial non-uniform distribution of the gas holdup can also be seen at all solids loadings, which is dense at the center and dilute at the near wall region.

However, the solids loading has no significant effect on the radial distribution of the gas holdup at both axial locations. The reason may be that the gas holdup depends on the amount of gas introduced to the column, which is strongly related to the inlet superficial gas velocity U_g. Since U_g affects the gas holdup in an inverse TPFB under the batch liquid mode, the effect of the inlet superficial gas velocity on the flow development will be discussed further in the following section.

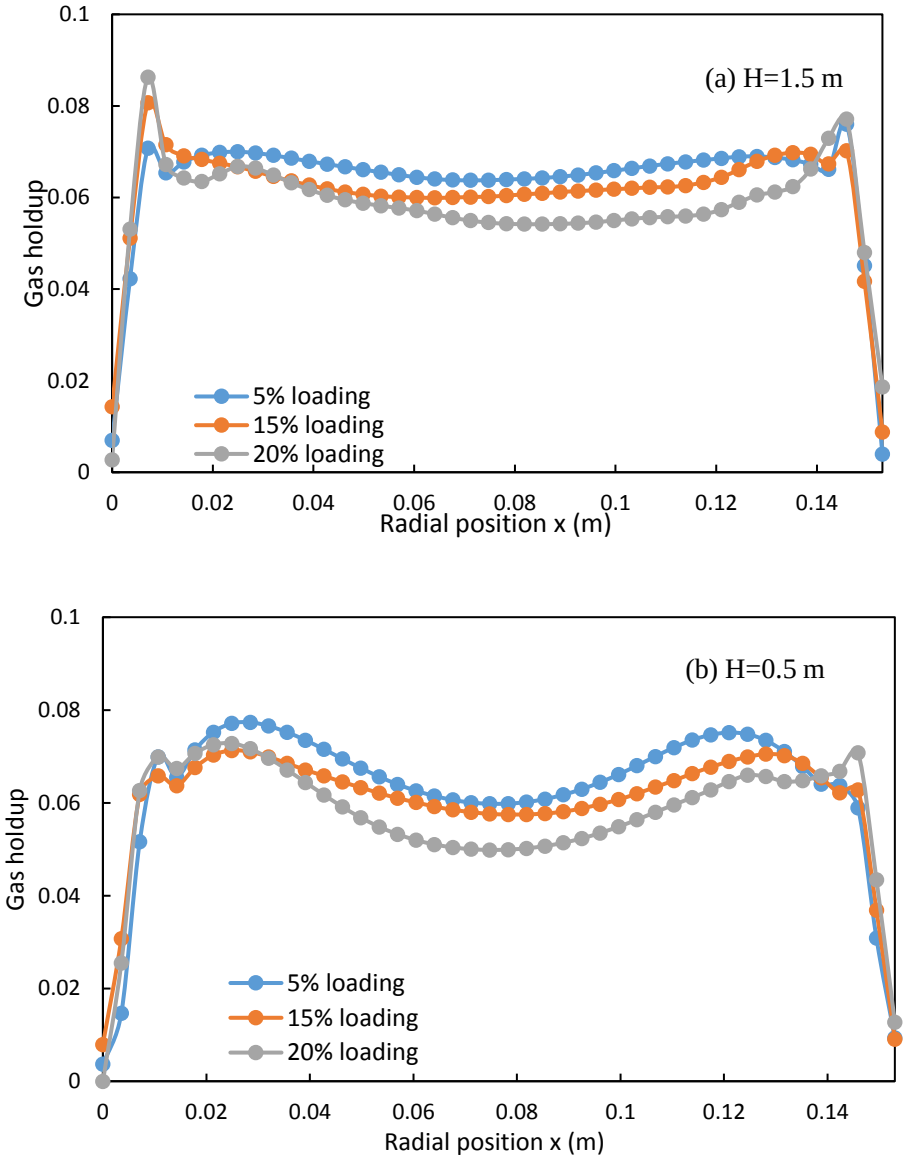

Figure 2.25 Radial profiles of the gas hold up at U_g=15mm/s and ρ_s=930kg/m^3

(a) H=1.5m and (b) H=0.5m

15% solids loading is selected to investigate the effect of the inlet superficial gas velocity on the required time to reach the developing stage and fully developed stage. Figure 2.26 shows the time needed to reach the developing stage and the fully developed stage under different inlet superficial gas velocities. The shortest time to reach the developing stage and the fully developed stage are 27s and 45s, respectively, under U_g=40 mm/s, and the longest time are 80s and 190s, respectively, under U_g=15 mm/s. Therefore, when increasing the inlet superficial gas velocity, less time is needed to reach the developing stage and the fully developed stage, which means packed particles are easier to be fluidized under a higher inlet superficial velocity in the inverse TPFB under the batch liquid mode.

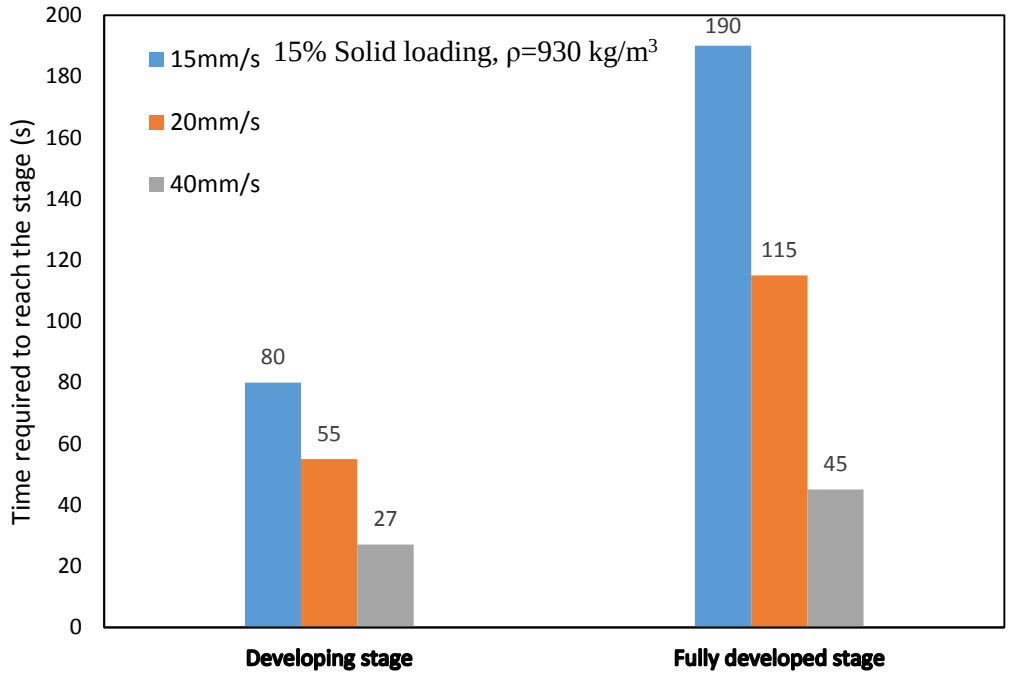

Figure 2.26 Time required to reach to the developing and fully developed stages under differet inlet superficial gas velocities

2.5.4 General flow structure

The knowledge on the hydrodynamics and flow structures is essential for the design and scale up of an inverse three-phase fluidized bed. However, the understanding of the flow structure in an inverse TPFB is still limited due to inadequate experimental data. Therefore,

the general flow structures including the radial solid distribution, axial solid distribution and gas holdup in an inverse TPFB under the batch liquid mode are investigated at the fully developed stage through CFD modelling. Simulations are carried out under different operating conditions and particle properties at 15% solids loading condition.

The particles movements from 30s-200s under different inlet superficial gas velocities from U_g= 9 - 40 mm/s are presented in Figure 2.27 by using contours of the solids volume fraction. At U_g=9 mm/s, particles remain packed as shown in Figure 2.27 (a) because the sum of gravity and drag force acting on the particles is too small to overcome the buoyance force. Particles are partially fluidized when increasing U_g to 12.5 mm/s as shown in Figure 2.27 (b). However, most particles are still in the packed bed state. Under U_g=15 mm/s, the particle distribution in the axial direction is nearly uniform and the three-phase fluidized bed expands to the entire column as shown in Figure 2.27 (c). By further increasing U_g to 20 mm/s, the axial solids distribution becomes less uniform where the solid phase is dense at the lower section and dilute at the upper section of the column as shown in Figure 2.27 (d) although all the particles are still fluidized in the entire column. The non-uniformity of the particle distribution becomes worse when increasing U_g further as shown Figure 2.27(e). More particles are accumulated at the bottom of the column and a free board region at the upper section of the column is formed when U_g= 40 mm/s. Thus, it can be concluded that with an increase in the inlet superficial gas velocity, more particles move downward along the column, which results in a bottom dense and upper dilute profile of the solids concentration.

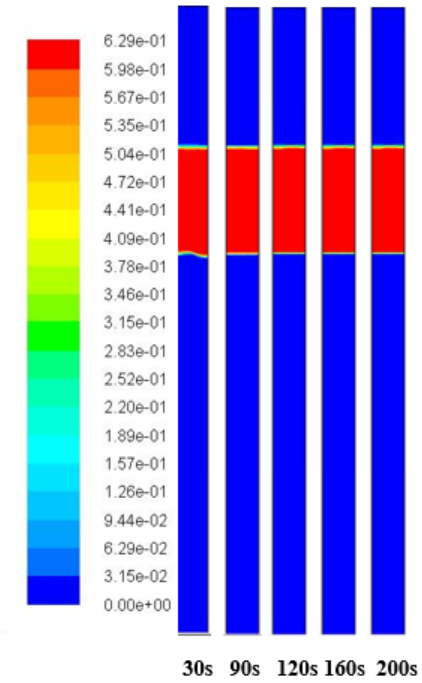

(a) Ug=9mm/s

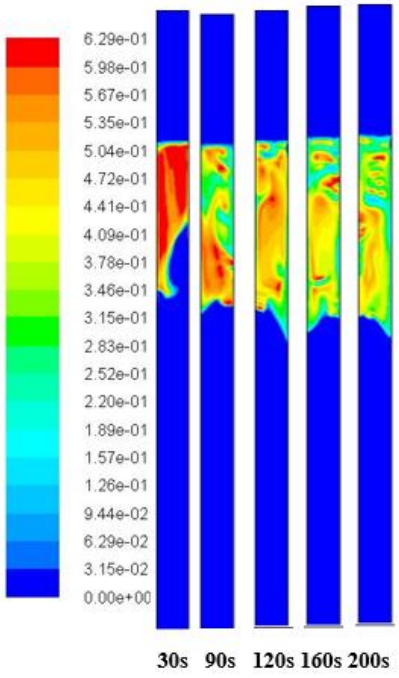

(b) Ug=12.5mm/s

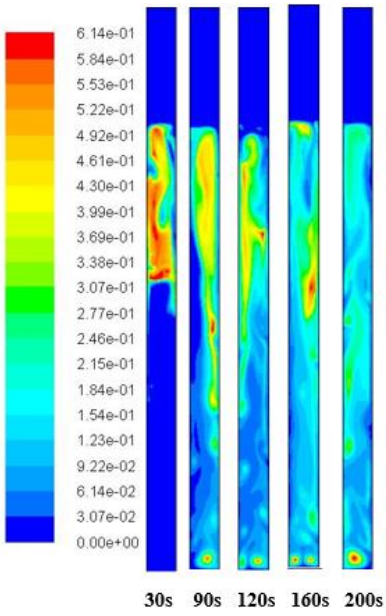

(c) Ug=15mm/s

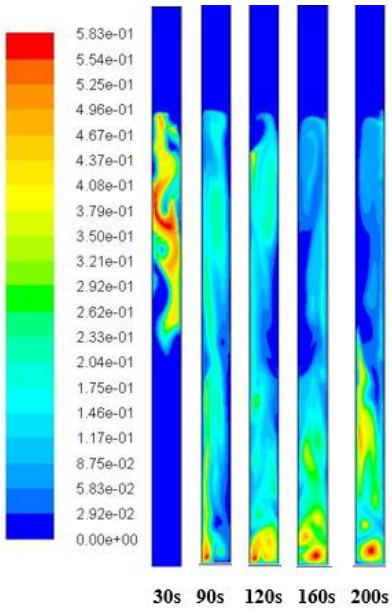

(d) Ug=20mm/s

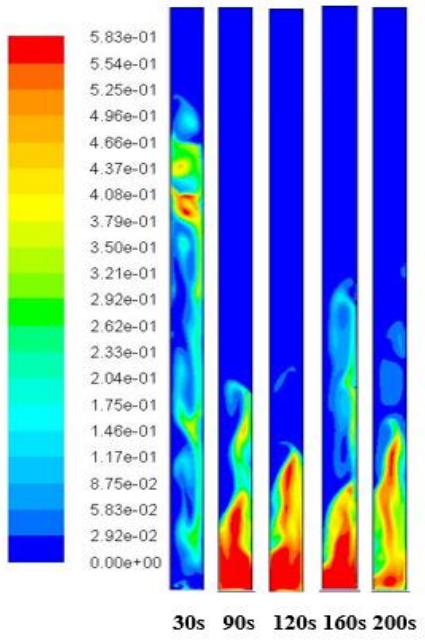

(e) Ug=40mm/s

Figure 2.27 Contours of the solids volume fraction under different inlet superficial velocities at 15% solids loading and ρ_s=930 kg/m^3

(a) U_g= 9mm/s, (b) U_g=12.5mm/s, (c) U_g=15mm/s, (d) U_g=20mm/s and (e) U_g=40mm/s

Figure 2.28 shows the radial profiles of the solids holdup under different inlet superficial gas velocities at different axial locations along the column (H=0.5 m and H=1.5 m) with 15% solids loading and 930 kg/m^3 particle density. At H=0.5 m, the maximum concentration of the solid phase occurs when the inlet superficial gas velocity is the highest (U_g=40 mm/s) because more particles settle down and accumulate at the lower section of the column. At H=1.5 m, the solids volume fraction at U_g=40 mm/s is the smallest, which fluctuates around 0.03. The solids volume fraction difference at H=1.5 m and H= 0.5 m is highest at U_g=40 mm/s, so particles under U_g=15 mm/s and U_g=20 mm/s can be better mixed with the liquid phase. The radial non-uniform distribution of the solid phase, which is dense at the center and dilute at the wall, can be found at both axial locations under all inlet superficial velocities. U_g=40 mm/s gives the most non-uniformity in the radial profiles of the solids holdup. Therefore, increasing the inlet superficial gas velocity will lead to a more radial non-uniform distribution of the solids holdup.

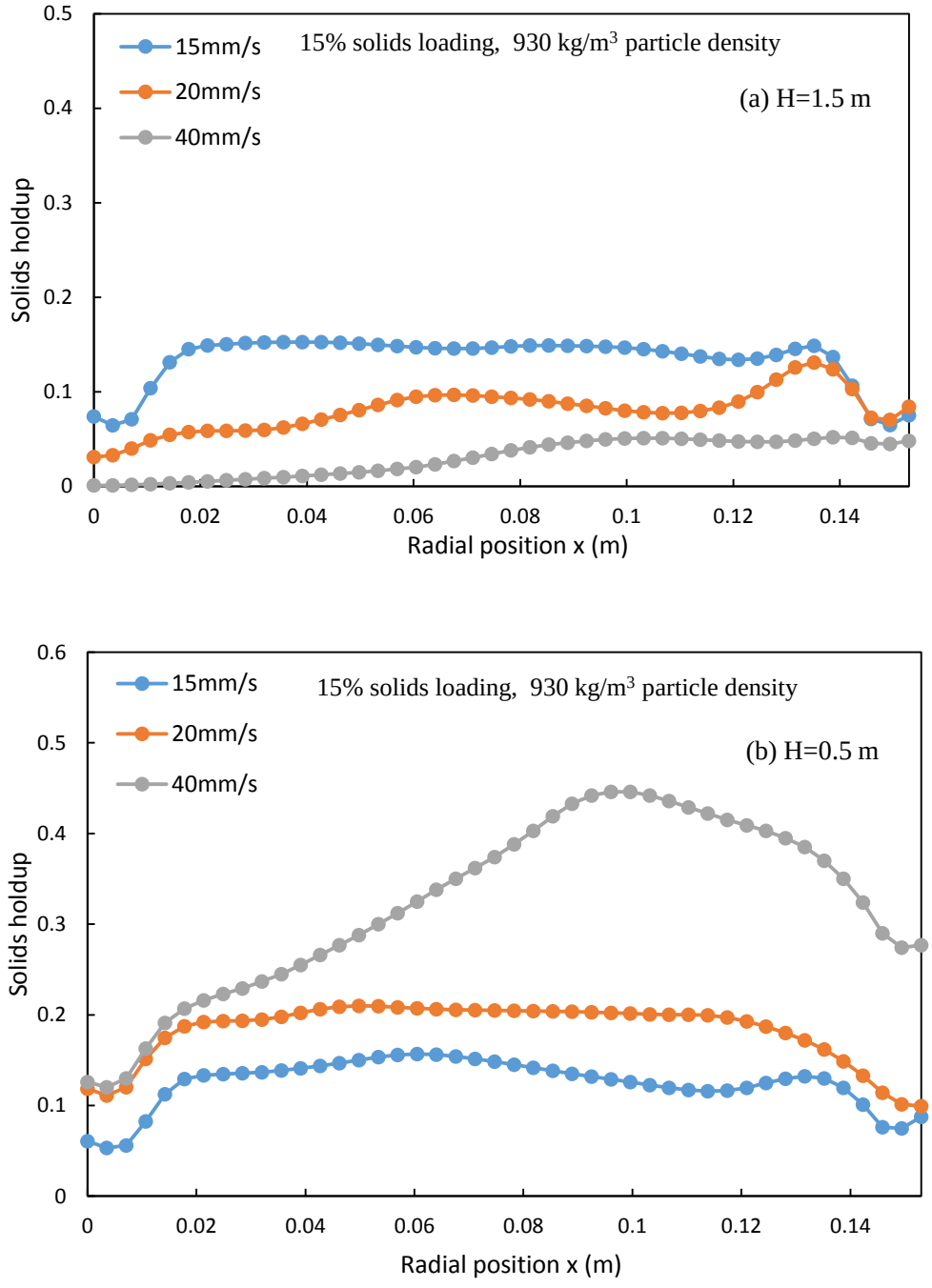

Figure 2.28 Radial profiles of the solids volume fraction under different inlet superficial gas velocities

(a) H=1.5m and (b) H=0.5m

The studies on the hydrodynamics at the fully developed stage under different particle densities, which are 904 kg/m^3, 930kg/m^3 and 950kg/m^3, were conducted at U_g=15 mm/s and 15% solids loading. The average gas holdups under different particle densities are shown in Figure 2.29. It can be seen that the average gas holdup under different particle densities are almost identical because the gas holdup mainly depends on the inlet superficial gas velocity.

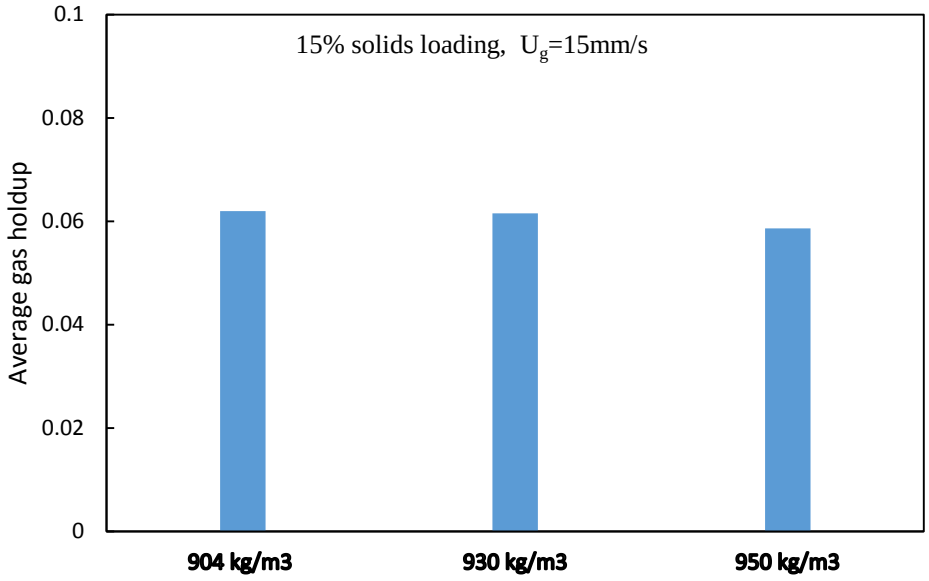

Figure 2.29 Average gas holdup under different particle densities at U_g=15mm/s, and 15% solids loading

Figure 2.30 shows the contours of the solid phase volume fraction from t=30s to 250s under different particle densities. It is noted that particles with a mean density of 904 kg/m^3 are only partially fluidized under U_g=15 mm/s, and most particles still remain packed as shown in Figure 2.30 (a). The particles with a mean density of 930 kg/m^3 are uniformly distributed along the column shown in the Figure 2.30 (b). The contours of the volume fraction of particles with a mean density of 950 kg/m^3 (Figure 2.30 (c)) indicate that the concentration of the solid phase is dense at the lower section and dilute at the upper part of the column. Thus, the particles with a higher density are easier to be fluidized in an inverse TPFB under the batch mode.

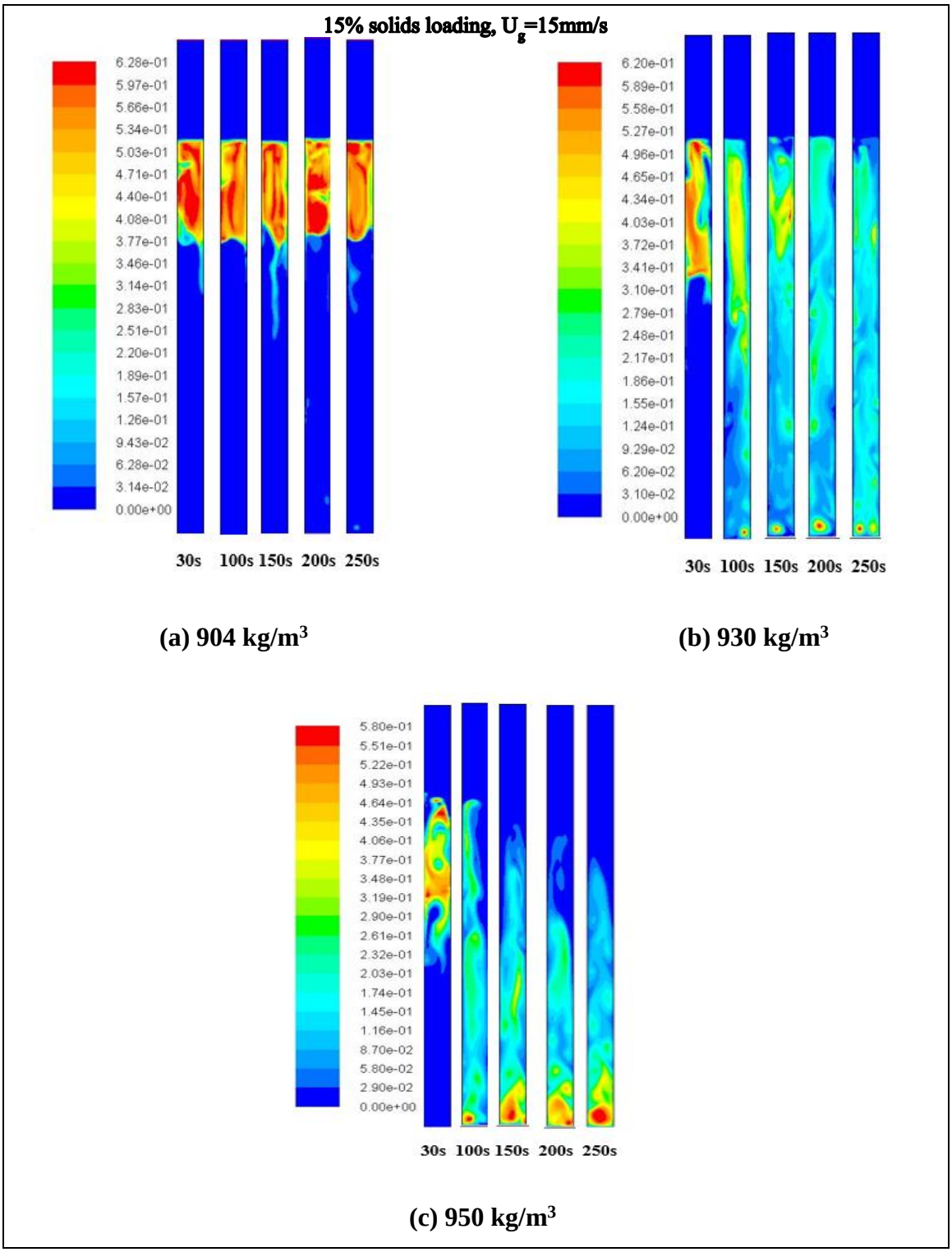

Figure 2.30 Contours of the solids volume fraction with different particle densities at 15% solids loading and U_g=15mm/s

(a) 904 kg/m^3, (b) 903 kg/m^3 and (c) 950kg/m^3

The time-averaged radial profiles of the solids holdup for different particle densities at two axial locations are shown in Figure 2.31. At H=0.5 m, the particles with 950 kg/m^3 density have the maximum solids volume fraction. The particles with 904 kg/m^3 density have the minimum solids volume fraction at both H=0.5 m and H=1.5 m because most particles are still packed at the upper part of the column. Three types of particles with different densities all have the radial non-uniform profiles of the solids holdup. The solids holdup for particles with 904 kg/m^3 at H=1.5 m is dense at the near wall region and dilute at the center region, which is different from other particles. This is due to the liquid recirculation caused by the upward flow of gas bubbles, which fluidizes the particles at the near wall region first, so more particles at the near wall region move to the lower section of the column first.

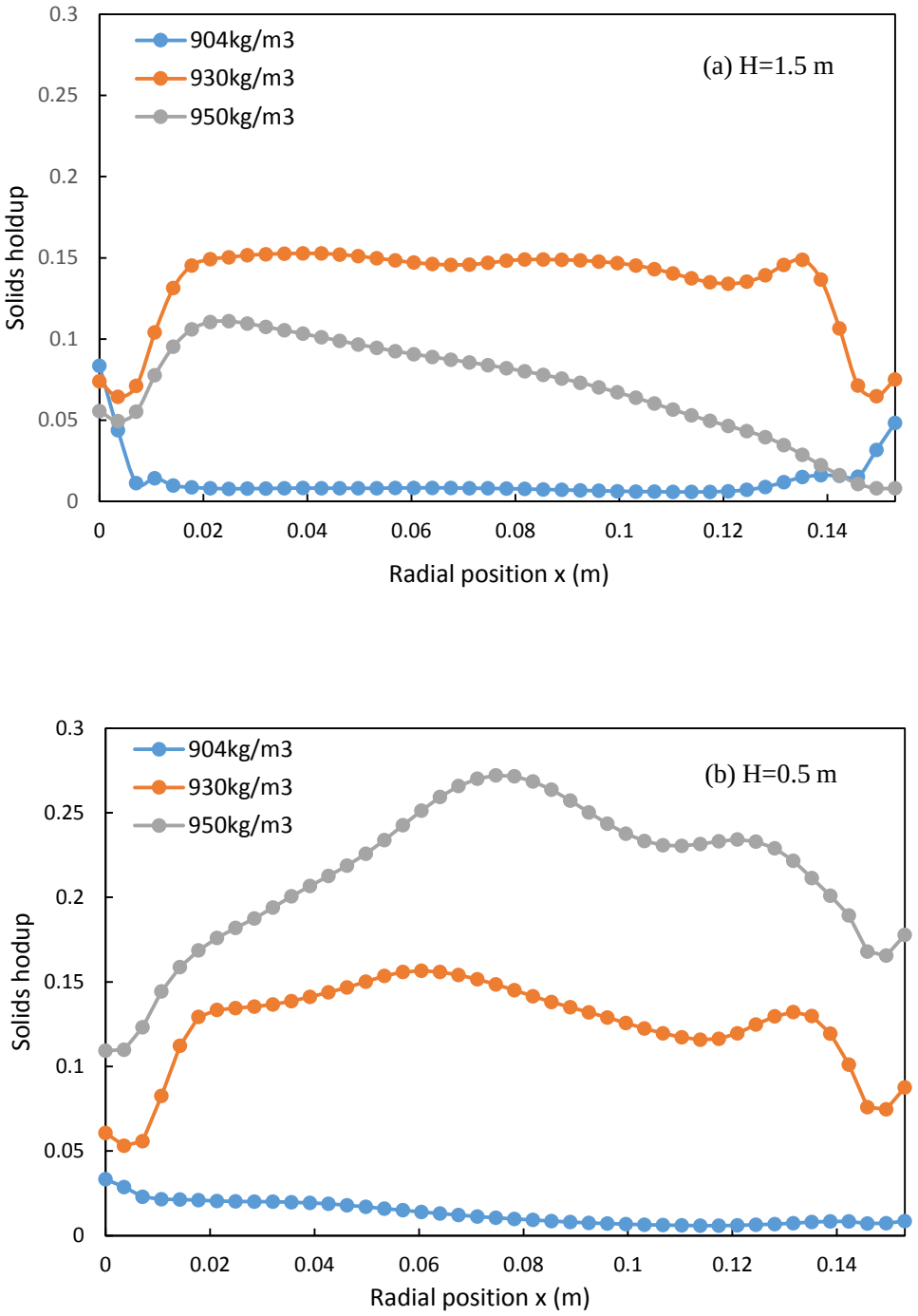

Figure 2.31 Radial profiles of solids holdup with different particle densities at 15% solids loading and U_g=15mm/s

(a) H=1.5m and (b) H=0.5m

2.5.5 Recirculation

In an inverse TPFB under the batch liquid mode (U_l=0), the gas phase is injected into the system from the bottom of the column as bubbles, and gas bubbles flow upward. The rising gas bubbles from the bottom of the column can induce the turbulence with small eddies in the system. However, under the batch liquid mode of the inverse TPFB, the liquid is not circulated out of the column. Therefore, the recirculation of the liquid and solid phases can be observed in the inverse TPFB. The recirculation of the liquid and solid phases is an important phenomenon because it can influence the heat and mass transfer in the inverse TPFB under the batch mode. The vortex and particle recirculation are also observed in the experimental study by Sun (2017). Therefore, the investigation of the recirculation of particles is carried out in this section. The simulation is conducted under 15% solids loading and particles with 930 kg/m^3 density, but different inlet superficial velocities are employed.

Figure 2.32 is the time-averaged radial profiles of the solids axial velocity at the fully developed stage. The radial non-uniform distribution of the solids axial velocity can be seen under all inlet superficial gas velocities. When $U_{g=}$15 mm/s, particles flow downward at the near wall region and the core region of the column, but upward particle flows can be found at the region between the wall and center of the column at both H=1.5 m and H=0.5 m. Particles flow upward at the core region and flow downward at the near wall region when $U_{g=}$20 mm/s at both axial locations, and particles under U_g=40 mm/s also move in both upward and downward directions. Therefore, the recirculation of particles can be found under all inlet superficial gas velocities through the radial profiles of the solids axial velocity. Besides, it can be seen that the radial profile of the solids axial velocity is most non-uniform at U_g=40 mm/s. Thus, with the increase in the inlet superficial gas velocity, the radial non-uniformity of the solids axial velocity will increase. The maximum upward and downward solids axial velocities for U_g=40 mm/s are higher than those for U_g=15 mm/s and U_g=20 mm/s, which indicates a stronger recirculation for U_g=40 mm/s than other two cases, because with the increase in the inlet superficial gas velocity, the liquid and solid phases can obtain more momentum from the gas phase.

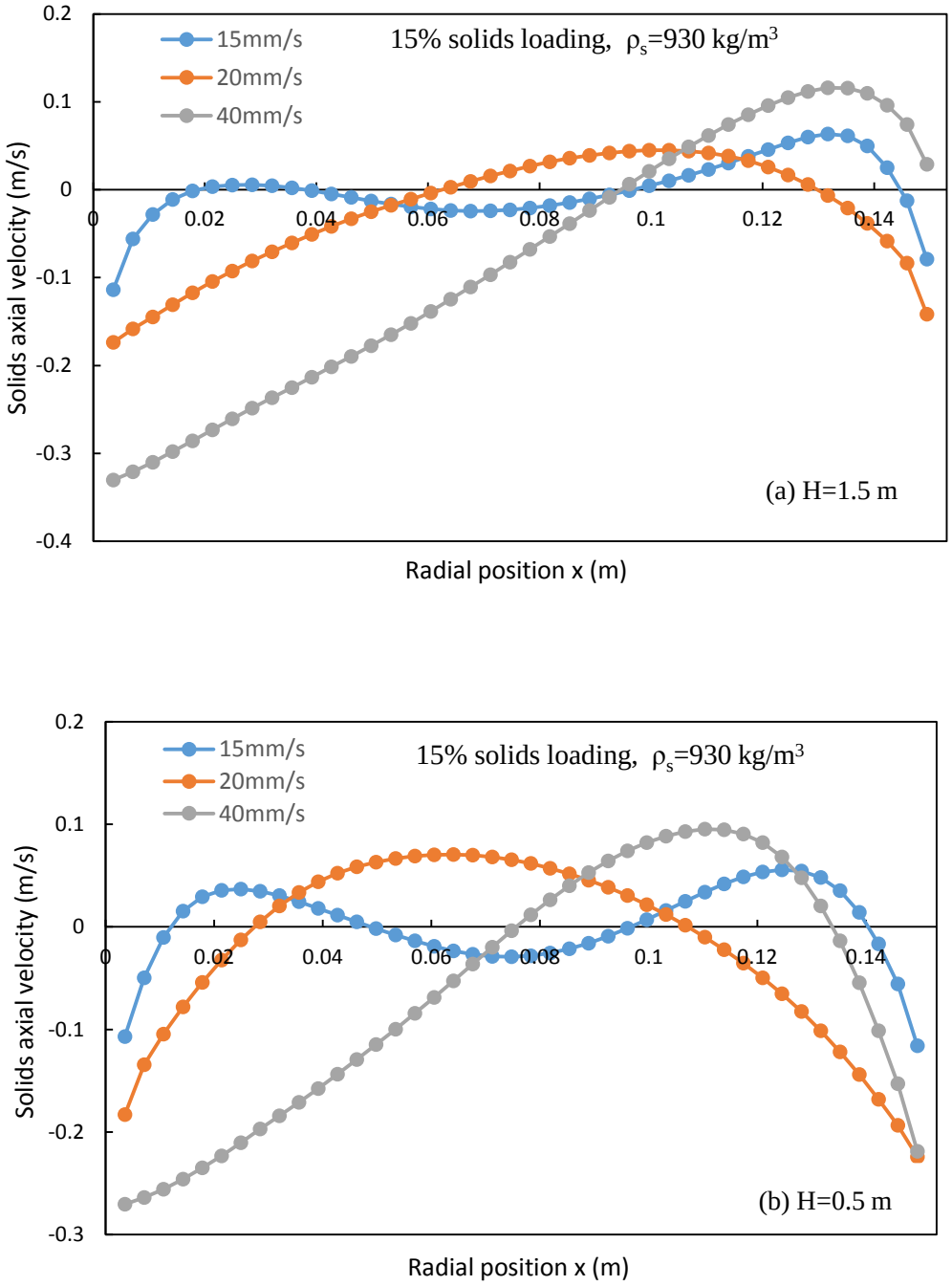

Figure 2.32 Radial profiles of the solids axial velocity under different inlet superficial gas velocities

(a) H=1.5m and (b) H=0.5m

To further investigate the recirculation in the inverse TPFB under the batch mode, the flow details in all three stages of the fluidization process are studied at U_g=15 mm/s, 15% solids loading and ρ_s=930 kg/m^3. Figure 2.33(a) shows the solids volume fraction contour and solids veolcity vector at the initial fluidization stage. A recirculation of particles can be observed at the bottom part of the packed bed from the velocity vector plot, where the particles descends at the near wall region on the left hand side and rise at the near wall region on the right hand side of the column, which is similar to the radial profiles of solids axial velocity shown in Figure 2.08. It can be seen from Figure 2.33 (a), at the bottom part of the packed bed, particle velocities at the near wall regions are higher than the velocities at the center region of the column, which indicates that the particles at the near wall region are fluidized first at the initial fluidization stage. The solid velocity vector and solids volume fraction at the developing stage are shown in Figure 2.33 (b). A large circulation of particles can be seen at the middle and upper part of the reactor. In addition, more vortexes are found at the lower section of the column, close to the gas distributor. So the flow of particles is more disordered and the solids volume fraction distribution is very non-uniform. Figure 2.33 (c) shows the solids velocity vector and solids volume fraction at the fully developed stage. The large recirculation of particles can be found inside the column. Therefore, it can be concluded that the recirculation of particles exists at all three stages.

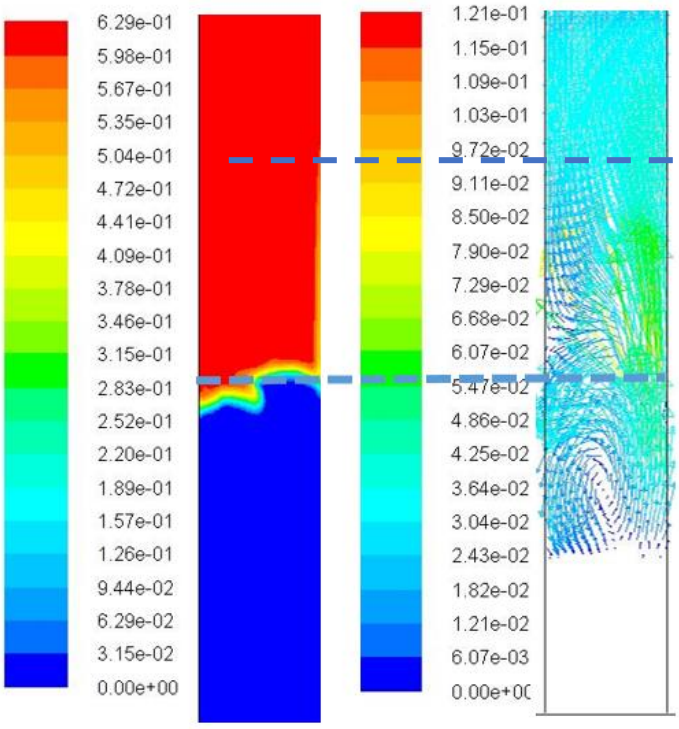
6.29e-01
5.98e-01
5.67e-01
5.35e-01
5.04e-01
4.72e-01
4.41e-01
4.09e-01
3.78e-01
3.46e-01
3.15e-01
2.83e-01
2.52e-01
2.20e-01
1.89e-01
1.57e-01
1.26e-01
9.44e-02
6.29e-02
3.15e-02
0.00e+00
1.21e-01
1.15e-01
1.09e-01
1.03e-01
9.72e-02
9.11e-02
8.50e-02
7.90e-02
7.29e-02
6.68e-02
6.07e-02
5.47e-02
4.86e-02
4.25e-02
3.64e-02
3.04e-02
2.43e-02
1.82e-02
1.21e-02
6.07e-03
0.00e+00
Middle part
Bottom part

(a)

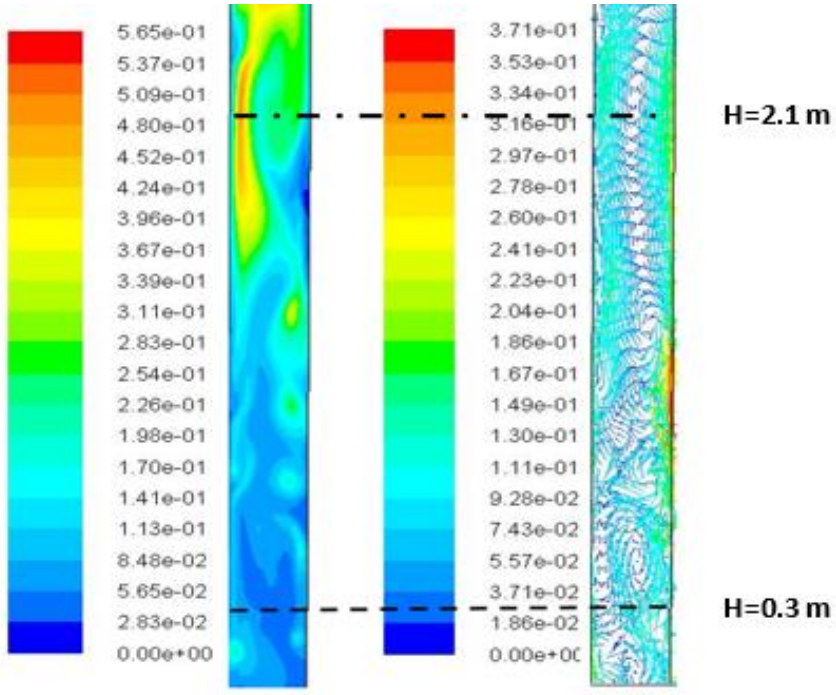
5.65e-01
5.37e-01
5.09e-01
4.80e-01
4.52e-01
4.24e-01
3.96e-01
3.67e-01
3.39e-01
3.11e-01
2.83e-01
2.54e-01
2.26e-01
1.98e-01
1.70e-01
1.41e-01
1.13e-01
8.48e-02
5.65e-02
2.83e-02
0.00e+00
3.71e-01
3.53e-01
3.34e-01
3.16e-01
2.97e-01
2.78e-01
2.60e-01
2.41e-01
2.23e-01
2.04e-01
1.86e-01
1.67e-01
1.49e-01
1.30e-01
1.11e-01
9.28e-02
7.43e-02
5.57e-02
3.71e-02
1.86e-02
0.00e+00
H=2.1 m
H=0.3 m

(b)

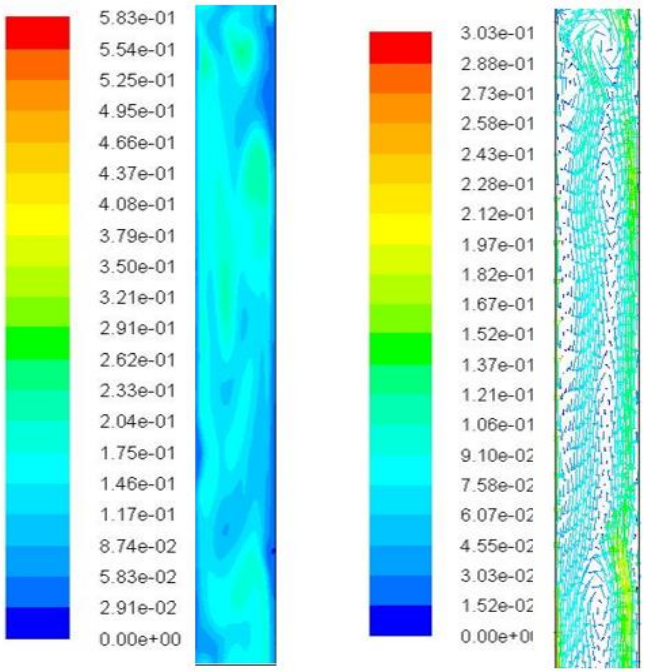

Solids volume fraction **Solids velocity vector**

(c)

Figure 2.33 Instantaneous volume fraction contour (left) and particle velocity vector contour (right)

(a) Initial fluidization stage, (b) Developing stage and (c) Fully developed stage

2.6 Conclusions

A three-phase Eulerian-Eulerian CFD model coupled with the kinetic theory of the granular flow has been developed for simulation of the inverse TPFB under the batch liquid mode, and it is validated with experimental data. A two-dimensional numerical simulation has been conducted in order to study the hydrodynamics and flow structures in an inverse TPFB. The flow development in the inverse three-phase fluidization process is investigated under conditions of U_g=15 mm/s, 15% solids loading, and 903 kg/m^3 particle density. The CFD results show that flow development in the inverse three-phase fluidization system can be divided into three stages, which are the initial fluidization stage, developing stage and fully developed stage based on the axial profile of the solid phase. The fluidization of particles was found to begin from the near wall region firstly due to the liquid recirculation

caused by the upward gas flow at the initial fluidization stage. The radial non-uniform profile of the gas holdup, solids holdup and solids axial velocity are shown at all three stages. The radial non-uniformity decreases with time, so the radial flow structure is more uniform at the fully developed stage. In addition, it is noted that a higher solids volume fraction occurs where particles flow upward, and a lower solids volume fraction is at where the particle moves downward at all three stages.

The effect of the solids loading on the flow structure has been studied through CFD modeling under U_g=15 mm/s. It is noted that the time to reach to the developing stage and fully developed stage is longer with a higher solids loading, so the particles with higher solids loading are more difficult to be fluidized. Besides, by applying different inlet superficial velocities with 15% solids loading, it is noted the time to reach to the developing stage and fully developed stage is reduced with the increase in the inlet superficial gas velocity under the same solids loading. The radial non-uniformity of the solids holdup increases with the increase in the solids loading. However, the solids loading has almost no effect on the radial distribution of the gas holdup.

The general flow structure at the fully developed stage including the radial solids distribution, axial solids distribution and gas holdup are also investigated under different inlet superficial gas velocities and particle densities. More particles move downward when increasing U_g. Particles are easier to be fluidized when its density is close to the liquid phase density, so the solid phase becomes denser at the lower section and dilute at the upper section of column when increasing the particle density. For the radial flow structure, the radial non-uniform profile of the solids holdup is observed at different inlet superficial velocities and particle densities. The radial non-uniformity of the solids holdup increases when increasing U_g, but it is not affected by the particle density. The particle density has almost no effect on the average holdup as well. In addition, it is found that the recirculation of particles exists at all three stages in the inverse fluidized bed under the batch liquid mode.

Reference

Ansys. Inc. (2014). Fluent 16.0 User's Guide.

Bandaru, K. S. V. S. R., Murthy, D. V. S., & Krishnaiah, K. (2007). Some hydrodynamic aspects of 3-phase inverse fluidized bed. *China Particuology*, *5*(5), 351–356. https://doi.org/https://doi.org/10.1016/j.cpart.2007.06.002

Buffière, P., & Moletta, R. (1999). Some hydrodynamic characteristics of inverse three phase fluidized-bed reactors. *Chemical Engineering Science*, *54*(9), 1233–1242. https://doi.org/10.1016/S0009-2509(98)00436-9

Cho, Y. J., Park, H. Y., Kim, S. W., Kang, Y., & Kim, S. D. (2002). Heat transfer and hydrodynamics in two- and three-phase inverse fluidized beds. *Industrial and Engineering Chemistry Research*, *41*(8), 2058–2063. https://doi.org/10.1021/ie0108393

Comte, M. P., Bastoul, D., Hebrard, G., Roustan, M., & Lazarova, V. (1997). Hydrodynamics of a three-phase fluidized bed - The inverse turbulent bed. *Chemical Engineering Science*, *52*(21–22), 3971–3977. https://doi.org/10.1016/S0009-2509(97)00240-6

Ding, J., & Gidaspow, D. (1990). A bubbling fluidization model using kinetic theory of granular flow. *AIChE Journal*, *36*(4), 523–538. https://doi.org/10.1002/aic.690360404

Fan, L. S., Muroyama, K., & Chern, S. H. (1982). Hydrodynamic characteristics of inverse fluidization in liquid-solid and gas-liquid-solid systems. *The Chemical Engineering Journal*, *24*(2), 143–150. https://doi.org/10.1016/0300-9467(82)80029-4

Feng, W., Wen, J., Fan, J., Yuan, Q., Jia, X., & Sun, Y. (2005). Local hydrodynamics of gas–liquid-nanoparticles three-phase fluidization. *Chemical Engineering Science*, *60*(24), 6887–6898. https://doi.org/https://doi.org/10.1016/j.ces.2005.06.006

Gidaspow, D. (1994). *Multiphase Flow and Fluidization: Continuu and Kinetic Theory Descriptions*. Boston: Acad. Press.

Grevskott, S., Sannaes, B. H., Dudukovic, M. P., Hjarbo, K. W., & Svendsen, H. F. (1996). Liquid circulation, bubble size distributions, and solid movement in two- and three-phase bubble columns. *Chemical Engineering Science*, *51*(10), 1703. https://doi.org/https://doi.org/10.1016/0009-2509(96)00029-2

Hamidipour, M., Chen, J., & Larachi, F. (2012). CFD study on hydrodynamics in three-phase fluidized beds — Application of turbulence models and experimental validation. *Chemical Engineering Science*, *78*, 167–180. https://doi.org/10.1016/j.ces.2012.05.016

Hillmer, G., & Weismantel, L. (1994). Investigations and Modelling Columns of Slurry

Bubble. *Science*, *49*(6), 837–843. https://doi.org/https://doi.org/10.1016/0009-2509(94)80020-0

Ibrahim, Y. A. A., Briens, C. L., Margaritis, A., & Bergongnou, M. A. (1996). Hydrodynamic Characteristics of a Three-Phase Inverse Fluidized-Bed Column. *AIChE Journal*, *42*(7), 1889–1900. https://doi.org/10.1002/aic.690420710

Lee, D. H., Epstein, N., & Grace, J. R. (2000). Hydrodynamic Transition from Fixed to Fully Fluidized Beds for Three-Phase Inverse Fluidization. *Korean Journal of Chemical Engineering*, *17*(6), 684–690. https://doi.org/10.1007/BF02699118

Li, W., & Zhong, W. (2015). CFD simulation of hydrodynamics of gas-liquid-solid three-phase bubble column. *Powder Technology*, *286*, 766–788. https://doi.org/10.1016/j.powtec.2015.09.028

Li, Y., Zhang, J., & Fan, L.-S. (1999). Numerical simulation of gas–liquid–solid fluidization systems using a combined CFD-VOF-DPM method: bubble wake behavior. *Chemical Engineering Science*, *54*(21), 5101–5107. https://doi.org/https://doi.org/10.1016/S0009-2509(99)00263-8

Lun, C. K. K., Savage, S. B., Jeffrey, D. J., & Chepurniy, N. (1984). Kinetic theories for granular flow: Inelastic particles in Couette flow and slightly inelastic particles in a general flowfield. *Journal of Fluid Mechanics*, *140*(1), 223–256. https://doi.org/10.1017/S0022112084000586

Muroyama, K., & Fan, L. - S. (1985). Fundamentals of gas- liquid- solid fluidization. *AIChE Journal*, *31*(1), 1–34. https://doi.org/10.1002/aic.690310102

Panneerselvam, R., Savithri, S., & Surender, G. D. (2009). CFD simulation of hydrodynamics of gas–liquid–solid fluidised bed reactor. *Chemical Engineering Science*, *64*(6), 1119–1135. https://doi.org/https://doi.org/10.1016/j.ces.2008.10.052

Renganathan, T., & Krishnaiah, K. (2008). Prediction of Minimum Fluidization Velocity in Two and Three Phase Inverse Fluidized Beds. *The Canadian Journal of Chemical Engineering*, *81*(3–4), 853–860. https://doi.org/https://doi.org/10.1002/cjce.5450810369.

Schaeffer, D. G. (1987). Instability in the evolution equations describing incompressible granular flow. *Journal of Differential Equations*, *66*(1), 19–50. https://doi.org/10.1016/0022-0396(87)90038-6

Schiller, L., & Naumann, A. (1935). A drag coefficient correlation. *Z. Ver. Deutsch. Ing*, *77*, 318–320.

Sun, X. (2017). *Bubble induced Inverse Gas-liquid-solid Fluidized bed*. University of Western Ontario.

Syamlal, M., Rogers, W., & O`Brien, T. J. (1993). *MFIX documentation theory guide*.

United States. https://doi.org/10.2172/10145548

Wen, J., & Xu, S. (1998). Local hydrodynamics in a gas-liquid-solid three-phase bubble column reactor. *Chemical Engineering Journal*, *70*(1), 81–84. https://doi.org/10.1016/S1385-8947(97)00120-4

Wu, Y., & Gidaspow, D. (2000). Hydrodynamic simulation of methanol synthesis in gas-liquid slurry bubble column reactors. *Chemical Engineering Science*, *55*(3), 573–587. https://doi.org/https://doi.org/10.1016/S0009-2509(99)00313-9

Yakhot, V., & Orszag, S. A. (1986). Renormalization group analysis of turbulence. I. Basic theory. *Journal of Scientific Computing*, *1*(1), 3–51. https://doi.org/10.1007/BF01061452

Zhang, D. Z., & Vanderheyden, W. B. (2002). The effects of mesoscale structures on the disperse two-phase flows and their closures for dilute suspensions . *Int. J. Multiphase Flows*, *28*(5), 805–822. https://doi.org/https://doi.org/10.1016/S0301-9322(02)00005-8

Chapter 3

3 Modification of the CFD Model Based on the Bubble Size Adjustment for the Inverse Three-phase Fluidized Bed

3.1 Introduction

Fluidization is a process that converts particles from the solid like state to a fluid like state by injecting liquid or gas flow into the system. With different fluidizing agents, fluidized beds can be categorized as the liquid-solid two-phase fluidization, gas-solid two-phase fluidization and gas-liquid-solid three-phase fluidization. The gas-liquid-solid three-phase fluidized bed (TPFB) has many applications in chemical, biochemical, petrochemical industries because it has a higher contact efficiency among each phase and good mass and heat transfer features (Muroyama & Fan, 1985). Fluidized beds can be further divided into the upward fluidized bed and inverse fluidized bed based on the flow direction of the fluidizing agent. In inverse TPFBs, the particle density is usually less than the liquid density, so the fluidization process will start when the drag force and gravity on the particle are balanced with the buoyancy force. The inverse gas-liquid-solid (GLS) fluidized bed can be operated under a continuous mode or batch liquid mode. Only gas is introduced into the fluidized bed at a certain velocity to fluidize the liquid and solids inside the column under the batch liquid mode. Under the continuous mode, both gas and liquid work as the fluidizing agents to fluidize the packed solids inside the fluidized bed. Compared with the traditional upward three-phase fluidized bed, the inverse TPFB has some advantages such as the lower energy cost.

In an inverse TPFB, the fluidization process will go through the fixed bed with dispersed bubble regime, bubbling fluidized bed regime, transition regime and slugging fluidized bed regime when increasing the liquid or gas velocity (Fan et al., 1982). Three significant superficial gas velocities have been defined to distinguish the flow regimes in an inverse TPFB under the batch liquid mode, which are (1) the minimum gas fluidization velocity U_{g1} that can break the fixed bed, (2) velocity U_{g2} is the velocity that can let some particle to reach the bottom of the column, and (3) velocity U_{g3} that can result in a uniform axial

particle distribution (Comte et al., 1997; Sun, 2017). It was found that U_{g2} and U_{g3} will decrease with an increase in the solids loading or particle density.

Other parameters and characteristics of the hydrodynamics in the inverse TPFB have been studied by a few researchers. The minimum liquid fluidization velocity was found to decrease with the increase in the gas velocity, and the average liquid holdup and gas holdup was found to increase with the increase in the superficial gas and liquid velocities (Bandaru et al., 2007; Cho et al., 2002; D. H. Lee et al., 2000). A correlation was developed by Renganathan & Krishnaiah (2008), which can predict the minimum fluidization velocity in the inverse TPFB under both the batch mode and continuous mode. Ibrahim et al. (1996) and Bandaru et al. (2007) studied the axial phase holdup in the inverse TPFB. The solid phase was found to become dilute at the top of the column and dense at the bottom when increasing the gas velocity or liquid velocity. Later, Sun (2017) reported similar results on the average holdup and axial distribution of each phases in the inverse TPFB under the batch mode. However, no studies on the hydrodynamics and flow patterns of an inverse TPFB in the radial direction were reported in the literatures.

For the bubble induced three-phase fluidization, the gas, which is introduced into the column, is usually present in the form of small bubbles with the help of the gas distributor. It was found that small gas bubbles and the density difference between the solid phase and the liquid-gas mixture would result in the liquid recirculation, which causes the bed to expand in the inverse TPFB under the batch liquid mode. (Buffière & Moletta, 1999; Renganathan & Krishnaiah, 2008). In that case, the bubble behavior has become an important role in the design and operation of the inverse TPFB under the batch liquid mode since bubbles related to the mass transfer and mixing in the TPFB. However, only a fewer literatures reported the relationship between the average bubble size, the inlet superficial gas velocity and the gas holdup, such as a correlation for an upward gas-liquid bubble column under the superficial gas velocities ranging from 0-12 cm/s (Jamialahmadi & Muller-Steinhagen, 1993). Less research works on the bubble behavior in the inverse TPFB were carried during the past decades.

For the inverse gas-liquid two-phase bubble column, Son et al. (2004) studied the bubble behavior and properties in a gas-liquid countercurrent flow bubble column, which is used for wastewater treatment. Four pipes in 6.35 mm diameter with 28 holes were used as the gas distributor in this experimental study, and the gas distributor is evenly installed at the bottom of the column. A correlation to calculate the bubble size based on the superficial liquid velocity and gas velocity was developed in their study. It was also found that the gas holdup under the batch liquid mode is smaller than the gas holdup under the continuous mode in a gas-liquid countercurrent bubble column.

Compared to the gas-liquid two-phase flow in a bubble column, less researchers reported studies on the bubble behaviors in inverse three-phase fluidized beds. Cho et al. (2002) reported that the bubble size and bubble rising velocity will increase when increasing the gas velocity in an inverse TPFB under the continuous mode. Later, Son et al. (2007) used the same experimental equipment that was used by Son et al. (2004) to study the bubble behaviors in an inverse TPFB under the continuous mode. The experimental study was conducted at U_l=10 mm/s - 50 mm/s, U_g= 0.5 mm/s - 8 mm/s and ρ_s =877.3 kg/m^3 - 966.6 kg/m^3. A correlation for the bubble size and bubble rising velocity based on the drift flux model was developed. It was also found that the bubble size increases with the increase in the gas velocity, liquid viscosity or liquid velocity, but it will decrease when increasing the particle density. The bubble rising velocity was found to increase with an increase in the gas velocity or liquid viscosity.

However, no studies have reported the average bubble size in the inverse TPFB under the batch liquid mode (U_l=0) due to the inadequate experiments and the limitation of the visualization techniques. The CFD method allows the model to include the effect of the bubble size, which can be used to further study the relationship between the bubble size and the inlet superficial gas velocity. Thus, the modification of the CFD model proposed in the previous work for the simulation of the flow in the inverse TPFB is carried out to include the effect of the bubble size on the flow field in the inverse TPFB.

The Eulerian-Lagrangian approach and Eulerian-Eulerian approach are the two main methods that, are used to simulate the three-phase flows in fluidized beds. In the Eulerian-

Lagrangian approach, the liquid and gas phases are treated as the continuous phases. The solid phase is treated as the discrete phase, and each individual particle is tracked by solving the Lagrangian force balance equation. Due to the high computational cost, the Eulerian-Lagrangian approach is used when the volume fraction of discrete phase is low. Thus, the Eulerian-Eulerian approach coupled with the kinetic theory of the granular flow (KTGP) is widely used for simulating the flow in the TPFBs. Each phase is treated as a continuum solved by governing equations in the Eulerian-Eulerian approach. The KTGP is used to calculate the solid phase pressure, viscosity and stress. The Eulerian-Eulerian approach can be divided into the pseudo two-fluid model and three-fluid Eulerian-Eulerian model when simulating three-phase flows. The pseudo two-fluid model is used when the particle or bubble size is small, the volume fraction of the solid or gas phase is low and the slip velocity between the two phases is low. Therefore, the liquid-gas or liquid-solid can be treated as one phase. Thus, the three-phase flows in the fluidized bed can be simplified to a two-phase flows. The pseudo two-fluid model is often used to simulate the flow in the three-phase slurry fluidized bed or the fluidized bed that uses nanoparticles (Feng et al., 2005; Grevskott et al., 1996; Hillmer & Weismantel, 1994; Wen & Xu, 1998). Besides, the Eulerian-Eulerian three-fluid model is often needed to simulate the flow in the gas-liquid-solid TPFB. Due to the complicated interacton among each phase in the TPFB, fewer CFD studies have been carried out to predict the hydrodynamcis and flow patterns in the TPFB based on the three-fluid Eulerian-Eulerian model. Panneerselvam et al. (2009) studied the hydrodynamics and flow pattern in an upward TPFB numerically. Two different superficial gas velocities, U_g = 0.2 m/s and U_g=0.4 m/s, were used in the simulation. The mean bubble sizes used for the gas phase at each inlet superficial gas velocity are 13 mm and 2 mm, respectively, which was determined by comparing the gas holdup from the simulation results with that from the experimental data. Hamidipour et al. (2012) conducted the same numerical study as Panneerselvam et al. (2009) by using the three-fluid Eulerian-Eulerian model with the KTGP. The same bubble size was used in their study as well. Li and Zhong (2015) carried out a numerical study in a TPFB based on the three-fluid Eulerian-Eulerian model. The performances of different drag models between each phase were compared. The range of the inlet superfical gas velocity in the study was from 0.036 m/s to 0.33 m/s,

but only one mean bubble size of 0.003 m was used in the simulations for different inlet superfical gas veolcities.

It is believed that the bubble size in a TPFB increases with the increase in the superficial gas velocity. (Kulkarni & Joshi, 2005; Son et al., 2004, 2007). However, most numerical stuides on TPFBs used only one bubble size for the gas phase even under the different inlet superfical gas velocities. Thus, the objective of this study is to modify the CFD model for the simulation of the inverse TPFB under the batch liquid mode proposed in the previous study by adjusting the bubble size under different superfical gas velocities. Also, since the numerical studies on the bubble behavior in the inverse TPFB were conducted only for a very small operating range, investigations on the flows in an inverse TPFB under wide range of different operating conditions be conducted. And a correaltion to predict the bubble size under different inlet superfical gas velocities will be developed as well.

3.2 Experimental setup of the inverse three-phase fluidized bed

The proposed CFD model has been validated based on the experimental data by Sun (2017). The configuration of the inverse TPFB used by Sun (2017) is shown in Figure 3.1. The column is made of PVC with 0.153 m in diameter and 3 m in height. The ring shape porous quartz gas distributor with an 8.7 cm outer diameter and a 2.7 cm inner diameter, which can generate very small bubbles, is placed at the bottom of the column. The tap water, air and particles (ρ_s=930 kg/m^3) are used as liquid, gas and solid phases in the experiment. The tap water and particles are injected into the column before the experiment starts, resulting in the floated particles at the top surface of the water because the particle density is lower than the density of water. During the experiment, only the gas is continuously introduced into the column through the gas distributor, and there is no outflow for particles and liquid. The gas phase is injected into the column as small bubbles from the bottom of the column through the gas distributor, and bubbles leaves the column through the top of the column. The superficial gas velocity at the inlet is from 0 mm/s to 60 mm/s. With an increase in the inlet superficial gas velocity, the coalescence of small bubbles can be observed. The experiment is carried out under ambient temperature and pressure.

In this study, the hydrodynamics in the inverse TPFB will be simulated under different inlet superficial gas velocities with its corresponding bubble size. Therefore, different bubble sizes will be used under different inlet superficial gas velocities. The summary of the operating conditions and properties of each phase are shown in Table 3.1.

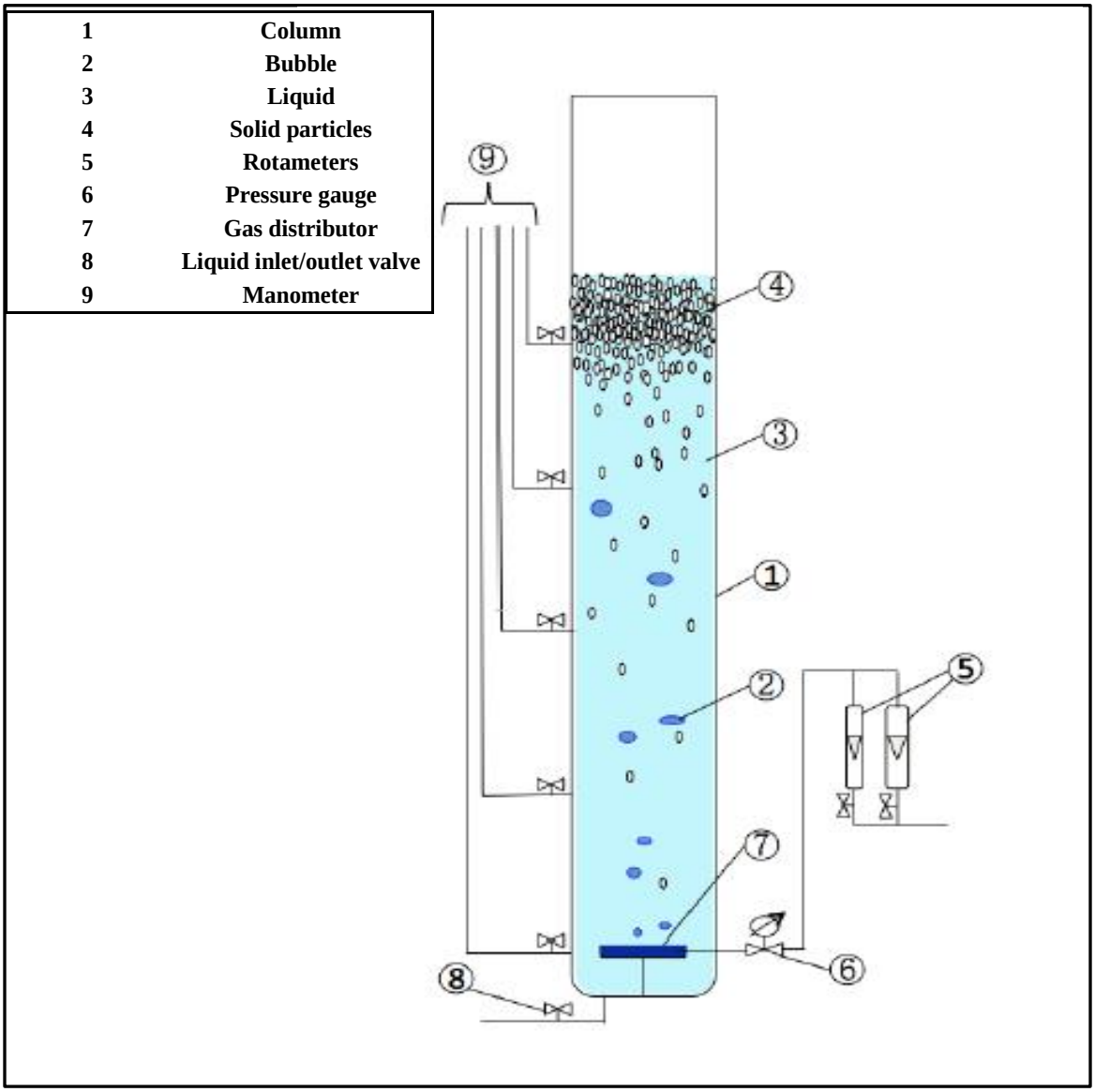

Figure 3.1 Configuration of the experimental setup of the inverse three-phase fluidized bed (Sun, 2017)

Table 3.1 Operating conditions and physical properties of each phase

Sun (2017)	Bubble column size (m)	Diameter: 0.153
		Total height: 3
	U_l (mm/s)	0
	U_g (mm/s)	9,20,30,40,50,60
	U_s (mm/s)	0
	Liquid phase	water
	Liquid phase density (kg/m$^{3)}$	998
	Liquid phase viscosity (kg/m$^{-s)}$	0.001003
	Gas phase	Air
	Gas phase density (kg/m$^{3)}$	1.225
	Gas phase viscosity (kg/m$^{-s)}$	1.7984×10^{-5}
	Solid phase	Polypropylene
	Particle diameter (mm)	3.5
	Particle density (kg/m$^{3)}$	930
	Solid phase loading	15%
	Pressure	atmospheric pressure
	Temperature	Ambient temperature

3.3 Numerical models

The CFD model used in this study to simulate the inverse gas-liquid-solid fluidized bed is based on the three-fluid Eulerian-Eulerian approach. Each phase is treated as interpenetrating continuum which is solved by governing equations. A Turbulence model and KTGP are used to close the governing equation. The liquid phase is set as the primary phase, and the gas and solid phases are the secondary phases in the simulation. The governing equation for each phase and corresponding closure law and constitutive relations are shown as following.

3.3.1Governing equations

Conservation equation of mass for the liquid phase

$$\frac{\partial}{\partial t}(\alpha_l \rho_l) + \nabla\,(\alpha_l \rho_l \overrightarrow{v_l}) = 0 \tag{1}$$

Conservation equation of mass for the gas phase

$$\frac{\partial}{\partial t}\left(\alpha_g \rho_g\right) + \nabla\left(\alpha_g \rho_g \overrightarrow{v_g}\right) = 0 \tag{2}$$

Conservation equation of mass for the solid phase

$$\frac{\partial}{\partial t}(\alpha_s \rho_s) + \nabla\,(\alpha_s \rho_s \overrightarrow{v_s}) = 0 \tag{3}$$

where α, ρ, and v are the volume fraction, density and velocity of each phase, the subscript of l, g land s represent liquid, gas and solid phase, respectively. The sum of volume fraction for each phase should be equal to one.

$$\alpha_l + \alpha_g + \alpha_s = 1 \tag{4}$$

Conservation equation of momentum for the liquid phase

$$\frac{\partial}{\partial t}(\alpha_l \rho_l \overrightarrow{v_l}) + \nabla\,(\alpha_l \rho_l \overrightarrow{v_l}\,\overrightarrow{v_l}) = -\,\alpha_l \nabla p + \nabla\,\overline{\overline{\tau_l}} + \alpha_l \rho_l \vec{g} + M_l \tag{5}$$

$$\overline{\overline{\tau_l}} = \alpha_l \mu_l\left(\nabla\,\overrightarrow{v_l} + \nabla \overrightarrow{v_l}^{T}\right) - \alpha_l \frac{2}{3}\mu_l(\nabla\,\overrightarrow{v_l})\bar{\bar{I}} \tag{6}$$

Conservation equation of momentum for the gas phase

$$\frac{\partial}{\partial t}\left(\alpha_g \rho_g \overrightarrow{v_g}\right) + \nabla\left(\alpha_g \rho_g \overrightarrow{v_g}\,\overrightarrow{v_g}\right) = -\alpha_g \nabla p + \nabla \overline{\overline{\tau_g}} + \alpha_g \rho_g \vec{g} + M_g \tag{7}$$

$$\overline{\overline{\tau_g}} = \alpha_g \mu_g \left(\nabla \overrightarrow{v_g} + \nabla \overrightarrow{v_g}^T\right) - \alpha_g \frac{2}{3} \mu_g \left(\nabla \overrightarrow{v_g}\right) \bar{\bar{I}} \tag{8}$$

Conservation equation of momentum for the solid phase

$$\frac{\partial}{\partial t}\left(\alpha_s \rho_s \overrightarrow{v_s}\right) + \nabla\left(\alpha_s \rho_s \overrightarrow{v_s}\,\overrightarrow{v_s}\right) = -\alpha_s \nabla p + \nabla p_s + \nabla \overline{\overline{\tau_s}} + \alpha_s \rho_s \vec{g} + M_s \tag{9}$$

$$\overline{\overline{\tau_s}} = \alpha_s \mu_s \left(\nabla \overrightarrow{v_s} + \nabla \overrightarrow{v_s}^T\right) + \alpha_s \left(\lambda_s - \frac{2}{3}\mu_s\right) \nabla \overrightarrow{v_s} \bar{\bar{I}} \tag{10}$$

where p_s and μ_s are solid phase viscosity and pressure which can be obtained by the kinetic theory of the granular flow, and $\bar{\bar{\tau}}$ is the stress of each phase.

3.3.2Interphase forces

The momentum exchange term M_l, M_g, and M_s in governing equations will be closed by considering the interphase interaction forces among each phase including the drag force, lift force, turbulent dispersion force, virtual mass force and etc. Only the drag force and virtual mass force will be considered in the present study since the other two forces are negligible. For the drag force between the liquid and gas phases, the equation can be written as following

$$F_{drag,gl} = K_{gl}\left(\overrightarrow{v_g} - \overrightarrow{v_l}\right) \tag{11}$$

where K_{gl} is the momentum exchange coefficients between the liquid and gas phases, which is calculated by

$$K_{gl} = C_{D,gl} \frac{3}{4} \rho_l \frac{\alpha_g \alpha_l}{d_b} \left|\overrightarrow{v_g} - \overrightarrow{v_l}\right| \tag{12}$$

where d_b is the diameter of the bubble or droplet, and $C_{D,gl}$ is the drag coefficient between the gas and liquid phases, and the Schiller-Naumann drag model (Schiller & Naumann, 1935) is used to calculate, which is shown as

$$C_{D,gl} = \begin{cases} 24(1 + 0.15{Re_1}^{0.687})/Re_1 & Re_1 \leq 1000 \\ 0.44 & Re_1 > 1000 \end{cases} \quad (13)$$

$$Re_1 = \frac{\rho_l d_b |\overrightarrow{v_g} - \overrightarrow{v_l}|}{\mu_l} \quad (14)$$

The drag force between the liquid and solid phase can be expressed as

$$F_{drag,ls} = K_{ls}(\overrightarrow{v_s} - \overrightarrow{v_l}) \quad (15)$$

$$K_{ls} = C_{D,ls}\frac{3}{4}\rho_l \frac{\alpha_l \alpha_s}{d_p} |\overrightarrow{v_s} - \overrightarrow{v_l}| \quad (16)$$

where d_p is the diameter of the particles, and the drag model used to calculate the drag force between the liquid and solid phases is also based on the Schiller-Naumann drag model (Schiller & Naumann, 1935). The equations are listed as following

$$C_{D,ls} = \begin{cases} 24(1 + 0.15{Re_2}^{0.687})/Re_2 & Re_2 \leq 1000 \\ 0.44 & Re_2 > 1000 \end{cases} \quad (17)$$

$$Re_2 = \frac{\rho_l d_p |\overrightarrow{v_s} - \overrightarrow{v_l}|}{\mu_l} \quad (18)$$

The drag force between the solid and gas phases is shown as

$$F_{drag,gs} = K_{gs}(\overrightarrow{v_g} - \overrightarrow{v_s}) \quad (19)$$

$$K_{gs} = C_{D,gs}\frac{3}{4}\rho_g \frac{\alpha_g \alpha_s}{d_p} |\overrightarrow{v_g} - \overrightarrow{v_s}| \quad (20)$$

$$C_{D,gs} = \begin{cases} 24(1 + 0.15{Re_3}^{0.687})/Re_3 & Re_3 \leq 1000 \\ 0.44 & Re_3 > 1000 \end{cases} \quad (21)$$

$$Re_3 = \frac{\rho_g d_p |\overrightarrow{v_s} - \overrightarrow{v_g}|}{\mu_g} \quad (22)$$

3.3.3Turbulence model

In present study, the dispersed RNG k-ε turbulence model is used for the liquid phase, since it has a better performance than the standard and realizable k-ε models and per-phase RNG

k-ε model. (Hamidipour et al., 2012). The turbulence in dispersed phases, which are the gas phase and the solid phase in present study, is derived from the time and length scales instead of transport equations (ANSYS. Inc, 2014). The general form of the k-ε model is shown as following

$$\frac{\partial}{\partial t}(\alpha_l \rho_l k_l) + \nabla\,(\alpha_l \rho_l k_l \overrightarrow{v_l}) = \nabla\,\left(\alpha_l \left(\frac{\theta_k \mu + \mu_t}{\sigma_k}\right) \nabla k\right) + \alpha_l G_{k,q} - \alpha_l \rho_l \varepsilon_l + \Pi_k \qquad (23)$$

$$\frac{\partial}{\partial t}(\alpha_l \rho_l \varepsilon_l) + \nabla\,(\alpha_l \rho_l \varepsilon_l \overrightarrow{v_l}) = \nabla\,\left(\alpha_l \left(\frac{\theta_{1,\varepsilon} \mu + \mu_t}{\sigma_\varepsilon}\right) \nabla \varepsilon\right) + \alpha_l \frac{\varepsilon_l}{k_l}(C_{1\varepsilon}\theta_{2,\varepsilon} G_{k,q} - C_{2\varepsilon}\theta_{3,\varepsilon}\rho_l \varepsilon_l) + C_{3,\varepsilon}\alpha_l \rho_l \Pi_k - \alpha_l R_\varepsilon \qquad (24)$$

$$\mu_t = \rho C_\mu \frac{k^2}{\varepsilon} \qquad (25)$$

where k is the turbulence kinetic energy, ε is the turbulence kinetic energy dissipation, and Π_k is the source term to account for the turbulence interaction between phases, which is neglected in the dispersed model. G_k is the turbulence kinetic energy generated by mean velocity gradient, which is given as

$$G_k = \mu_t S^2 \qquad (26)$$

$$S = \sqrt{2 S_{ij} S_{ij}} \qquad (27)$$

$$S = \frac{1}{2}(\nabla \vec{v} + (\nabla \vec{v})^T) \qquad (28)$$

The RNG k-ε model is obtained by renormalizing the Naiver-Stokes equations based on renormalization group method (Yakhot & Orszag, 1986). The RNG k-ε model has a better performance on predicting rapid strained flows and swirling flow, and the RNG k-ε model can simulate the flow in a low-Reynolds region well by using an analytical formula to calculate the effective viscosity (ANSYS, 2014). The parameters of the standard k-ε turbulence model is modified as following when it is used as a dispersed RNG k-ε turbulence model

θ_k is set to one and σ_k is calculated based on σ_{eff} which is the effective Schmidt number, and it is shown by equation

$$\left|\frac{\left(\frac{1}{\sigma_{eff}}\right)-1.3929}{\left(\frac{1}{\sigma_0}\right)-1.3929}\right|^{0.6312}\left|\frac{\left(\frac{1}{\sigma_{eff}}\right)+2.3929}{\left(\frac{1}{\sigma_0}\right)+2.3929}\right|^{0.3679}=\frac{\mu}{\mu+\mu_t} \quad (29)$$

where $\frac{1}{\sigma_0} \approx 1$ and $\theta_k = 1$

σ_ε is defined based on σ_{eff} as well which can be also calculated by Eq (29). R_ε is the addiction model parameter calculated by

$$R_\varepsilon = \frac{\rho C_\mu \eta^3 (\frac{1-\eta}{\eta_0})}{1+\beta\eta^3}\frac{\varepsilon^2}{k} \quad (30)$$

where η is the dimensionless strain rate coefficient, which is calculated by

$$\eta = \frac{Sk}{\varepsilon} \quad (31)$$

In that case, the equations for the RNG k-ε turbulence model can be written as following

$$\frac{\partial}{\partial t}(\rho k) + \nabla(\rho_l k_l \overrightarrow{v_l}) = \nabla\left(\alpha_k \mu_{eff} \nabla k\right) + G_k + G_b - \rho\varepsilon - Y_M + S_k \quad (32)$$

$$\frac{\partial}{\partial t}(\rho\varepsilon) + \nabla(\rho_l \varepsilon_l \overrightarrow{v_l}) = \nabla\left(\alpha_\varepsilon \mu_{eff} \nabla\varepsilon\right) + C_{1\varepsilon}\frac{\varepsilon}{k}(G_k + C_{3\varepsilon}G_b) - \rho C_{2\varepsilon}\frac{\varepsilon^2}{k} - R_\varepsilon + S_\varepsilon \quad (33)$$

The relevant parameters of the RNG k-ε model is list in the Table 3.2

Table 3.2 Parameters of the dispersed RNG k-ε models

Parameters	θ_k	$\theta_{1,\varepsilon}$	σ_ε	σ_k	$C_{1\varepsilon}$	$C_{2\varepsilon}$
Values	1	1	Equation (29)	Equation (29)	1.42	1.68
Parameters	C_μ	R_ε	$\theta_{3,\varepsilon}$	$\theta_{2,\varepsilon}$	$C_{3,\varepsilon}$	Π_k
Values	0.085	Equation (30)	1	1	0	0

A wall function is used with a turbulence model in order to modify the model for the low Reynold number region. The scalable wall function is used in the present study, since the standard wall function is not accurately when y^* is smaller than 15. The scalable wall function refined the standard wall function when $y^* < 11.225$ by using a limiter shown in equation to avoid the c deterioration in the accuracy in the near wall region (ANSYS, 2014).

$$\widetilde{y^*} = Max(y^*, y^*_{limit}) \tag{34}$$

where $y^*_{limit} = 11.225$ and y^* is the dimensionless distance from the wall.

To describe the solid phase motion, the KTGP is used to in the Eulerian-Eulerian approach in order to close the solid phase governing equations. The granular temperature is introduced in the KTGP, which is related to the particle random motion, and solid phase stress and pressure can be calculated by using the granular temperature. The constitutive equations related to the KTGP are shown as following

Table 3.3 Constitutive equations of the solid phases

Solid pressure (Lun et al., 1984)	$P_S = \alpha_S \rho_S \Theta_S + 2\rho_S(1+e_{ss})\alpha_s^2 g_{0,ss}\Theta_s$	(35)
Radial distribution function (Ding & Gidaspow, 1990)	$g_{0,ss} = \left[1 - \left(\frac{\alpha_s}{\alpha_{s,max}}\right)^{1/3}\right]^{-1}$	(36)
Solid shear stress	$\mu_s = \mu_{s,col} + \mu_{s,kin} + \mu_{s,fr}$	(37)
Collisional viscosity (Gidaspow, 1994)	$\mu_{s,col} = \frac{4}{5}\alpha_s \rho_s d_s g_{0,ss}(1+e_{ss})\sqrt{\frac{\Theta_s}{\pi}}$	(38)
Kinetic viscosity (Syamlal et al., 1993)	$\mu_{s,kin} = \frac{\alpha_s \rho_s d_s \sqrt{\Theta_s \pi}}{6(3+e_{ss})}\left[1 + \frac{2}{5}(1+e_{ss})(3e_{ss}-1)\alpha_s g_{0,ss}\right]$	(39)

Frictional viscosity (Schaeffer, 1987)	$$\mu_{s,fr} = \frac{P_s \sin\phi}{2\sqrt{I_{2D}}}$$	(40)
Bulk viscosity (Lun et al., 1984)	$$\lambda_s = \frac{4}{3}\alpha_s^2 \rho_s d_s g_{0,ss}(1+e_{ss})\sqrt{\frac{\Theta_s}{\pi}}$$	(41)
Granular conductivity (Syamlal et al., 1993)	$$k_{\Theta_s} = \frac{15 d_s \rho_s \alpha_s \sqrt{\Theta_s \pi}}{4(41-33\eta)}\left[1 + \frac{12}{5}\eta^2(4\eta-3)\alpha_s g_{0,ss} + \frac{16}{15\pi}(41-33\eta)\alpha_s g_{0,ss}\eta\right]$$	(42)
Collisional dissipation of energy (Lun et al., 1984)	$$\gamma_{\Theta_s} = \frac{12(1-{e_{ss}}^2 g_{0,ss})}{d_s\sqrt{\pi}}\rho_s \alpha_s^2 \Theta_s^{3/2}$$	(43)

3.4 Numerical methodology

Two-dimensional simulations of the three-phase flows are conducted in this study for an inverse TPFB under the batch liquid model in order to study the hydrodynamics and flow patterns. The inverse TPFB shown in Figure 3.1 is simplified to a 2D planar computational domain, which is 3 m × 0.152 m based on the dimensions of the inverse TPFB used in the experiment. A uniform distributed quad grid mesh is used. The grid is 43×850 in the x and H directions. The schematic diagram of the computational domain, mesh, boundary conditions and initial conditions is shown in Figure 3.2. The mesh is created by using the commercial software ICEM 16.0.

The gas inlet is located at the bottom of the column, and the uniform velocity is used as the inlet boundary condition for the gas phase based on the experimental inlet superficial gas velocity. For the liquid and solid phases, the inlet velocity is zero for a batch liquid mode operation. The outflow is selected as outlet boundary condition for all three phases on the top of the column. The no-slip boundary condition is set for the liquid phase as wall the boundary condition, and the free-slip condition on the wall is used for both the gas phase

and solid phase, so the specularity coefficient of solid phase is set to zero which corresponds to the free-slip boundary condition. The particle-particle restitution coefficient is set as 0.95.

The particles have a mean diameter of 3.5 mm. For the gas bubble diameter, since the CFD model proposed in the previous study is modified in this study based on the bubble size, different bubble diameters from 3 mm to 5 mm are used for the gas phase, which depends on the inlet superficial gas velocity.

The initial conditions of the inverse TPFB under the batch liquid operating condition are shown in Figure 3.2, which are different from the conventional or circulating fluidized beds. To mimic the experimental condition, the liquid phase is initially patched inside the column, and particles are patched at the top surface of the liquid phase because the density of the particles is less than the density of the liquid phase.

The simulation is conducted using the commercial software Fluent 16.0. The double precision segregated, transient, implicit formulation are used. The phase coupled SIMPLE algorithm is used for the pressure-velocity coupling. The second order upwind scheme is used to discretize the momentum equations while the first order upwind discretization method is used for all other convection terms. The convergence criterion is set as 5×10^{-4} and the time step is set as 0.0001.

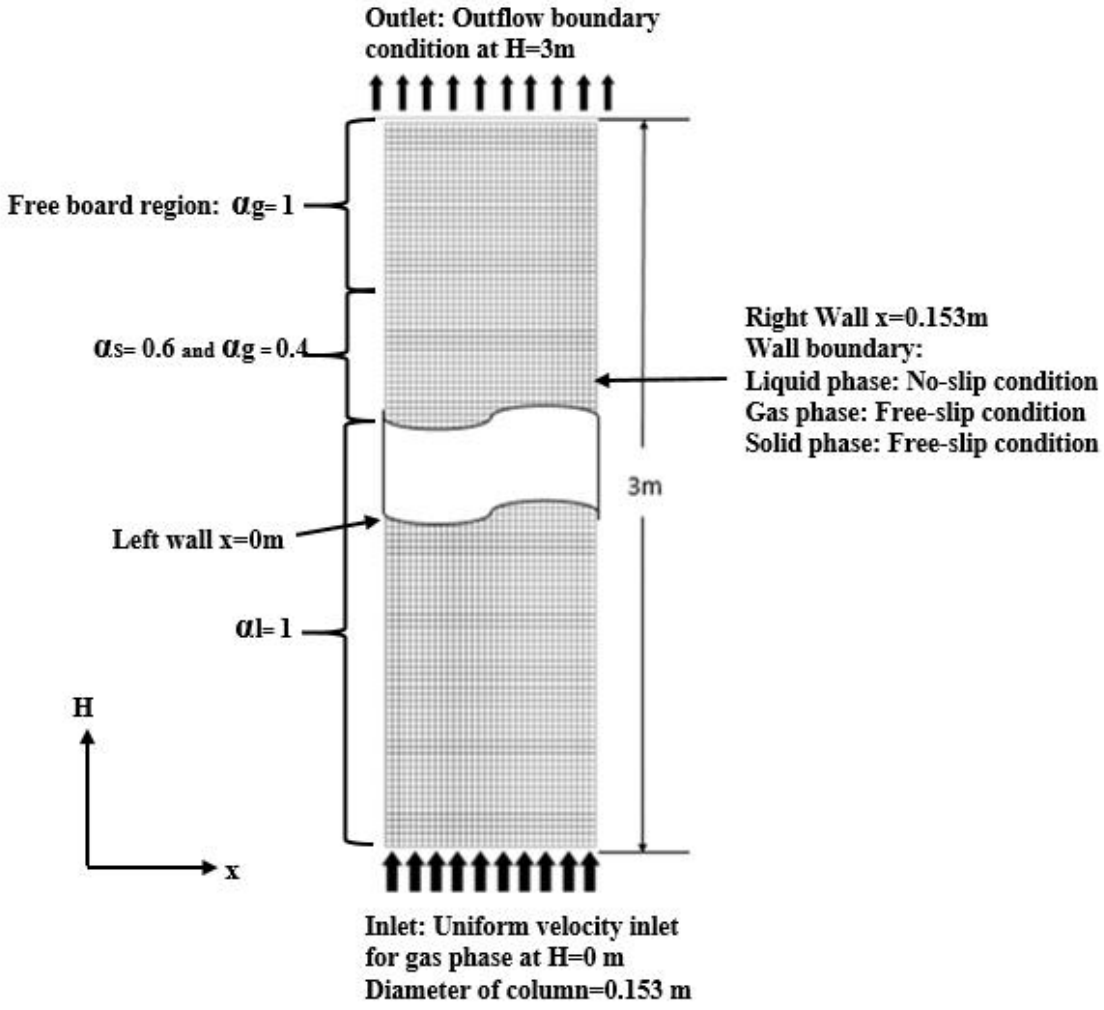

Figure 3.2 Computational domain of the inverse three-phase fluidized bed under the batch liquid mode

3.5 Grid Independence test

The grid independent study will be performed in this section under U_g=20 mm/s. The information on three different meshes is listed in Table 3.4, and the average gas holdup is used to check the grid independence. The results from the three meshes are listed in Table 3.5. It can be seen that the difference of average gas holdup between the medium mesh and fine mesh is less than 1%. Therefore, the medium size mesh is selected in this study for further simulations.

Table 3.4 Mesh information for the grid independent test

Mesh info	Size	Coarse	Medium	Fine
	Face	44815	73906	286680
	Node	22750	37400	144000
	Cell	22066	36507	142681

Table 3.5 Average gas holdups from different meshes

Mesh	Average gas holdup	Difference% of gas holdup
Coarse mesh	0.0856	
Medium mesh	0.0819	4.5%
Fine mesh	0.0816	0.4%

3.6 Results and discussion

The bubble size is found to have a significant on the average gas holdup in the inverse TPFB under the batch liquid mode. Therefore, the three-phase Eulerian-Eulerian CFD model developed in the previous study for the inverse TPFB is modified by adjusting the average bubble size. The effects on the bubble behavior and hydrodynamics in the inverse TPFB are investigated by using the modified CFD model.

3.6.1 Bubble size adjustment under different U_g

In the CFD model proposed in the previous work, a fixed mean bubble size of 2 mm was used for the simulations under different inlet superficial gas velocities because the gas bubbles generated from the gas distributor have an average size of 2 mm. According to the experimental study by Sun (2017), the gas bubbles inside the inverses TPFB tend to increase from 2 mm to 6 mm with the increase in the inlet superficial gas velocity from 10 mm/s to 60 mm/s. Thus, the constant value (2 mm) of the mean bubble size in the original three-phase CFD model is adjusted with the bubble size obtained from the experiment,

which is from 3 mm to 5 mm based on different U_g from 10 mm/s to 60 mm/s. In addition, the mean bubble sizes used in the modified CFD model are given in Table 3.6, which are obtained by a trail-and-error method. Figure 3.3 shows the comparison of the predicted average gas holdups under different U_g using the origin CFD model and the modified CFD model with the experimental data. It is clear that the gas holdup from the modified CFD model has a better agreement with the experimental data compared to the gas holdup from the original CFD model. Figure 3.3 also shows under the same U_g, the average gas holdup predicted by the original CFD model with a constant 2 mm bubble diameter is higher than that from the modified CFD model. The reason could be that the rising velocity of large bubbles is higher than the small bubbles, so the small bubbles will have a longer residence time in the column, which can lead to a higher gas holdup for small bubbles. In addition, it is observed based on the results from the modified CFD model and the experimental data that the increase of the gas holdup with U_g is almost linear when U_g is from 10-30 mm/s, but the increase of the gas holdup is lower when U_g is higher than 40 mm/s. The reason lies in that at a lower inlet superficial gas velocity, the small bubbles has a lower bubble coalescence rate, which lead to the uniform bubble size distribution. Therefore, the gas holdup is increased linearly with the increase in the inlet superficial gas velocity (Kawagoe, Nakado & Otake, 1976). However, the bubble coalescence rate will increase under a higher inlet superficial gas velocity, so the small bubbles start to coalescence and formulate large bubbles, which leads to a higher rising bubble velocity and less residence time in column. Thus, the increase in the gas holdup with the increase in the inlet superficial gas velocity is lower at a higher inlet superficial gas velocity, which is consistent with the experimental results from Jin et al. (2013). This is also the reason that the difference between the results from the original CFD model and modified CFD model becomes larger when the inlet superficial gas velocity is higher as shown in Figure 3.3 since a small mean bubble size is used for all inlet superficial gas velocities. In addition, the increase in the mean bubble size becomes smaller when U_g is above 40 mm/s when the solids loading is around 15% in the inverse TPFB. The reason is that the intensive interactions between the gas and particles break the large bubbles into small bubbles, so that the increase in the mean bubble size is lower at a higher inlet superficial gas velocity.

Table 3.6 Bubble sizes under the different inlet superficial gas velocities

Superfical gas velocity (mm/s)	Modified mean bubble size (mm)	Original mean bubble size (mm)
60	**5**	**2**
50	**4.7**	**2**
40	**4.5**	**2**
30	**4**	**2**
20	**3.5**	**2**
9	**3**	**2**

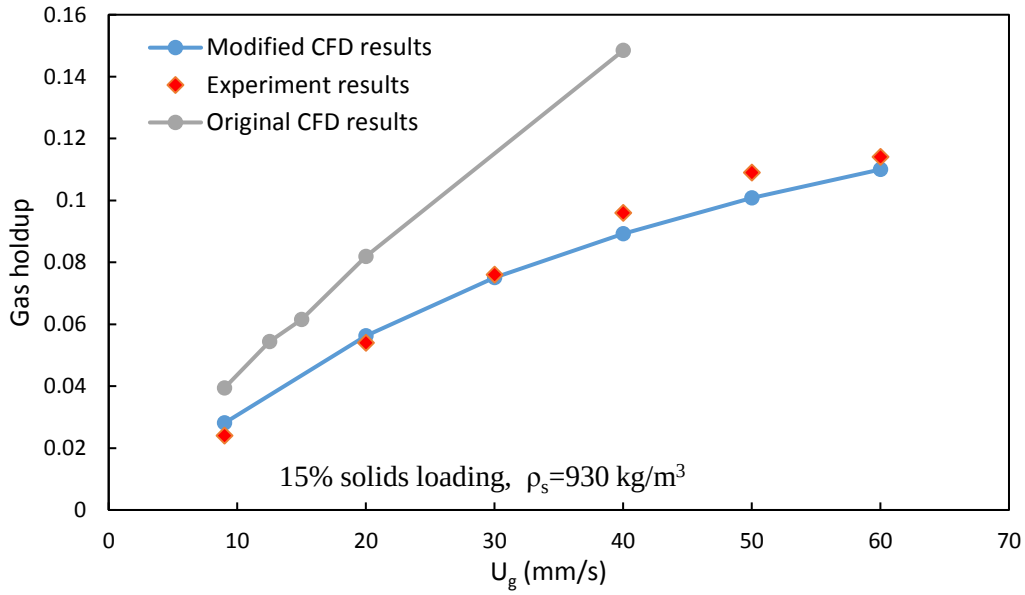

Figure 3.3 Comparison of the average gas holdup between the numerical results and experimental data under the different inlet superfical gas velocities at 15% solids loading and ρ_s=930 kg/m^3

Figure 3.4 (a) shows comparison of axial distributions of the gas holdup from the original CFD model and the modified CFD model under U_g=20 mm/s. Both the original model and the modified model give a uniform axial distribution of the gas holdup in the inverse TPFB, which is consistent with the experimental data. However, by using the original CFD model with the constant 2 mm bubble size, the axial gas holdup is around 0.08, which is obviously higher than the gas holdup from the experiential data. The axial gas holdup from the modified CFD model with a 3.5 mm bubble size for U_g = 20 mm/s shows a better agreement with the experimental data. Similarly, the results from the modified CFD model with the bubble size of 4.5 mm for U_g=40 mm/s has a better agreement with the experimental data than the original CFD model as shown in Figure 3.4 (b).

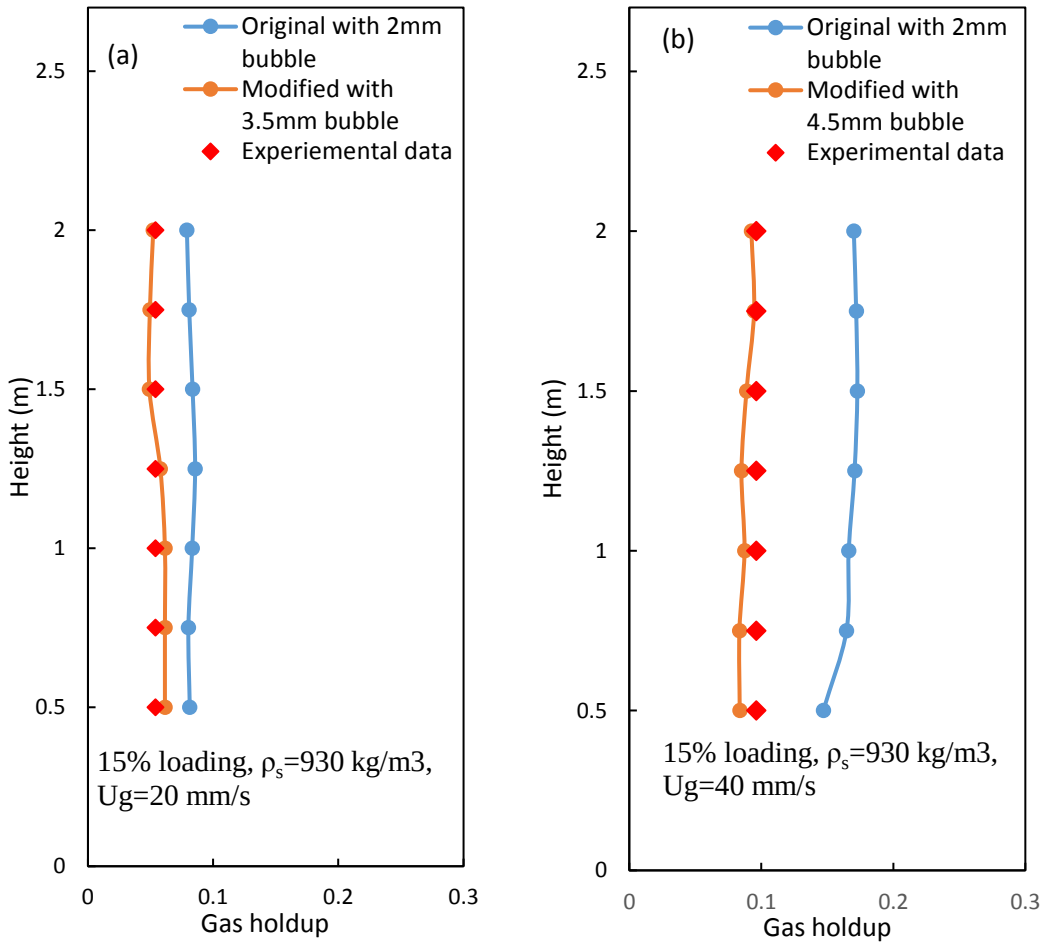

Figure 3.4 Comparison of the axial gas holdups from the origin CFD model and modified CFD model with the experiment data at ρ_s=930 kg/m^3 and 15% solids loading

(a) U_g= 20 mm/s and (b) U_g=40 mm/s

The time-averaged radial profiles of the gas holdup under three different superficial gas velocities at H=1.5 m using the modified CFD model are shown in Figure 3.5. The x-axis is the radial positon of the column, which is from the left wall (x=0 m) to the right wall (x=0.153 m), and the center of the column is at x=0.0765 m. The radial profiles of the gas holdup is almost flat for U_g=20 mm/s. When increasing the inlet superficial gas velocity, it is clear that the radial profiles of the gas holdup become less uniform, where the gas holdup

is higher at the center region and lower at the near wall region. This non-uniform radial profile is consistent with the most commonly seen experimental results of the gas-liquid two-phase or gas-liquid-solid three-phase bubble column (Jin et al., 2013; Rabha, Schubert, & Hampel, 2013; Yu & Kim, 1988). The reason is that the higher inlet superficial gas velocity results in a higher bubble coalescence rates, which lead to the formation of the large bubbles in the column, and large bubbles will stay at the center region of the column. In addition, the small bubbles tend to move toward the wall region due to the wall effect. Thus, large bubbles are dominant at the center region and result in a higher gas holdup at the center region of the column, which leads to a non-uniform profile of the gas holdup in the radial direction.

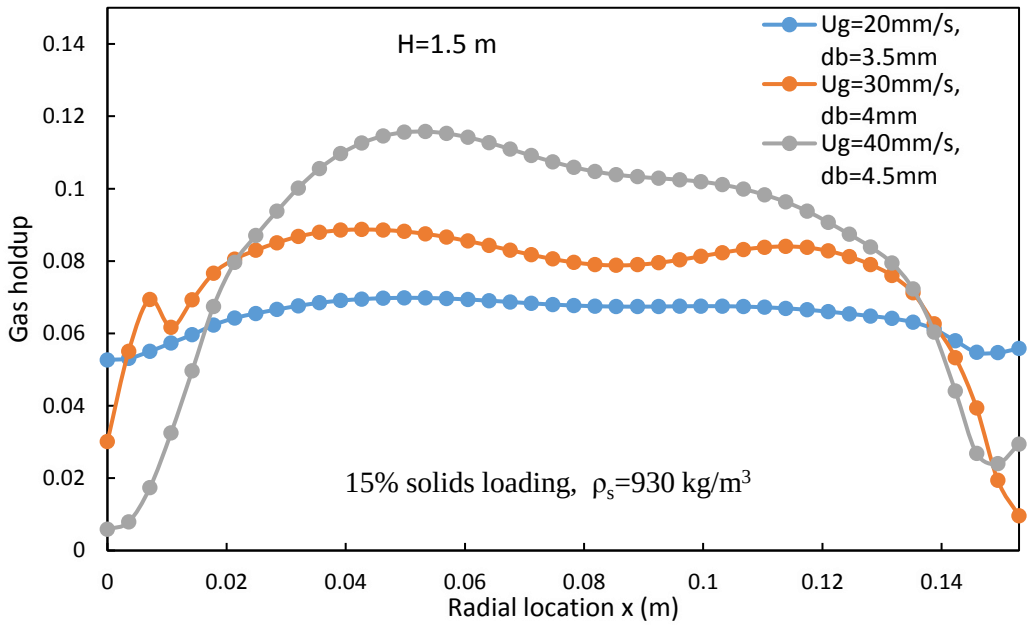

Figure 3.5 Time-averaged radial gas holdups under different superficial gas velocities from the modified CFD model

Figure 3.6 shows the comparison of the radial profiles of gas holdups between the original CFD model and the modified CFD model under U_g=20 mm/s and U_g=40 mm/s. At U_g=20 mm/s and U_g=40 mm/s, the original CFD model with 2 mm bubble size gives a higher gas holdup than the modified CFD model with the bubble diameters are 3.5 mm and 4.5 mm for U_g=20 mm/s and U_g=40 mm/s, respectively, because the large bubble has a lower

residence time, which can lead to a lower gas holdup. The radial profile of the gas holdup is almost flat for both the original CFD model and the modified CFD mode at U_g=20 mm/s, but the radial profile of the gas holdup from the modified CFD model is much more non-uniform than the original CFD model at U_g=40 mm/s. It can conclude that the large bubble size will lead a lower gas holdup under the same inlet superficial gas velocity.

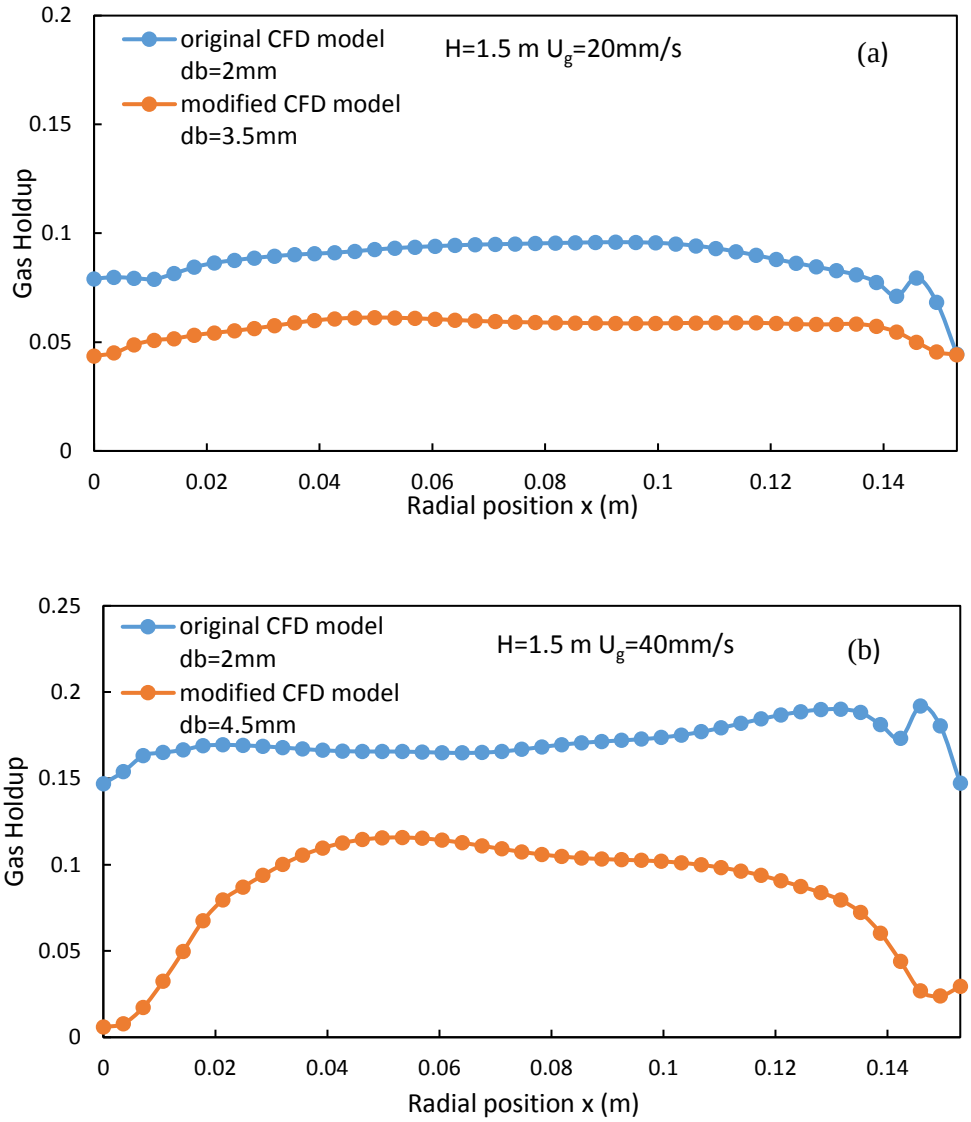

Figure 3.6 Comparison of the radial profiles of the gas holdup between the origin CFD model and the modified CFD model at 15% solids loading and ρ_s=930 kg/m^3

(a) Ug=20 mm/s and (b) Ug=40 mm/s

3.6.2 Mean bubble size correlation

A correlation between the mean bubble size and the average gas holdup under different inlet superficial gas velocities in the inverse TPFB has been proposed in this study. Many factors affect the bubble behavior in the inverse TPFB, such as the inlet superfical gas velocity, the gas holdup, the liquid density, the liquid viscosity and the particle density. As shown in Figure 3.3, the mean bubble size is related to the superficial gas velocity and the average gas holdup. The properties of the liquid and the solid phases can also influence the bubble size in an inverse TPFB since they affect the velocity field and the turbulence viscosity. Based on the CFD results and the literature reviews, the bubble size in the inverse TPFB is assume to be a function of liquid properties, solid density, gas holdup, inlet superfical gas velocity, which is shown as following

$$d_b = f(\rho_l, \rho_s, U_g, \mu_l, \varepsilon_g) \tag{44}$$

So the form of the correlation for the mean bubble size is considered to be written as following

$$d_b = K U_g^a \varepsilon_g^b (\frac{\rho_l}{\rho_s})^c \tag{45}$$

where K=0.0112, a=0.175, b=0.15 and c=0.12 which are determined using Matlab based on CFD results. Therefore,

$$d_b = 0.0112 U_g^{0.175} \varepsilon_g^{0.15} (\frac{\rho_l}{\rho_s})^{0.12} \tag{46}$$

The studies by Sun (2017) were carried out under the inlet superficial gas velocities from 10 to 60 mm/s, the corresponding average gas holdup in the inverse TPFB under the batch liquid mode increases from 0.03 to 0.12 with the increase in the U_g and the bubble size is from 2mm to 6mm. The predicted mean bubble size using the correlation is from 3mm to 5mm for the inlet superficial gas velocity from 10 to 60mm/s. Therefore, the correlation gives a good agreement with the experimental data. Thus, the correlation can be used to approximately estimate the mean bubble size when simulating the flow in the inverse TPFB under the batch liquid mode.

3.7 Conclusions

In the present study, a modified CFD model for the simulation of an inverse TPFB under the batch mode has been proposed based on the bubble size adjustment. The comparison between the results from the original CFD model and the modified CFD model indicates that the modified CFD model gives a better agreement with the experimental data than the original CFD model. Large size bubbles will result in a lower gas holdup under the same inlet superficial gas velocity. In addition, with the increase in the mean bubble size and superficial gas velocity, the radial profile of the gas holdup will be less uniform.

A correlation to predict the bubble size is proposed, and it has been validated as a reliable tool to approximately predict the average bubble size or gas holdup in the inverse three-phase fluidized bed under the batch liquid mode. The proposed correlation includes the density ratio of the liquid and the particle, which accounts for the influence of the fluidizing medium on the particle motion, and the parameter K may vary under the different properties of the liquid and the solids phases. Besides, the bubble size is influenced by the type of the gas distributor used at a low inlet superficial gas velocity, which is not taken into account in this study due to inadequate experimental data. Therefore, the correlation and K value can be further modified based on the fluidizing agents and gas distributors. The future work will focus on the modification of the K value, and the proposed correlation can be further modified when more experiments are carried out in the inverse TPFB under the batch liquid mode.

Reference

Ansys. Inc. (2014). Fluent 16.0 User's Guide.

Bandaru, K. S. V. S. R., Murthy, D. V. S., & Krishnaiah, K. (2007). Some hydrodynamic aspects of 3-phase inverse fluidized bed. *China Particuology*, *5*(5), 351–356. https://doi.org/https://doi.org/10.1016/j.cpart.2007.06.002

Buffière, P., & Moletta, R. (1999). Some hydrodynamic characteristics of inverse three phase fluidized-bed reactors. *Chemical Engineering Science*, *54*(9), 1233–1242. https://doi.org/10.1016/S0009-2509(98)00436-9

Cho, Y. J., Park, H. Y., Kim, S. W., Kang, Y., & Kim, S. D. (2002). Heat transfer and hydrodynamics in two- and three-phase inverse fluidized beds. *Industrial and Engineering Chemistry Research*, *41*(8), 2058–2063. https://doi.org/10.1021/ie0108393

Comte, M. P., Bastoul, D., Hebrard, G., Roustan, M., & Lazarova, V. (1997). Hydrodynamics of a three-phase fluidized bed - The inverse turbulent bed. *Chemical Engineering Science*, *52*(21–22), 3971–3977. https://doi.org/10.1016/S0009-2509(97)00240-6

Ding, J., & Gidaspow, D. (1990). A bubbling fluidization model using kinetic theory of granular flow. *AIChE Journal*, *36*(4), 523–538. https://doi.org/10.1002/aic.690360404

Fan, L. S., Muroyama, K., & Chern, S. H. (1982). Hydrodynamic characteristics of inverse fluidization in liquid-solid and gas-liquid-solid systems. *The Chemical Engineering Journal*, *24*(2), 143–150. https://doi.org/10.1016/0300-9467(82)80029-4

Gidaspow, D. (1994). *Multiphase Flow and Fluidization: Continuu and Kinetic Theory Descriptions*. Boston: Acad. Press.

Hamidipour, M., Chen, J., & Larachi, F. (2012). CFD study on hydrodynamics in three-phase fluidized beds — Application of turbulence models and experimental validation. *Chemical Engineering Science*, *78*, 167–180. https://doi.org/10.1016/j.ces.2012.05.016

Ibrahim, Y. A. A., Briens, C. L., Margaritis, A., & Bergongnou, M. A. (1996). Hydrodynamic Characteristics of a Three-Phase Inverse Fluidized-Bed Column. *AIChE Journal*, *42*(7), 1889–1900. https://doi.org/10.1002/aic.690420710

Jamialahmadi, M., & Muller-Steinhagen, H. (1993). Effect of Superficial Gas Velocity on Bubble Size, Terminal Bubble Rise Velocity and Gas Hold-up in Bubble Columns. *Developments in Chemical Engineering and Mineral Processing*, *1*(1), 16–31. https://doi.org/10.1002/apj.5500010103

Jin, H., Qin, Y., Yang, S., He, G., & Guo, Z. (2013). Radial profiles of gas bubble behavior

in a gas-liquid bubble column reactor under elevated pressures. *Chemical Engineering and Technology*, *36*(10), 1721–1728. https://doi.org/10.1002/ceat.201200551

Kawagoe, K., Nakado, T., & Otake, T. (1976). Flow pattern and gas hold up conditions in gas sparged contactors. *Int. Chem. Engng*, *16*(1), 176.

Kulkarni, A. A., & Joshi, J. B. (2005). Bubble formation and bubble rise velocity in gas-liquid systems: A review. *Industrial and Engineering Chemistry Research*, *44*(16), 5873–5931. https://doi.org/10.1021/ie049131p

Lee, D. H., Epstein, N., & Grace, J. R. (2000). Hydrodynamic Transition from Fixed to Fully Fluidized Beds for Three-Phase Inverse Fluidization. *Korean Journal of Chemical Engineering*, *17*(6), 684–690. https://doi.org/10.1007/BF02699118

Li, W., & Zhong, W. (2015). CFD simulation of hydrodynamics of gas-liquid-solid three-phase bubble column. *Powder Technology*, *286*, 766–788. https://doi.org/10.1016/j.powtec.2015.09.028

Lun, C. K. K., Savage, S. B., Jeffrey, D. J., & Chepurniy, N. (1984). Kinetic theories for granular flow: Inelastic particles in Couette flow and slightly inelastic particles in a general flowfield. *Journal of Fluid Mechanics*, *140*(1), 223–256. https://doi.org/10.1017/S0022112084000586

Muroyama, K., & Fan, L. -S. (1985). Fundamentals of gas-liquid-solid fluidization. *AIChE Journal*, *31*(1), 1–34. https://doi.org/10.1002/aic.690310102

Panneerselvam, R., Savithri, S., & Surender, G. D. (2009). CFD simulation of hydrodynamics of gas–liquid–solid fluidised bed reactor. *Chemical Engineering Science*, *64*(6), 1119–1135. https://doi.org/https://doi.org/10.1016/j.ces.2008.10.052

Rabha, S., Schubert, M., & Hampel, U. (2013). Intrinsic flow behavior in a slurry bubble column: A study on the effect of particle size. *Chemical Engineering Science*, *93*, 401–411. https://doi.org/https://doi.org/10.1016/j.ces.2013.02.034

Renganathan, T., & Krishnaiah, K. (2008). Prediction of Minimum Fluidization Velocity in Two and Three Phase Inverse Fluidized Beds. *The Canadian Journal of Chemical Engineering*, *81*(3–4), 853–860. https://doi.org/https://doi.org/10.1002/cjce.5450810369.

Schaeffer, D. G. (1987). Instability in the evolution equations describing incompressible granular flow. *Journal of Differential Equations*, *66*(1), 19–50. https://doi.org/10.1016/0022-0396(87)90038-6

Schiller, L., & Naumann, A. (1935). A drag coefficient correlation. *Z. Ver. Deutsch. Ing*, *77*, 318–320.

Son, S. M., Kang, S. H., Kim, U. Y., Kang, Y., & Kim, S. D. (2007). Bubble properties in three-phase inverse fluidized beds with viscous liquid medium. *Chemical Engineering*

and Processing: Process Intensification, *46*(8), 736–741. https://doi.org/10.1016/j.cep.2006.10.002

Son, S. M., Song, P. S., Lee, C. G., Kang, S. H., Kang, Y., & Kusakabe, K. (2004). Bubbling behavior in gas-liquid countercurrent bubble column bioreactors. *Journal of Chemical Engineering of Japan*, *37*(8 SPEC. ISS.), 990–998. https://doi.org/10.1252/jcej.37.990

Sun, X. (2017). *Bubble induced Inverse Gas-liquid-solid Fluidized bed*. University of Western Ontario.

Syamlal, M., Rogers, W., & O`Brien, T. J. (1993). *MFIX documentation theory guide*. United States. https://doi.org/10.2172/10145548

Yakhot, V., & Orszag, S. A. (1986). Renormalization group analysis of turbulence. I. Basic theory. *Journal of Scientific Computing*, *1*(1), 3–51. https://doi.org/10.1007/BF01061452

Yu, Y. H., & Kim, S. D. (1988). Bubble characteristics in the radial direction of three-phase fluidized beds. *AIChE Journal*, *34*(12), 2069–2072. https://doi.org/10.1002/aic.690341217

Chapter 4

4 Conclusions and Recommendations

4.1 Conclusions

An Eulerian-Eulerian three-fluid CFD model coupled with the kinetic theory of the granular flow is developed for an inverse three-phase fluidized bed under the batch liquid mode in this work. The proposed three-phase Eulerian-Eulerian CFD model is validated with the experimental data. The hydrodynamics and flow patterns under different operating conditions in the inverse three-phase fluidized bed were studied numerically using the proposed CFD model. Three stages of the fluidization process, which are the initial fluidization stage, developing stage and fully developed stage, in inverse three-phase fluidized beds has been defined based on the particle distribution in the column. The time required to reach to the developing stage and fully developed stage is longer when increasing the solids loading or decreasing the inlet superficial gas velocity. The non-uniform radial flow structures and recirculation phenomenon of the liquid and solid phases are found at all three stages of the fluidization process. The general hydrodynamics under different operating conditions including different superficial gas velocities, particle densities, and particle loadings has been investigated. It is found that increasing the inlet superficial gas velocity can result in a higher average gas holdup. A higher superficial gas velocity or solids loading can lead to a more non-uniform radial profile of the solids holdup. The particle density has almost no effect on the radial hydrodynamics and flow structures, but it is a key factor that can influence the axial distribution of the solids holdup. The solids volume fraction is higher at the lower section of the column when the particle density is higher under the same inlet superficial gas velocity and solids loading. The concentration of the solid phase at the lower section of the column will be higher when increasing the solids loading or inlet superficial gas velocity.

The modification of the proposed CFD model (chapter 2) based on the mean bubble size adjustment is carried out in the present study, because the bubble size is found to have a strong effect on the average gas holdup under the same inlet superficial gas velocity. A consistent bubble size is used in the original CFD model under different superficial gas

velocities. In the modified CFD model, the bubble size will increase with the increase in the inlet superficial gas velocity. The comparison between the CFD results and the experimental data indicates that the modified CFD model gives a better agreement with the experiment data in terms of the gas holdup. Using the modified CFD model, the non-uniform radial distribution of the gas phase was also found. With the increase in the inlet superficial gas velocity and average mean bubble size, the radial profile of the gas holdup is more non-uniform, which is higher at the center region and lower at the near wall region. A correlation to predict the mean bubble size was proposed, which includes the effects of the inlet superficial gas velocity, average gas holdup and density ratio of the liquid and particles on the bubble size, and was validated. Thus, the proposed correlation is considered as a reliable tool to approximately predict the mean bubble size or average gas holdup.

4.2 Recommendations

A CFD model has been developed to study the hydrodynamics and flow patterns in the inverse three-phase fluidized bed, and a correlation has been proposed to estimate the mean bubble size and average gas holdup in the present study. There are still some aspects that can be further investigated in order to better understand the hydrodynamics in inverse TPFB by CFD. The recommendations and future works are list as following

(1) The bubble behavior is considered to play an important role in the inverse three-phase fluidized bed, which has strong effects on hydrodynamics and flow pattern. Therefore, the Eulerian-Lagrangian approach can be used for the study of the bubble behavior in the micro-scale if the computational cost is acceptable.

(2) The uniform inlet velocity is used for the gas phase in present study. The effect of the gas distributor can be considered in the future.

(3) Two-dimensional simulation is used in present study to reduce the computational time. The three-dimensional simulation, which can provide more accurate flow patterns, can be used to compare with the results from two-dimensional simulation.

(4) The experimental data of the inverse three-phase fluidized bed used in this study, only have the average and axial distribution of each phase. When more experimental data are

available, such as the solids volume fraction in radial direction and bubble size distribution, the proposed CFD model can be further validated and modified.

(5) In terms of the proposed correlation for the mean bubble size, the parameter K can be further modified by using the different fluidized medium and taking the gas distributor effect into account.

Curriculum Vitae

Name:	Yunfeng Liu
Post-secondary Education and Degrees:	The University of Western Ontario London, Ontario, Canada 2012-2016 B.Sc.
	The University of Western Ontario London, Ontario, Canada 2016-2018 M.E,Sc
Honors and Awards:	Dean's Honor List 2014-2016
Related Work Experience	Teaching Assistant The University of Western Ontario 2016-2018